UNIVERSITÀ DEGLI STUDI DI PADOVA

Sede Amministrativa: Università degli Studi di Padova

Dipartimento di Ingegneria dell'Informazione

CORSO DI DOTTORATO DI RICERCA IN: Ingegneria dell'Informazione
CURRICOLO: Scienza e Tecnologia dell'informazione
CICLO XXXII

Instrumentation for Photon Handling of XUV and Soft X-ray Ultrafast Pulses

Coordinatore: Ch.mo Prof. Andrea Neviani
Supervisore: Ch.mo Dr. Luca Poletto

Dottorando: Nicola Fabris

UNIVERSITY OF PADOVA

PH.D. SCHOOL IN INFORMATION ENGINEERING

XXXII CLASS

DOCTORAL THESIS

Instrumentation for Photon Handling of XUV and Soft X-ray Ultrafast pulses

Author:
Nicola FABRIS

Supervisor:
Dr. Luca POLETTO

Ph.D. School Director:
Prof. Andrea NEVIANI

A thesis submitted in fulfillment of the requirements for the degree of Doctor of Philosophy

in the

DEPARTMENT OF INFORMATION ENGINEERING

JANUARY 2020

"The most beautiful experience we can have is the mysterious. It is the fundamental emotion that stands at the cradle of true art and true science."

Albert Einstein

Abstract

The recent availability of ultrafast coherent sources in the extreme ultraviolet (XUV) and soft X-ray spectral regions, such as high-order laser harmonics and free-electron lasers made possible time-resolved studies of electron and molecules dynamics on sub-femtosecond time scales. Simultaneously, the increasing demand of optical technologies suitable for photon handling and conditioning of this type of sources is a field where a strong collaboration between research and industry is required, in order to reach new results. This thesis concerns the design, realization and characterization of different monochromators dedicated to the selection of a portion of the spectrum generated by ultrafast sources.

The first contribution regards the comparison in terms of overall efficiency between two widely adopted single diffraction grating monochromators geometries, specifically the classical (CDM) and off-plane (OPM) mounts. A subsequent comparison with AFM-based simulations has been performed in order to validate the experimental results. Remarkably, the OPM diffraction efficiency is measured to $\approx$2 times and $\approx$7 times higher than the CDM at the XUV energies of 100 eV and 310 eV. Efficiencies as high as 45% at 100 eV and 35% at 310 eV have been measured for OPM gratings.

The second contribution consists in the software and optical setup of a double grating time-delay compensated monochromator. This monochromator will be soon inserted and ready for the alignment at the Extreme Light Infrastructure – Attosecond Light Pulse Source, ELI-ALPS, European ultra-high brightness laser facility (Hungary). The chosen parameters of the monochromator, in order to obtain the requested spectral bandwidth and temporal performances are analyzed in detail. The XUV monochromator simulated temporal resolution is lower than 15 fs at low energy resolution mode and lower than 30 fs at high energy resolution.

The third contribution consists in the characterization results achieved in terms of aberrations minimization, resolution and efficiency by designing a novel monochromator with a new three-optical-elements layout. The measured spectral resolving power is in the 3700–5200 range (output bandwidth <10 meV) over the spectral region of 12–50 eV. This is comparable to spectral resolving powers achieved on synchrotron beamlines. Excellent XUV monochromator performances has been obtained throughout by using simple optical components, which are available off the shelf on the market with high optical quality; although at modest prices.

Sommario

La recente disponibilità di sorgenti ultrabrevi nelle regioni spettrali dell'estremo ultravioletto (XUV) e dei raggi X soffici, tra le quali la generazione di armoniche di ordine elevato ed i laser a elettroni liberi hanno reso possibile lo studio di dinamiche risolte in tempo di elettroni e molecole, su scale temporali inferiori al femtosecondo. Simultaneamente, la crescente domanda di tecnologie ottiche atte alla manipolazione e al condizionamento di questo tipo di sorgenti è un campo nel quale è richiesta una forte collaborazione tra ricerca e industria per raggiungere nuovi risultati. Questa tesi riguarda la progettazione, realizzazione e caratterizzazione di diversi monocromatori dedicati alla selezione di una porzione dello spettro generato da sorgenti ultrabrevi.

Il primo contributo riguarda il confronto in termini di efficienza globale tra due geometrie di monocromatori a singolo reticolo di diffrazione ampiamente adottate, in particolare i montaggi in diffrazione classica (CDM) e conica (OPM). Per convalidare i risultati sperimentali è stato effettuato un successivo confronto con le simulazioni basate su analisi AFM. Sorprendentemente, l'efficienza di diffrazione OPM è stata misurata circa 2 e 7 volte superiore a quella CDM alle energie nell'XUV di 100 e 310 eV. Efficienze che raggiungono il 45% a 100 eV e 35% a 310 eV sono state misurate per i reticoli OPM.

Il secondo contributo consiste nella messa a punto software e ottica di un monocromatore a doppio reticolo a tempo compensato. Questo monocromatore sarà presto inserito e pronto per l'allineamento alla Extreme Light Infrastructure-Attosecond Light Pulse Source, ELI-ALPS, impianto laser europeo ad altissima luminosità (Ungheria). I parametri scelti dal monocromatore, per ottenere la banda spettrale e le prestazioni temporali richieste vengono analizzati in dettaglio. La risoluzione temporale simulata nell'XUV del monocromatore è inferiore a 15 fs con modalità a bassa risoluzione energetica e inferiore a 30 fs ad alta risoluzione energetica.

Il terzo contributo consiste nei risultati di caratterizzazione ottenuti in termini di minimizzazione delle aberrazioni, risoluzione ed efficienza progettando un nuovo monocromatore con uno schema a tre elementi ottici. La potenza di risoluzione è nell'intervallo 3700–5200 (larghezza di banda di uscita <10 meV) nella regione spettrale tra 12 e 50 eV. Questo è paragonabile alle risoluzioni spettrali ottenute sulle linee di luce da sincrotrone. Eccellenti prestazioni del monocromatore nell'XUV sono state ottenute nel complesso utilizzando semplici componenti ottici, che sono disponibili con disponibilità immediata sul mercato con alta qualità ottica; seppur a prezzi modesti.

Acknowledgements

This thesis represents an important milestone in my long career of student begun several years ago. During this three years of PhD I have met some truly remarkable people. They gave me the courage to overcome every doubt and discomfort. It is therefore compulsory to thank them all.

Thanks to my advisor Luca Poletto. To be an enthusiastic, proactive and competent researcher. Thanks to have trusted in me!
Thanks to Fabio Frassetto to have carefully reviewed this thesis providing positive comments and helpful hints.
Thanks to all the people who have worked with me at CNR-IFN in these years, especially Fabio Frassetto, Paolo Miotti and Fabio Samparisi who worked with me on the installation and characterization of multiple instruments and on different topics discussed in this manuscript.
Thanks to Paola Zuppella, Enrico Tessarolo, Lorenzo Cocola, Alain J. Corso, Stefano Bonora at CNR-IFN Padova for all the useful discussions had in these years.
Thanks to the CNR-ISM and ELI people for helping me and giving me a lot of useful tips in this years.
Thanks to the friends of ever Nicolò, Filippo, Marco, Leonardo and Eugenio.
Finally thanks to my family, to Luigina e Renato for their love in every moment of my life.

Thank you!

Contents

List of Figures

List of Tables

List of Abbreviations

AFM	**A**tomic **F**orce **M**icroscope
AOI	**A**ngle **O**f **I**ncidence
APT	**A**ttosecond **P**ulse **T**rain
BD	**B**eam **D**ump
BS	**B**eam**S**plitter
CAM	**CAM**era
CCD	**C**harge-**C**oupled **D**evice
CDM	**C**lassical **D**iffraction **M**ount
CEP	**C**arrier-**E**nvelope **P**hase
CMOS	**C**omplementary **M**etal-**O**xide-**S**emiconductor
CH	**CH**amber
CM	**C**yFchlindrical **M**irror
CRAB	**C**omplete **R**econstruction of **A**ttosecond **B**ursts
DE	**D**iffraction **E**fficiency
DS	**D**elay **S**tage
EEW	**E**lectromagnetic **E**lliptical **W**iggler
FEL	**F**ree-**E**lectron **L**aser
FL	**F**ocusing **L**ens
FROG	**F**requency **R**esolved **O**ptical **G**ating
FW	**F**ilter **W**heel
FWHM	**F**ull **W**idth at **H**alf **M**aximum
G	**G**rating
GC	**G**as **C**ell
GD	**G**roup **D**elay
GDD	**G**roup-**D**elay-**D**ispersion
GUI	**G**raphical **U**ser **I**nterface
HCF	**H**ollow **C**ore **F**iber
HH	**H**igh **H**armonic
HHG	**H**igh-order **H**armonic **G**eneration
HR	**H**igh **R**epetition
HWHM	**H**alf **W**idth at **H**alf **M**aximum
IAP	**I**solated **A**ttosecond **P**ulse
IR	**I**nfra**R**ed
LPF	**L**arge **P**itch **F**iber
MF	**M**etallic **F**ilter

NIM	**N**ormal **I**incidence **M**onochromator
OPM	**O**ff-**P**lane **M**ount
PCGPA	**P**rincipal **C**omponent **G**eneralized **P**rojections **A**lgorithm
PG	**P**olarization **G**ating
PIE	**P**tychographic **I**terative **E**ngine
PM	**P**lane **M**irror
PSD	**P**ower **S**pectral **D**ensity
RABBITT	**R**econstruction of **A**ttosecond harmonic **B**eating **B**y **I**nterference of **T**wo-photon **T**ransitions
RCW	**R**igorous **C**oupled-**W**awe
RM	**R**ecombination **M**irror
SAE	**S**ingle **A**ctive **E**lectron
SFA	**S**trong **F**ield **A**pproximation
SGM	**S**pherical **G**rating **M**onochromator
SB	**S**ide**B**and
SM	**S**pherical **M**irror
TDC	**T**ime-**D**elay **C**ompensated
TDSE	**T**ime-**D**ependent **S**chrödinger **E**quation
TE	**T**ransverse **E**lectric
TL	**T**ransform-**L**imited
TM	**T**ransverse **M**agnetic
TM	**T**oroidal **M**irror
TOF	**T**ime-**O**f-**F**light
XUV	e**X**treme **U**ltra**V**iolet

Chapter 1

Introduction

1.1 Topics covered in this thesis

In this thesis, a description of the activities related to the development, test and characterization of instrumentation dedicated to the monochromatization of ultrafast pulses in the extreme ultraviolet (XUV) and soft X-ray spectral regions is given. Specifically, three are the projects in which I have been involved:

1) the study of the XUV and soft X-ray efficiency performances of ultrafast single-grating monochromators;

2) the setup of a time-delay compensated monochromator for the spectral selection of attosecond XUV pulses;

3) the characterization of a high resolution XUV grating monochromator.

In this dissertation, a first brief introduction informs the reader about the importance of adopting ultrashort XUV pulses generated by the newest fully coherent sources as a unique tool to perform high-resolution time-domain spectroscopy experiments, involving different areas of science from solid-state physics to biology. Special emphasis is given to the parallel impressively enhance in the realization of optical technologies applied to photon handling and conditioning of this type of sources.

Chapter 2 treats some background concepts concerning three arguments. The first one refers to one the most promising type of sources adopted nowadays to generate XUV and soft X-ray radiation: high-order harmonic generation (HHG) in gases. Particular attention is dedicated to the optimal conversion efficiency conditions, i.e. phase matching and to the description of the polarization gating technique for the generation of isolated attosecond pulses. Secondly, a description of the behaviour of materials in the X-ray regime is reported, thus bringing to the selection of the most appropriate coatings to obtain the best propagation performances in terms of reflectivity. Finally, some techniques adopted for the temporal characterization of HHG pulses are reported.

Chapter 3 describes the advantages of adopting single-grating monochromators in terms throughput. Two are the compared configurations: classical diffraction

mount (CDM) and off-plane mount (OPM). The experimental results obtained at ELETTRA Synchrotron Trieste have been compared with the simulations performed exploiting the parameters derived from atomic force microscope (AFM) analysis.

Chapter 4 describes the design and software development of a double-grating time-delay compensated monochromator installed at the ELI-ALPS Laser Institute (Hungary). The simulated temporal and bandwidth performances are reported together with the future tests that will be performed.

Chapter 5 describes the design and the characterization of a high resolution XUV cost-effective grating monochromator which can be inserted in a high-repetition rate beamline dedicated to pump-probe experiments. The analysis of the acquired data obtained with a plasma source emitting in the XUV are presented.

The conclusion consists in a summary of the principal results described in the thesis and a discussion upon the possible future perspectives.

1.2 Author's contribution

In this Section, I give a short summary of my personal contribution in the realization of the three main activities reported above.

- **Study of the XUV and soft X-ray efficiency performances of ultrafast single-grating monochromators**

I collaborated in the development and realization of the experimental setup reported in sub-Section 3.3.1, employed for the efficiency measurements of the grating samples adopted for the CDM and OPM configurations. I took part to the measurements at ELETTRA Synchrotron, exploiting a source with a wide and continuous tunable energy range, performing a subsequent data analysis work in order to extract the efficiency results. In parallel I carried out the simulations of the tested gratings, adopting as parameters for the shape of the grooves and surface roughness, the ones obtained from the AFM analysis performed in the CNR-IFN research laboratories (Padova). After an accurate comparison between simulation and experimental data reported in Sections 3.5 and 3.6, I was able to extract important considerations regarding the influence on the efficiency performances of certain parameters more than others based on the adopted configuration.

- **Setup of a time-delay compensated monochromator for the spectral selection of attosecond XUV pulses**

I have been involved in the development and the characterization of an XUV double-stage monochromator. The instrument has been installed at the ELI-ALPS Laser Institute to give the possibility to the users to perform pump-probe experiments on solid samples with a monochromatic spectrum and a time resolution of few-femtoseconds. The main activity that I have performed during my two weeks of staying in Hungary was the development of the Labview software necessary for the

future alignment and calibration of the monochromator. This is described in detail in Section 4.5. I also collaborate to perform the first mechanical and optical elements tests of the instrument. I will take part to the future activities dedicated to the fulfilment of the efficiency, focal size and temporal resolution requirements as described in Section 4.7.

- **Characterization of a high resolution XUV grating monochromator**

The work is dedicated to the realization and characterization in terms of spatial resolution of a three-optical-elements XUV monochromator based on a grating with a variable subtended angle designed to have fixed entrance and exit arms, therefore suitable for microscopy applications. During my second year of Phd at CNR-IFN, I performed the focusing optimization of the instrument, i.e. the derivation of bandwidth performances adopting a plasma source able to emit discrete spectral lines in the XUV. Taking comparison with simulations good results has been obtained. I also worked on the data analysis aimed to derive the overall efficiency of the proposed design. This last task has been performed at ELETTRA Synchrotron. All the characterization activities are reported in Section 5.3.

1.3 XUV and soft X-ray ultrashort pulses

The natural time scale of molecular dynamics, and therefore for the building and breaking of chemical bonds, is in the femtosecond domain (1 fs = 10^{-15} s). The observation of chemical or biological transformations therefore typically requires measurements with femtosecond time resolution. Such observations are only possible with correspondingly short pulses, which then allow the photo-induced initiation of a process of interest using a short "pump" laser pulse, followed by a stroboscopic observation after a well-defined time delay, using an equally short "probe" pulse.

Photochemical reactions can be described making use of the Born-Oppenheimer approximation, where potential energy surfaces describe the energy of all electrons as a function of the atomic coordinates, as well as the resulting forces acting on the atoms. As the atoms move under the influence of these forces, the electrons adiabatically adapt until curve crossings are encountered, where the Born-Oppenheimer approximation breaks down and where the electronic structure may undergo drastic changes on time scales that are however still determined by the atomic motion.

The electronic motion, can occur on much faster, attosecond time scales (1 as = 10^{-18} s), taking as reference the 152 as orbital period derived from the Bohr atomic model of hydrogen. Until recently, direct measurements on these time scales were impossible. However, two ultrafast, XUV and X-ray sources are the new leading sources of the last decade, i.e. HHG discovered in 1961 by Franken et al. [1] and free-electron lasers (FELs) invented by John Madey in 1971 [2]. They are able to provide time-resolved access to processes that are happening into the attosecond domain.

In HHG, an intense femtosecond infrared (IR) laser is focused on an atomic or molecular gas. The XUV radiation can then be produced at laser frequencies that are odd, and in some cases very high multiples of the driver laser frequency. Only in 2001, has been demonstrated that attosecond XUV pulses can be created through HHG [3, 4].

If we adopt a sequence of femtosecond laser pulses with an envelope of few tens of femtosecond for HHG, it will form an attosecond pulse train (APT), rather than an isolated attosecond pulse (IAP). Performing attosecond pump-probe experiments with an APT intuitively seems very problematic. This because there is an uncertainty in the time delay between the pump and probe, since we do not know which attosecond pulse in the train has excited or probed the system.
The solution to this problem consists in configuring experiments where the APTs are used in combination with a co-propagating CEP-stabilized IR laser field (typically a replica of the laser that was used to generate the APT). Rather than using the pulse envelope of the co-propagating laser, the experiments use the optical cycle of this laser as a clock with attosecond time resolution. Given that the spacing between the attosecond pulses in the APT is exactly half the optical period, all attosecond pulses experience the same IR electric field (up to its sign), making time-resolved studies of electron dynamics on sub-femtosecond time scales possible. For example, small time delays between the XUV-induced ionization of different argon atomic orbitals could be characterized in two-color XUV-IR experiments using an APT [5].

Very extensive efforts have been developed to tailor the HHG process in a manner that rejects all except one of the attosecond pulses that are produced, in order to be able to configure experiments with IAPs. A number of different routes towards the generation of IAPs have been taken [6], and work in this direction continues to this days [7].

Although the first experimental demonstration of the formation of an IAP was almost immediately followed by a remarkable demonstration of the use of attosecond techniques to measure the lifetime of highly excited atoms undergoing Auger decay [8], the first few years after that were largely devoted to improvement of the attosecond pulse production and characterization techniques. Given that attosecond pulses can only be synthesized using wavelengths with an optical period in the attosecond domain, their central wavelength is automatically in the XUV/X-ray range, where the development of highly reflective dispersive optics is extremely challenging. Moreover, since XUV radiation is absorbed by all materials, the experiments have to be entirely performed in vacuum. This creates challenges for the separation of the attosecond pulses from the IR laser that has generated them. Moreover, attosecond experiments pose extreme requirements on the stability of optical setups. When one considers that a light pulse travels a distance of 30 nm in 100 as and that in certain types of attosecond setups the "pump" and "probe" lasers travel along separate paths over a distance of several meters, then it becomes clear that active stabilization of optical beam paths is often an absolute necessity to retain the attosecond

time resolution.

Make monochromatic APTs using specifically designed ultrafast instruments, i.e. the spectral selection of a single harmonic of a HHG spectrum in a wide XUV spectrum can be accomplished using a grating monochromator. In this thesis the development, test and characterization of ultrafast monochromators applied for the photon handling and conditioning of XUV and soft X-ray ultrashort pulses are presented.

Different characterization methods have been developed for APTs with and withouth a subsequent monochromatization, and IAPs. The first characterization of APTs used the RABBITT (reconstruction of attosecond harmonic beating by interference of two-photon transitions) method [9]. In the measurement, interferences in two-color XUV+IR photoelectron sidebands are used to characterize the relative phase of a comb of harmonics, providing a full characterization of the APT when combined with a measurement of the harmonic spectrum.
The characterization of IAPs generally relies on stronger IR laser fields, and uses the principle of the attosecond streak camera [10]: depending on the delay between the IAP and a co-propagating, moderately strong (typically 10^{12}–10^{13} W·cm^{-2}) IR laser field, the photoelectrons resulting from ionization by the IAP will be up or down-shifted. It has been shown that measuring a complete streaking trace, that is, a complete set of photoelectron spectra as a function of XUV-NIR delay, allows the full characterization of both the IAP [11] and the IR laser pulse [12].

Isolated attosecond pulses obtained by HHG are typically very weak. The conversion efficiency from IR to XUV is typically on the order of 10^{-6} in HHG, meaning that millijoule-level driver pulses will only lead to nanojoule-level XUV/X-ray pulses. In the approaches used for the generation of IAPs, the efficiency is usually even lower. For this reason, the two color XUV-IR experiments that were described above were up to now the only attosecond experiments possible. However, this is about to change. In the last few years, significant efforts have been undertaken to increase the pulse energy of attosecond pulses, in particular the pulse energy of IAPs, in attempts to make IAP pump-IAP probe experiments possible. Such experiments are extremely important, since they will allow more easy and reliable tracking of electronic motion over time delays exceeding the IR optical period. Several laboratories have developed attosecond experiments on the basis of larger scale laser systems delivering IR with several hundreds of millijoule pulse energy [13, 14]. With these systems IAPs with pulse energies in the 100 nJ range have recently been reported [14], which should be enough for IAP pump-IAP probe experiments.

Chapter 2

Theory and background

2.1 High-harmonic generation in gases

High-harmonic generation (HHG) in gases is a process in which a high intensity (10^{13}–10^{15} W·cm^{-2}) infrared (IR) laser pulse is focused on a noble gas jet (typically He, Ne and Ar). Such intensity is already comparable with the static Coulomb field experienced by an outer-shell electron in an atom, therefore the light-matter interaction can not be seen as a perturbative process anymore. This highly nonlinear interaction with the conversion medium generates a train sub-femtosecond bursts every half-optical cycle of the driving IR laser field. When detecting the radiation emitted on the laser axis, the measured spectra is made up of discrete peaks at the multiple odd frequencies of the IR laser frequency, so-called harmonic frequencies. The intensity of the first harmonic orders decreases quickly. However, they are followed by a plateau region with almost constant intensity and a cutoff energy with exponential decrease. Extremely high orders have been generated since the plateau has been shown to extend until the keV range [15].

The underlying physics can be understood with a model in three separate steps [16, 17, 18]. The whole process is laser driven and thus fully temporally and spatially coherent. Moreover, the HHG broadband spectrum should result in attosecond pulses if the different harmonics are perfectly phase-locked [19].

The unique properties of HHG have found applications in different fields. They can be used as a seed for the Free Electron Lasers in order to improve their temporal coherence [20]. They also can be applied to coherent lensless diffraction imaging of nanostructures with a spatial resolution of few tens of nanometers [21].

In this Section, a detailed treatment of the HHG process based on the semi-classical three-step model is given in sub-Section 2.1.1. Phase matching conditions are described in sub-Section 2.1.2. The generation of isolated attosecond pulses (IAPs) by means of the polarization gating technique is treated in sub-Section 2.1.3.

2.1.1 Semi-classical three-step model

A general important theoretical tool for describing quantum mechanical behavior is the time-dependent Schrödinger equation (TDSE). In single active electron approximation, the three dimensional time-dependent wave function $\psi(\mathbf{r}, t)$ that describes

the electron in a time dependent potential influenced by a strong laser field can be written as (using atomic units: m = e = $\hbar$ = 1):

$$i\frac{\partial}{\partial t}\boldsymbol{\psi}(\mathbf{r},t) = \left[-\frac{1}{2}\nabla^2 + V_0(\mathbf{r}) + \mathbf{r}\cdot\mathbf{E}(t)\right]\boldsymbol{\psi}(\mathbf{r},t), \tag{2.1}$$

where $V(\mathbf{r},t) = V_0(\mathbf{r}) + \mathbf{r}\cdot\mathbf{E}(t)$ is the time-dependent potential. $V_0(\mathbf{r})$ is the static intra-atomic or molecular potential. At high field intensities, the electronic wave function is extremely distorted since the field strength is comparable to the intra-atomic/molecular electric field. Its influence cannot be treated as a perturbation in this case. Thus the interaction with the laser $\mathbf{r}\cdot\mathbf{E}(t)$ is also considered, where $\mathbf{E}(t)$ is the electric field of the laser. The exact solution of the electronic wave function can be obtained by the integration of the equation. The numerical solution of the TDSE for single electron can be solved analitically in spherical coordinates. However, the full numerical solution for multi-electron systems would be extremely complicated due to the high dimensionality of the problem. Thus, single active electron approximation (usually from the highest occupied orbital) under a pseudo-potential is often applied.

On the other hand we would like to understand the physics insight of HHG which cannot be obtained from TDSE. Therefore, a simple semi-classical three-step model was developed based on two assumptions:

- Single Active Electron (SAE) approximation: lasers electric field interacts just with one electron coming from the atom ionization at a time;
- Strong Field Approximation (SFA): the contribution of all the excited bound states can be neglected; the effect of the atomic potential on the motion of the continuum electron can be neglected and the depletion of the ground state can be neglected.

When a strong laser field interacts with atom or molecule, its potential barrier is strongly deformed. Therefore the electron can tunnel ionize out from its parent atom/molecule with initially zero velocity (i). Then the freed electron is accelerated away from the ion by the laser field, and its acceleration reverses when the laser field changes the direction of the oscillation (ii). Eventually, the electron gets chance to recollide with its parent ion, at which moment converts the gained kinetic energy into an extreme ultraviolet photon (iii).

In this model, the electron is treated by quantum mechanics at the instant of ionization, but its dynamics after are considered classically: the electron is considered as a classical point charge, and during the second step one considers the driving laser field to completely govern its evolution. This process can be repeated each half-cycle of the laser oscillation, producing an APT during the IR envelope. In the following, each one of these fundamental mechanisms will be treated.

Tunnel ionization

The tunnel ionization process is very important in HHG, because it is not only the basis for all subsequent physical processes but also the source of the extreme nonlinearity required to push the pulse duration to attosecond regime. To understand the mechanism of tunnel ionization, a comparison of different ionization schemes, in the case of hydrogen-like atoms interacting with an infrared laser field is given in Fig. 2.1.

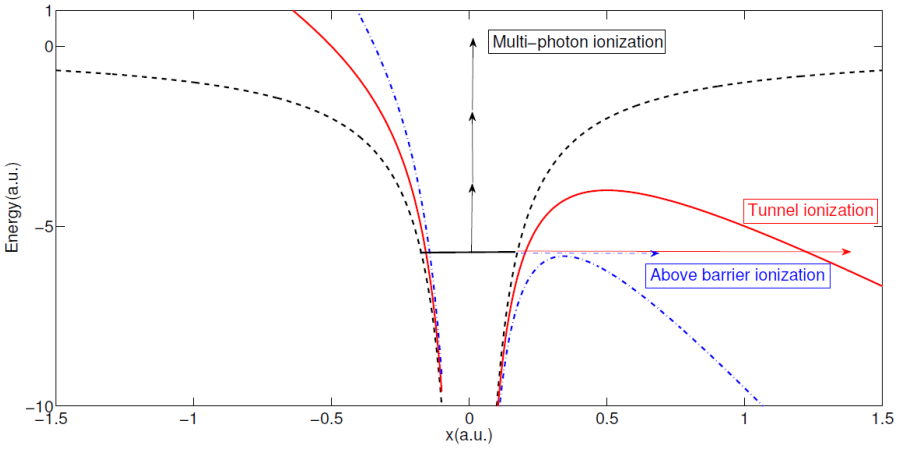

FIGURE 2.1: Different ionization schemes. The horizontal black line indicates the atomic ground state. Multi-photon ionization dominates when the external electric field is negligible (black dashed line). With the increase of the laser intensity, the Coulomb potential barrier is lowered so that the tunnel ionization happens (red solid line). A sufficiently intense electric field completely suppresses the potential barrier, in which case the above-barrier ionization takes place (blue dash-dotted line).

In strong field physics, the barrier formed by the coulomb potential $V_0(x)$ is modified by the electric field linearly polarized along the x direction:

$$\mathbf{E}(t) = E_0 \cos(\omega_0 t)\hat{x}, \tag{2.2}$$

where E_0 is the amplitude and ω_0 is the angular frequency of the laser. The total potential $V(x,t)$ felt by the electron is:

$$V(x,t) = V_0(x) + (-e)E(t)x = -\frac{Z_{eff}e^2}{4\pi\epsilon_0}\frac{1}{x} + (-e)E_0 \cos(\omega_0 t)x, \tag{2.3}$$

where Z_{eff} is the effective nuclear charge, e is the electron charge and ϵ_0 is the vacuum permittivity. Figure 2.1 shows different schemes of ionization due to the influence of the laser. The electron can be ionized from the simultaneous absorption of several photons corresponding to an energy greater than the ionization potential, which is referred as multi-photon ionization. When the external electric field is comparable to the binding electric field between the nucleus and the electron, it distorts

the Coulomb potential. Therefore, the electron gets a given probability to tunnel through a barrier that it classically could not surmount. This tunnel ionization effect is a quantum phenomenon (the wave function tunnels into the continuum) that depends on the height and the width of the barrier and on the time during which the barrier is lowered. By continuously increasing the driving intensity, the potential barrier can be suppressed completely so that the electron gets free. This kind of ionization is called above-barrier ionization. The maximum laser intensity (referred to as saturation intensity $I_{BS} = E_{BS}^2/(8\pi)$), that can be applied before reaching the barrier suppression can be found by determining the position (x_0) of the inflection point on the potential barrier. By deriving Eqn. (2.3) with respect to the position, one finds that $x_0 = (Z_{eff}e/4\pi\epsilon_0 E_{BS})^{1/2}$. The saturation intensity is found by substituting the x_0 back to Eqn. (2.3):

$$I_{BS}[W \cdot cm^{-2}] = 4 \cdot 10^9 \frac{I_p^4[eV]}{Z_{eff}^2}, \tag{2.4}$$

where I_p is the atomic ionization potential. For the noble gases krypton and argon, where $Z_{eff} = 1$, this implies $I_{BS}^{Kr} = 1.5 \cdot 10^{14}$ W·cm^{-2} and $I_{BS}^{Ar} = 2.5 \cdot 10^{14}$ W·cm^{-2}.

The description given above for a quasi-static field should be complemented in the case of an oscillating laser field due to the fact that tunnel ionization also depends on the time during which the barrier is lowered, proportional to the laser field.
We can distinguish between different ionization regimes of the light matter interaction with the introduction of the Keldysh parameter [22]:

$$\gamma = \sqrt{\frac{I_p}{2U_p}} = \frac{\omega_0}{e}\sqrt{\frac{c\epsilon_0 m_e I_p}{I_0}} = \frac{T_{tunnel}}{T_0}, \tag{2.5}$$

where I_p is the ionization potential, $I_0 = c\epsilon_0 E_0^2/2$ is the intensity of the laser field (c is the speed of light in vacuum). U_p is the ponderomotive potential, i.e. the mean quiver energy of a free electron in the laser field:

$$U_p = \frac{e^2 E_0^2}{4 m_e \omega_0^2} \qquad U_p[eV] = 9.337 \cdot 10^{-14} I_0[W \cdot cm^{-2}]\lambda^2[\mu m^2], \tag{2.6}$$

where m_e is the electron mass. $T_{tunnel} = 2\pi(c\epsilon_0 m_e I_p)^{1/2}/eE_0$ is the ionization time the electron takes to tunnel through the barrier. In particular, γ measures the ratio between the time needed for an electron to cross the Coulomb barrier, and the period of the oscillation, $T_0 = 2\pi/\omega_0$. Therefore, a value of $\gamma \gg 1$ indicates multi-photon ionization, since for higher laser frequency the electron does not have enough time to follow the fast changes in the potential. In this case, the electron motion will be then governed by an average over many cycles of the laser field rather than by the tunneling process in a single cycle, since the tunneling time is larger than the optical period. Therefore the absorption of many photons will lead to an electronic state with an energy larger than zero, thus a free electron. On the other hand, the condition $\gamma \ll 1$ implies barrier suppression.

Acceleration in the continuum

Upon the instant of tunnel ionization (t_i), the electron is freed in the continuum with initially zero velocity. From this moment on, the electron is considered as a classical point charge, and during the second step one considers the driving laser field, $\mathbf{E}(t)$, to completely govern its evolution.

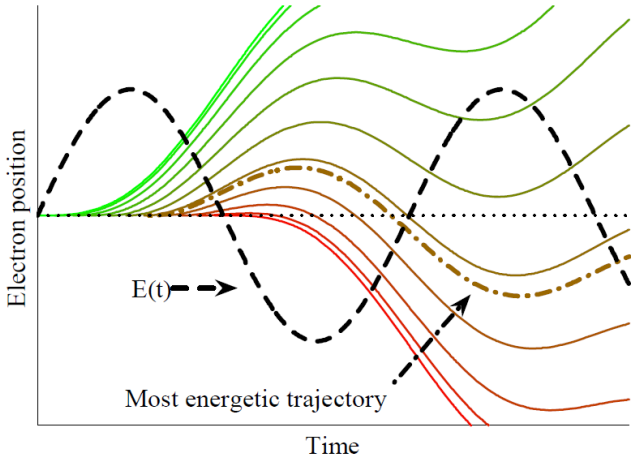

FIGURE 2.2: The position of the electron as function of time for different ionization times t_i. The most energetic trajectory refers to the solution where the electron encounters the nucleus with the maximal kinetic energy.

We assume that the position of the electron at t_i corresponds to the position of the atom, $x_0 = 0$. Therefore, the velocity and displacement of the electron can be calculated from Newton's second law of motion using Eqn. (2.2):

$$v_x(t) = \int_{t_i}^{t} -\frac{e}{m_e} E(t')dt' + v_0 \tag{2.7}$$

and

$$x(t) = \int_{t_i}^{t} v_x(t')dt' + x_0. \tag{2.8}$$

By assuming the initial conditions $v_0 = 0$ and $x_0 = 0$ we obtain:

$$v_x(t) = -\frac{E_0 e}{m_e \omega_0} \left[\sin(\omega_0 t) - \sin(\omega_0 t_i)\right] \tag{2.9}$$

and

$$x(t) = \frac{E_0 e}{m_e \omega_0^2} \left[\cos(\omega_0 t) - \cos(\omega_0 t_i) + \omega_0 (t - t_i) \sin(\omega_0 t_i)\right]. \tag{2.10}$$

From Eqn. (2.10), the electron trajectories that correspond to different tunnel ionization moments (t_i) can be obtained, as shown in Fig. 2.2. The electron reverses its acceleration direction when the electric field changes its sign. The electrons just drift away if the ionization occurs at specific times ranges of the cycle. Moreover, some trajectories indicate several recollisions. As we will see if phase matching is

ensured, it will decrease the contribution of longer trajectories to the macroscopic HHG signal. Therefore, we can only consider the first recollisions.

Recombination

In the case of linear polarization, the electron can return to the parent ion and recombine to the ground state, with emission of photons with energy given by the following expression:

$$\hbar\omega(t) = I_p + \frac{1}{2}m_e v^2 = I_p + 2U_p\left[\sin(\omega_0 t) - \sin(\omega_0 t_i)\right]^2. \tag{2.11}$$

The recombination instant can be calculated by solving the equation $x(t) = 0$, which does not have analytical solutions. However, it is possible to show that the freed electron can return to the parent ion if $0° \leq \omega_0 t \leq 80°$ or $180° \leq \omega_0 t \leq 260°$. The numerical solution of equation $x(t) = 0$ can be fitted by the function given in terms of phases [23]:

$$\omega_0 t = \frac{\pi}{2} - 3\sin^{-1}\left(\frac{2}{\pi}\omega_0 t_i - 1\right), \tag{2.12}$$

as shown in Fig. 2.3(a). By using the previous expression in Eqn. (2.11) it is possible to obtain a simple expression for the energy of the emitted photons

$$\hbar\omega(t) = I_p + 2U_p\left\{\cos\left[3\sin^{-1}\left(\frac{2}{\pi}\omega_0 t_i - 1\right)\right] - \sin(\omega_0 t_i)\right\}^2. \tag{2.13}$$

Figure 2.3(b) shows the kinetic energy of the returning electron, normalized to the ponderomotive energy, as a function of the emission phase $\omega_0 t_i/2\pi = t_i/T_0$. The electron released at a particular instant $t_i < 0.05T_0$ has the same kinetic energy of an electron emitted at $t_i > 0.05T_0$. Since shorter ionization times, t_i, correspond to longer recombination times, t, it is common to group the trajectories described by the electrons between tunnel ionization and recombination in two classes. The long trajectories are the paths followed by the electrons ionized at $t < 0.05T_0$, while the short paths correspond to the trajectories described by the electrons ionized at $t > 0.05T_0$. In the case of the short trajectories, the corresponding recombination time, t is $0.25T_0 < t < 0.7T_0$. For the long trajectories $0.7T_0 < t < T_0$.
The maximum energy of the photons emitted by recombination of the returning electrons is given by $\hbar\omega_{max} = I_p + 3.17U_p$ (cutoff law). Since $U_p \propto I_0\lambda_0^2$, the cutoff frequency can be extended by increasing the excitation intensity and by increasing the wavelength. On the other hand the driving intensity is limited by the saturation intensity, which leads to complete ionization of the ground state.

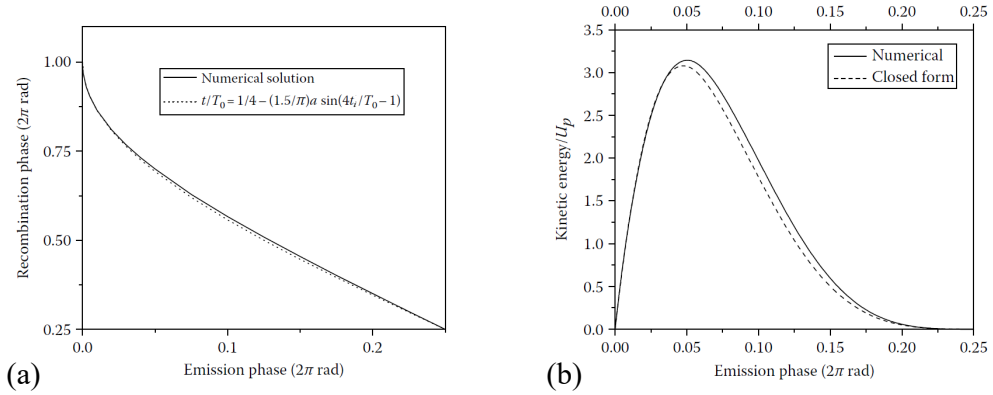

FIGURE 2.3: (a) Dependence of the recombination time on the releasing time. (b) The kinetic energy of the returned electron normalized to the ponderomotive energy.

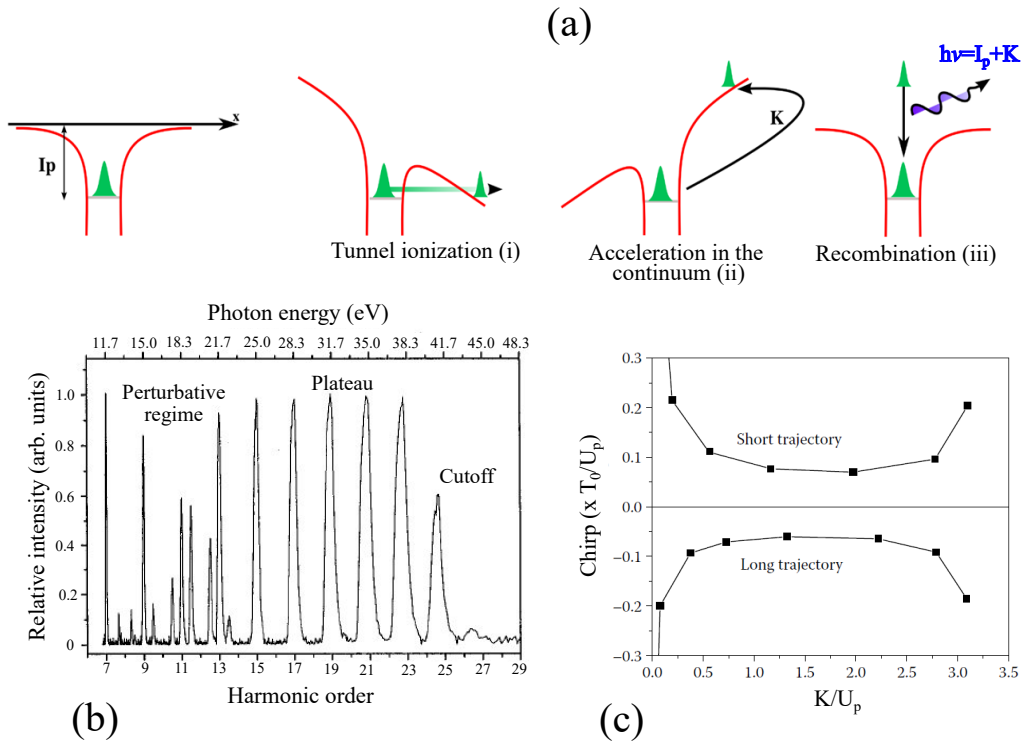

FIGURE 2.4: (a) Three-step model. (b) A typical high-harmonic spectrum generated in argon. (c) The chirp in unit of T_0/U_p as function of K/U_p.

Since the instantaneous angular frequency of the XUV pulses is a function of time, as shown by Eqn. (2.11), the attosecond pulses present an intrinsic chirp, $C = d\omega/dt$. The XUV pulses generated by the short trajectories exhibit a positive (almost linear) chirp, while the pulses generated by the long ones are negatively chirped. The short electron trajectories can be experimentally selected, thus generating trains

of attosecond pulses characterized by a linear and positive chirp, which can be properly compensated by suitable techniques [24, 25]. The overall three-step model process is shown in Fig. 2.4(a) together with a typical high-harmonic spectrum generated in argon in Fig. 2.4(b) and the dependence of the chirp on the kinetic energy K in Fig. 2.4(c).

2.1.2 Phase matching in HHG

The attosecond high-harmonic field emitted from a single atom is too weak for applications. To produce sufficient XUV photons, many atoms are placed in the interaction region. The energy of single isolated attosecond pulses generated with a few mJ femtosecond lasers is on the order of 1 nJ. Thus the conversion efficiency is about 10^{-6}. Finding schemes that can significantly increase the conversion efficiency is one of the biggest challenges in attosecond optics research. The condition in which fields emitted by atoms located at different positions in the propagation direction are in phase so that they add up constructively on the detector is called phase matching. Improving the length over which the attosecond fields are phase matched (coherent length), is one of the active areas of HHG research.
In the case of monochromatic paraxial linearly polaarized plane waves, the wave equation of the total field (assuming z as the propagation direction) can be expressed as

$$2ik_q \frac{\partial}{\partial z} A_q(z) = \mu_0 \omega_q^2 P_q e^{i(k_q - qk_0)z}, \tag{2.14}$$

where μ_0 is the vacuum permittivity and k_0 is the propagation constant of the driving laser. Here k_q and $\omega_q = q\omega_0$ are, respectively, the propagation constant and the angular frequency of the q-th harmonic field. A_q and P_q are, respectively, the the q-th harmonic component of the total field and nonlinear polarization.
The variation of the q-th harmonic field amplitude in the propagation direction can be calculated as

$$A_q(z) = -i\frac{\mu_0 \omega_q^2}{2k_q} \int_0^z P_q e^{i\Delta k_q z} e^{-\alpha_q z} dz \quad with \quad \Delta k_q = \frac{\omega_q}{c} n_R(\omega_0) - qk_0 \tag{2.15}$$

where $\alpha_q = \omega_q n_I(\omega_q)/c$ is the absorption coefficient, assuming that $n_R - in_I$ is the complex index of refraction of the medium.
When a phase mismatch Δk_q independent of z and no absorption are assumed, the harmonic intensity is proportional to the product between length L and field-free gas density N

$$I_q(NL) \propto (1-p)^2 (NL)^2 sinc^2\left(\frac{\Delta k_q L}{2}\right), \tag{2.16}$$

where p is the gas ionization probability. Dephasing effects show up when the medium length is longer than the coherent length

$$L_c = \frac{\pi}{\Delta k_q}, \tag{2.17}$$

When absorption α_q is considered, $A_q(z)$ reaches an asymptotic maximum value when the propagation distance is much longer than the absorption length

$$L_a = \frac{1}{2\alpha_q} = \frac{1}{N\sigma_q} \quad with \quad \sigma_q = 2r_e\lambda_q f_2(\lambda_q), \tag{2.18}$$

where $\lambda_q = 2\pi c/\omega_q$, f_2 is the imaginary part of the atomic scattering factor and r_e is the classical electron radius. Here, due to the high photon energy the harmonic radiation can excite core electrons and ionize valence electrons along its propagation in the gas medium and can be reabsorbed. For this reason the conversion efficiency saturates after L_a. For a given target gas density, the absorption length is determined by the harmonic photon energy. The dependence of the XUV photon flux on the medium length for several coherent lengths is shown Fig. 2.5. The medium length should be set to $L > 3L_c$. The coherent length should be much larger than the absorption length. As a rule of thumb, to generate more than 50% of the maximum photon flux, the phase matching should be improved so that $L_c > 5L_a$.

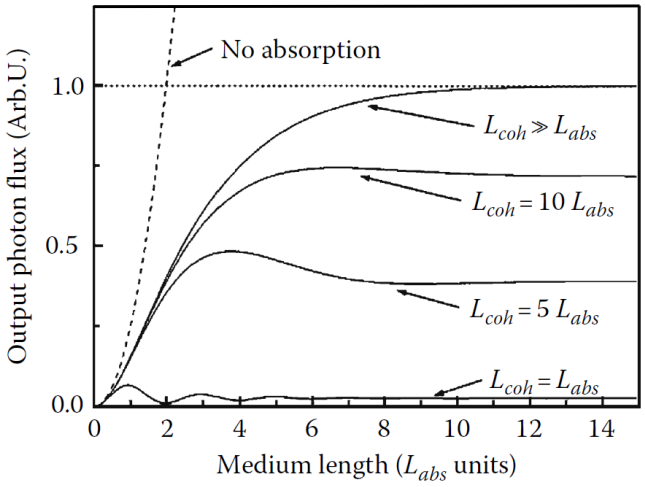

FIGURE 2.5: Dependence of output photon flux on gas parameters. The quantity L_{coh} and L_{abs} in the figure are the coherent and absorption lengths, respectively.

Four are the main terms which contribute to the phase mismatch:

$$\Delta k = \underbrace{\Delta k_a}_{>0} + \underbrace{\Delta k_{fe}}_{<0} + \underbrace{\Delta k_{foc}}_{<0} + \underbrace{\Delta k_{dip}^{traj}}_{\text{sign(z)}}. \tag{2.19}$$

The first term takes into account the dispersion in the neutral atom. The generation of a plasma (hence free electrons) also influences the phase matching mechanism because of the introduction of a time dependent refractive index affecting the propagation of the driving pulse. Such dispersion term, tends to speed up the fundamental phase velocity with respect to the harmonic radiation, thus reducing the coherence length. Since shorter wavelengths ($q \gg 1$) are generated in the presence of a higher

free electron density, the phase mismatch Δk_{fe} rapidly increases with harmonic order.
The third term in Eqn. (2.19) is given by the fact that when the focusing fundamental laser beam is Gaussian it experiences a geometric phase shift $\phi(z)$ called Gouy phase shift:

$$A_0(r,z) = A_0 \frac{w_0}{w(z)} e^{-\frac{r^2}{w^2(z)}} e^{-i\frac{r^2}{2R(z)}} e^{i\phi(z)}, \tag{2.20}$$

where

- A_0 is the amplitude of the field at the laser focus and on axis;
- w_0 and $w(z)$ are the radius of the beam at the focus and at position z;
- R(z) is the radius of curvature of the wave front;
- ψ is the Gouy phase.

When the intensity is chosen to the lowest value for perfect phase matching, we have $z = z_R$, where $z_R = \pi w_0^2$ is the Rayleigh range. It means that the target should be located one Rayleigh range away after the laser focus as shown in Fig. 2.6.

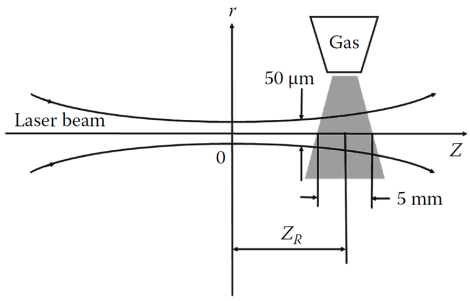

FIGURE 2.6: Gas target delivered from a nozzle located near the laser focus. Here, z_R is the Rayleigh range of the laser beam. The typical value of the gas volume with high enough driving laser intensity is a cylinder that is 5 mm long and 50 μm in diameter when lasers with mJ pulse energy are used.

The last term in Eqn. (2.19) is the dipole phase term which can be approximated [26] by $S \approx U_p\tau$, where $\tau = t - t_i$ represents the time spent by the electron in the continuum between tunnel ionization and recombination, and depends on the considered quantum path and on the laser intensity (and therefore on the position of the nonlinear medium with respect to the focus position of the fundamental beam). This intrinsic phase introduces an additional dispersion term proportional to the gradient of the laser intensity.
In particular, in the longitudinal direction, the dipole phase term is symmetric with respect to the laser focus, and competes with the antisymmetric Guoy phase.

Depending on the geometrical conditions, the contribution of one trajectory can be enhanced and the others reduced. For example, when the laser beam is focused

before the nonlinear medium, the phase variation induced by focusing is small and the selected trajectory is the one with the slowest phase variation (short trajectory). When the nonlinear medium is located around the position of the laser focus the contribution of the long paths increases. Moreover, it has been demonstrated that the harmonic emission due to the long paths is characterized by a larger divergence with respect to that due to the short paths, therefore it is possible to isolate the contributions of the short and long quantum paths simply adjusting the position of the nonlinear medium with respect to the laser focus and by spatial filtering [27]. By controlling the laser aperture, length, pressure and position of the gas medium, harmonic energies in the μJ range have been reached [28].

2.1.3 Polarization gating technique for the generation of IAPs

As reported in Section 2.1, during the HHG process, XUV radiation is periodically generated near the peaks of the IR driving field. Assuming a 800 nm driving field, electrons are emitted during a time window of ≈300 as centered around each peak of the electric field. As a result, XUV bursts are produced every half-optical cycle of the IR driving field, leading to the generation of attosecond pulse trains (APTs).
In order to isolate a single attosecond pulse a gating technique on the HHG process must be applied. These techniques rely on two different methods:

- spectral gating;
- temporal gating.

Spectral gating is based on the bandpass filtering in the cutoff region of the XUV emission obtained from carrier-envelope phase (CEP) stabilized IR pulses. Obtained results reported the generation and measurements of single 250-as XUV pulses, by selecting the cutoff harmonics at 93.5-eV energy within a 5-eV bandwidth generated in neon by a 5-fs linearly polarized fundamental pulse (λ = 750 nm) with stabilized CEP [29]. However, this method suffers from two serious disadvantages, that severely limit the process efficiency: it requires few-cycle driving laser pulses and selects only the cutoff region of the emitted spectrum. In fact, with this technique, the minimum pulse duration achievable is limited by the (≈10 eV) bandwidth of the selected cut-off harmonics, which prevents us reaching the sub-100-attosecond domain.

In order to overcome the mentioned problems, to obtain IAPs from broadband APTs we adopt a temporal gating process called polarization gating (PG).
The HHG process efficiency strongly depends on the polarization state of the driving pulse. From the three-step model, it is straightforward that the recombination process can occur only if the electron revisits the position of the parent ion, thus requiring a linearly polarized driving field. For a circularly polarized driving field, the electron acquires a transverse momentum and does not revisit the original position during its motion in the continuum, thus inhibiting the HHG process. Measurements of the HHG efficiency compared to the ellipticity of the driving field indicate

that the harmonic yield is reduced by a factor of 2 for an ellipticity ϵ_{thr} of 0.13 [30]. Shaping the incident pulse in a way that only half cycle of the driving radiation is linearly polarized is a method to isolate only one attosecond pulse from the whole train. This method bring the advantage that the whole XUV spectrum can be used to generate isolated pulses.

From the above property, Corkum et al. [31] proposed a method for the generation of IAPs based on the combination of two perpendicularly polarized pulses with frequencies ω_1 and ω_2 slightly detuned ($(\omega_1 - \omega_2) \ll (\omega_1 + \omega_2)/2$). Due to the coherent superposition of the two fields, the polarization state changes through the pulse being circularly polarized on the edges and linearly polarized at the center. For such a pulse, HHG is efficient only in the central temporal window whose duration depends on the duration of the two pulses and on the frequency differences between the two components. Tcherbakoff et al. [32] implemented this original idea using a single-color driving pulse and two birefringent plates as shown in Fig. 2.7(a).

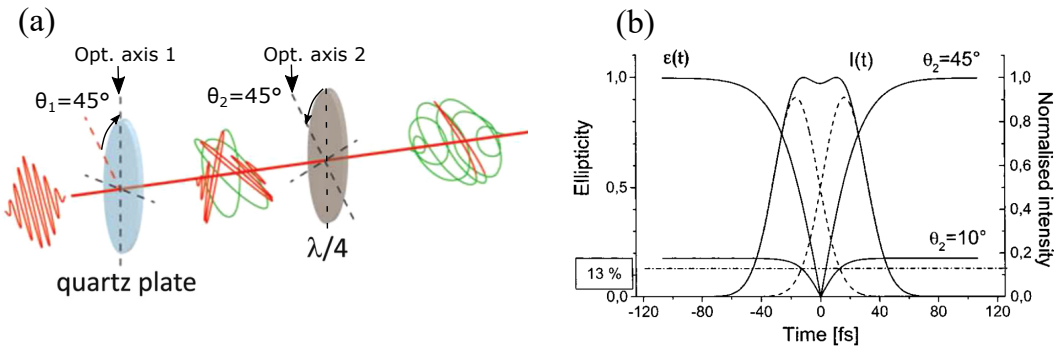

FIGURE 2.7: (a) Sketch of the optical setup for PG. (b) Pulse intensity profile (solid line) and time-dependent ellipticity for $\theta_1 = 45°$ and two angles ($\theta_2 = 45°$ and $\theta_2 = 10°$) of the zeroth-order quarter wave plate. The crossed polarized 35 fs Gaussian pulses separated by 31 fs are shown (dotted lines). The 13% ellipticity defining the gate width is indicated.

The first plate splits the incoming beam in two replica with perpendicular polarization, that, propagating through the birefringent material acquire a delay T_d given by the thickness of the first plate and by the difference of the group velocities between the ordinary and extraordinary axes. The second plate is a zero-order quarter wave plate oriented parallel to the incoming polarization direction that transforms the linear polarization of the leading and trailing edge in counter-rotating circular polarization, and the circular polarization of the central part in linear.

The final intensity envelope and polarization state of the pulse at the output of the second plate is shown in Fig. 2.7(b). At the center of the gating the gating field is zero and the pulse is linearly polarized. At the edges, the driving and gating fields have similar amplitude (and present a phase difference of $\pi/2$) thus leading to circular polarization. The duration of the central temporal gate δt_g where HHG can occur

can be estimated as [33]:

$$\delta t_g = 0.3 \frac{\epsilon_{thr} \tau_p^2}{T_d}, \tag{2.21}$$

where τ_p is the duration of the incoming pulse. When the temporal gate is shorter than half-optical-cycle, a single attosecond pulse can be generated.

This technique has been used for the first complete characterization of isolated attosecond pulses [11], using few-cycle pulses. An advantage of this technique is the possibility to generate XUV IAPs also in the plateau region of the harmonic spectrum and not only in the cutoff region. The PG technique requires few-cycle pulses in order to generate efficiently isolated attosecond pulses. For longer pulses, the condition $\delta t_g < T_0$ requires larger delay between the two perpendicularly polarized components of the incoming beam after the first plate, determining a low intensity of the electric field in the central temporal gate and, therefore, a low efficiency of the harmonic process.

Generally, the IR laser pulses envelopes for generating single isolated attosecond pulses are in the range of 3-30 fs, while for generating an attosecond pulse train, they can be as long as 100 fs.

2.2 Optics in the XUV and soft X-ray regions

XUV and soft X-ray energies (extending from 10 eV to several keV) determine large absorption coefficients for almost all materials, including air. Lenses can't be adopted for focusing, and very thin metal foils are used as band pass filters. Therefore, optical systems are basically constructed from reflective components at grazing incidence. This situation introduces strong aberrations in the image, as we know from visible light experience. The use of grazing incidence optics in the design of synchrotron beamlines and monochromators is discussed in articles by Namioka, Koike, Padmore, Howells, McKinney, and Underwood in the two-volume edition Vacuum Ultraviolet Spectroscopy edited by Samson and Ederer [34]. The use of grazing incidence optics in the design of synchrotron radiation beamlines is also described in the text by Peatman [35].

Here, in sub-Section 2.2.1 we describe the refraction index behaviour and the critical angle derivation when we deal with XUV and soft X-ray radiation. Sub-Section 2.2.2 gives the reflectivity performances of common materials adopted as coatings in these spectral regions.

2.2.1 Refraction index and critical angle

XUV and soft X-ray spectral regions are characterized by the presence of the primary atomic resonances and absorption edges for most of low and intermediate Z elements, where Z is the atomic number (the number of protons in the nucleus). Differently from visible range, we consider a complex refraction index, which deviates

only a small amount from unity that we can write it in the following form [36]:

$$n(\omega) = 1 - \delta(\omega) + i\beta(\omega) = 1 - \frac{n_a r_e \lambda^2}{2\pi} \underbrace{\left[\sum_s \frac{g_s \omega^2}{\omega^2 - \omega_s^2 + i\gamma\omega} \right]}_{f^0(\omega)}, \tag{2.22}$$

where n_a is the number density (atoms per unit volume), $r_e = e^2/(4\pi\epsilon_0 m_e c^2)$ is the classical electron radius, γ is a dissipative factor, g_s and ω_s are, respectively, the oscillator strengths and resonant frequencies.
Here we consider $f^0(\omega) = f_1^0(\omega) - i f_2^0(\omega)$ as the complex forward atomic scattering factor. The resulting expressions for the real and imaginary part of the refraction index are:

$$\delta(\omega) = \frac{n_a r_e \lambda^2}{2\pi} f_1^0(\omega) \tag{2.23}$$

and

$$\beta(\omega) = \frac{n_a r_e \lambda^2}{2\pi} f_2^0(\omega). \tag{2.24}$$

The refractive index $n(\omega)$ has a strong frequency dependence, in particular near the resonant frequencies ω_s , and is thus said to be dispersive. That is, waves of different frequencies propagate at different phase velocities and thus tend to separate (disperse). Equation (2.22) predicts both positive and negative dispersion, depending on whether the frequency ω is less or greater than ω_s . Typically for visible and infrared light, $dn/d\omega < 0$ and the medium is said to have normal dispersion. Instead, for XUV and soft X-rays $dn/d\omega > 0$, and the medium is said to have anomalous dispersion. As an example, Figure 2.8 illustrates the real and imaginary part of gold refraction index ($Z = 79$) obtained from Henke, Gullikson, and Davis [37]. As we can see δ and β are much less than unity in the XUV range.

For a wave propagating in a medium of uniform atomic density the phase velocity (the speed with which crests of fixed phase move) is not equal to c as in vacuum, but rather is modified to a value

$$v_\phi = \frac{c}{n(\omega)} = \frac{c}{1 - \delta + i\beta}. \tag{2.25}$$

Thus for visible light, with $\omega < \omega_s$, the refractive index is greater than unity, typically 1.5 or so for common glass, which corresponds to a relatively low phase velocity, less than c. Typical phenomena affected by low phase velocity propagation of visible wavelengths include reflection and refractive turning at tilted interfaces, focusing by lenses, dispersive separation of wavelengths by prisms, and total internal reflection.
For XUV/soft X-ray radiation, where $\omega > \omega_s$ for many of the atomic electrons, the refractive index is less than unity, but only slightly so, indicating that X-rays propagate in materials at phase velocities somewhat greater than in vacuum.

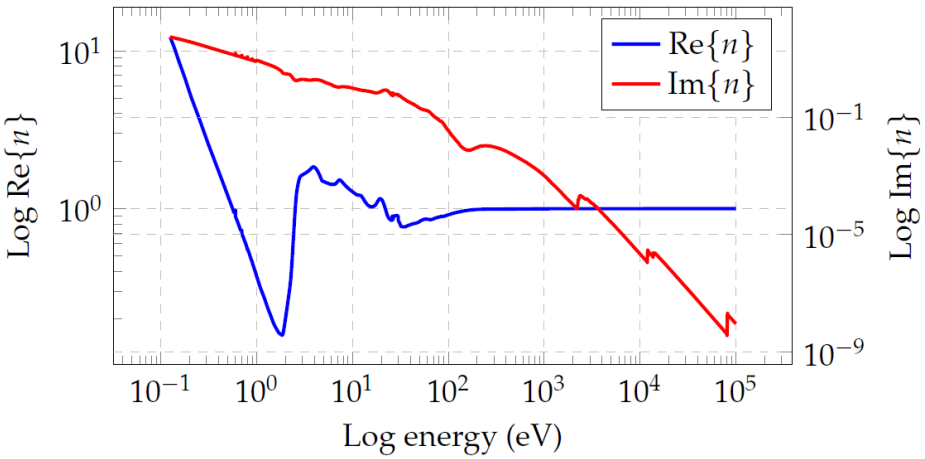

FIGURE 2.8: Real and imaginary part of the gold refraction index ($Z = 79$). Im$\{n\}$ shows the K and L_3 absorption edges at, respectively, 80.725 keV and 11.919 keV. Re$\{n\}$ shows multiple interband transitions at the ≈2.4 eV resonance energy.

This gives rise to the interesting and important phenomenon of total external reflection of X-rays, whereby reflection occurs with little absorption at glancing incidence from material interfaces. Note that although the phase velocity can be greater than c for X-rays, the group velocity, which represents energy flow, is less than c.
By introducing in the field expression of a plane wave the refraction index term of Eqn. (2.22) we obtain

$$\mathbf{E}(\mathbf{r},t) = \mathbf{E_0} e^{i(\mathbf{k}\cdot\mathbf{r}-\omega t)} e^{-i\frac{2\pi\delta}{\lambda}r} e^{-\frac{2\pi\beta}{\lambda}r}, \tag{2.26}$$

where the first exponential factor represents the phase advance of the wave being propagating in vacuum, the second factor represents the modified phase shift due to the medium, and the third term represents decay of the wave amplitude.
The wave decays with distance $\mathbf{r}$ into the material, with an exponential decay length

$$l_{abs} = \frac{\lambda}{4\pi\beta}, \tag{2.27}$$

which is very small in the XUV/soft X-rays.

Considering Snells law for a refractive index of $n \simeq 1-\delta$, we can express the critical grazing angle

$$\theta_c = \sqrt{2\delta} \propto \lambda\sqrt{Z}, \tag{2.28}$$

as the angle for which the refracted wave is parallel to the vacuum-material surface and does not penetrate into the material. To obtain a conveniently large critical angle, Eqn. (2.27) suggests the use of a relatively long wavelength and a higher Z material. In Table 2.1 are reported the critical energies for different materials adopted as coatings in the XUV/soft X-ray region assuming two different grazing angles: 5° and 10°. Since we want to work at grazing angles as high as possible in order to

have lower aberrations, typical used coatings for mirrors are gold and platinum at an energy lower than the critical one.

Critical energy (eV)		
Material	$\theta = 5^\circ$	$\theta = 10^\circ$
SiO_2	310.9	98.17
Al_2O_3	416.5	205.5
Ag	337.2	197.3
Au	615.1	180.5
Pt	694.7	180.5
Ir	735.4	183.4

TABLE 2.1: Critical energies for different materials adopted as coatings in the XUV/soft X-ray region assuming two different grazing angles: 5° and 10°.

2.2.2 Reflectivity and absorption

The reflected and refracted Fresnel coefficients in the case of s-polarization are

$$r_s = \frac{\cos\phi - \sqrt{n^2 - \sin^2\phi}}{\cos\phi + \sqrt{n^2 - \sin^2\phi}}, \tag{2.29}$$

and

$$t_s = \frac{2\cos\phi}{\cos\phi + \sqrt{n^2 - \sin^2\phi}}, \tag{2.30}$$

where ϕ is the wave vector incidence angle (with respect to the surface normal), such that $\phi = 90^\circ - \theta$. In the p-polarization case we have

$$r_p = \frac{n^2\cos\phi - \sqrt{n^2 - \sin^2\phi}}{n^2\cos\phi + \sqrt{n^2 - \sin^2\phi}}, \tag{2.31}$$

and

$$t_p = \frac{2n\cos\phi}{n^2\cos\phi + \sqrt{n^2 + \sin^2\phi}}. \tag{2.32}$$

Two cases of particular interest are normal incidence ($\theta = 90^\circ$) and grazing incidence ($\theta \leq \theta_c$) reflections.

In the normal incidence case the reflectivity (reflected to incident intensity) is

$$R_{s,p} \simeq \frac{\delta^2 + \beta^2}{4}. \tag{2.33}$$

Since δ and β are small, for large grazing angles, the reflectance in the XUV and soft X-ray range is small, especially for the energies that are higher than 35 eV, as shown in Fig. 2.9. Thus, to increase the reflectance, it is necessary to select a grazing angle θ lower than $\approx 20^\circ$.

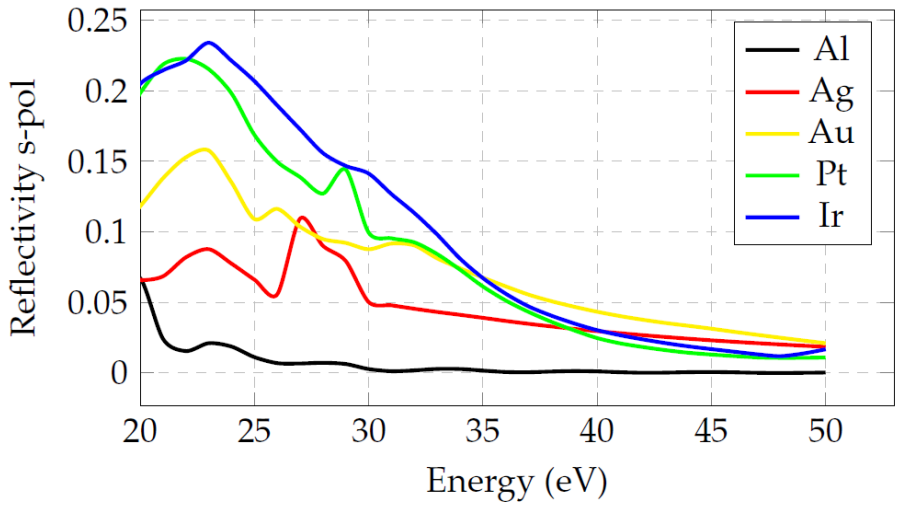

FIGURE 2.9: Normal incidence reflectivity for different coating materials (s-polarized light). Reflectivity has been calculated using Eqn. (2.29).

Just at the critical angle $\theta = \theta_c$ we can express the reflectivity as

$$R_{s,p,\theta_c} = \frac{1 - \frac{\sqrt{2\delta\beta}}{\delta+\beta}}{1 + \frac{\sqrt{2\delta\beta}}{\delta+\beta}}, \tag{2.34}$$

which is unity for $\beta/\delta = 0$, 0.20 for $\beta/\delta = 1/2$, and 0.17 for $\beta/\delta = 1$. Therefore Finite absorption (β) causes a rounding of the otherwise sharp angular dependence of reflectivity at the critical angle.

Figure 2.10 shows the reflectivity curves of different coating materials at a typical grazing angle $\theta = 3^\circ$.

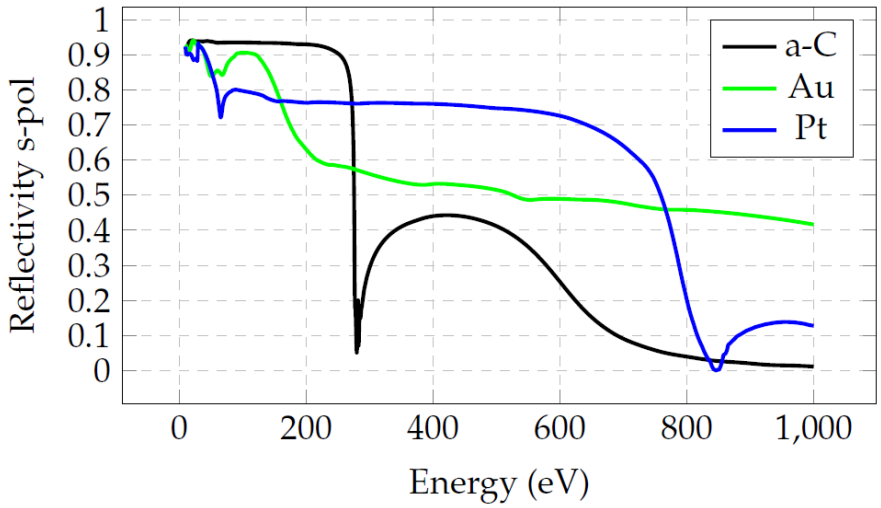

FIGURE 2.10: $\theta = 3°$ reflectivity for different coating materials (s-polarized light) in the entire XUV/soft X-ray range.

For energies lower than ≈284 eV (carbon K-edge) it is preferable to use carbon-coated optics since the reflectivity is almost constant and higher than 0.9. Instead for higher energies, nickel-coated optics are the best solution since they have a good reflectivity (≈0.75) up to 600 eV.

When we deal with HHG; after generation we have the IR laser co-propagating with the XUV. Even if carbon-coated optics have a high reflectivity in the XUV, they have a low one in the IR. Therefore they can not be used, since they will be damaged by the high absorption of the IR light. In this case gold-coated mirrors are the most adopted solution.

Due to total reflection, grazing incidence mirrors always exhibit a high and almost flat reflectivity and a linear spectral phase (within the bandwidth of the attosecond pulses/high-order harmonics). Moreover, the variation of the incidence angle of the rays on the mirror surface is by far too small to induce any changes of the coating response in space related to the angle of incidence. Therefore, the influence of the coating on the reflected pulses can be neglected. Only the losses due to non-unity reflectivity have to be considered.

2.3 Temporal characterization of ultrashort XUV and soft X-ray pulses

Femtosecond and attosecond temporal measurements of HHG pulses are affected by the fact that the responses of the detectors are much slower than the timescales of interest. Therefore, in order to obtain the full temporal characterization of attosecond bursts it is possible to follow a cross-correlation approach: the so-called "streak camera" method. In this kind of measurements the attosecond pulse ionizes a target

gas by single photon absorption, generating an electron wave-packet. If the process happens away from any atomic resonance, the electron wave packet is a perfect replica of the attosecond light pulse: the phase and amplitude of the XUV field are transferred to the photoelectron wave-packet. Direct information on the temporal structure of the XUV field can therefore be obtained by characterizing this electron wave-packet. It turns out that IR laser fields acting on attosecond electron pulses constitute ideal time-nonstationary filters. Therefore the acceleration and deceleration of the electrons by an intense laser field essentially acts as an ultrafast phase modulator on the electron wave-packet. Although the IR pulse duration is much longer than the attosecond XUV pulse, the phase modulation occurs in a small fraction of an IR cycle, which leads to a significant change of phase of the electron wave during the time that attosecond pulse last. This idea works for characterizing both attosecond pulse trains and single isolated attosecond pulses.
A simple sketch of this kind of measurement is depicted in Fig. 2.11. It is possible to demonstrate that the sequence of photo-ionization spectra as a function of the delay τ between the attosecond and the IR pulses contains enough information for the complete reconstruction of the temporal amplitude and phase of both the attosecond pulse and the streaking IR pulse at the same time. This technique is known as frequency-resolved optical gating for complete reconstruction of attosecond bursts (FROG-CRAB) [38].

In this Section a quntum theory description of the streak camera method is presented in sub-Section 2.3.1. Sub-Section 2.3.2 gives a detailed description of the FROG-CRAB technique.

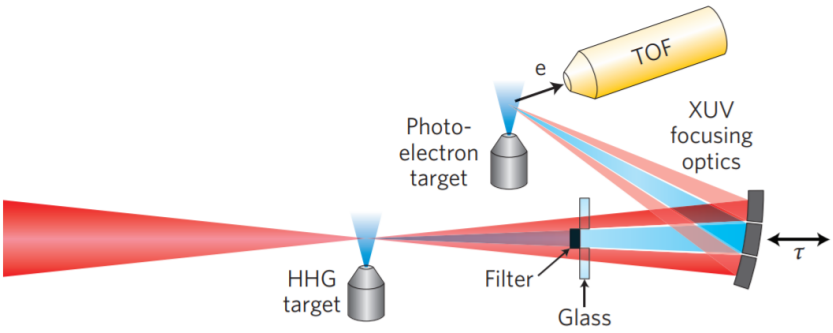

FIGURE 2.11: The attosecond pulses are generated in the HHG target, and refocused into the photoionization target. The laser pulse and the attosecond pulses are separated by an X-ray filter mounted on an annular glass pellicle. The time delay is controlled by moving the inner mirror. Photoelectrons are collected by the time-of-flight spectrometer (TOF). Sketch taken from [39].

2.3.1 XUV photoionization: quantum theory

The transition amplitude $a_{\mathbf{v}}$ of the electron from the ground state to the final continuum state $|\mathbf{v}\rangle$ can be expressed as:

$$a_{\mathbf{v}} = -i \int_{-\infty}^{\infty} dt d_{\mathbf{v}} \mathbf{E_{XUV}}(t) e^{i(W+I_p)t}, \tag{2.35}$$

where $\mathbf{v}$ is the momentum of the freed electron, $\mathbf{E_{XUV}}$ is the XUV electric field, $d_{\mathbf{v}}$ is the dipole transition matrix element from the ground state to the continuum state, W is the kinetic energy of the electron after the transition and I_p is the ionization potential of the atom. In the description of the photo-ionization process by the attosecond pulse, the photo-electron spectrum is given by $|a_{\mathbf{v}}|^2$.
It is possible to derive the expression of the transition amplitude $a_{\mathbf{v}}$ in the conditions of spatially overlapped and time-delayed XUV and gating IR pulses, by solving the Schrodinger equation for an atom in a classical electromagnetic field under certain approximations. These are (i) SAE approximation—the atom is considered hydrogen-like and multiple ionization is neglected; (ii) SFA—the electron in the continuum is influenced only by the external electric field, the influence of the parent ion Coulomb potential is neglected; (iii) only ground state and continuum states are considered—no influence of the atomic bound states is considered. With these approximations, the expression for $a_{\mathbf{v}}$ becomes [38, 40]

$$a_{\mathbf{v}}(\tau) = -i \int_{-\infty}^{\infty} dt e^{i\phi(t)} d_{\mathbf{p}(t)} \mathbf{E_{XUV}}(t-\tau) e^{i(W+I_p)t}, \tag{2.36}$$

where $\mathbf{p}(t) = \mathbf{v} + \mathbf{A}(t)$ is the instantaneous kinetic momentum, $\mathbf{A}(t)$ is the vector potential of the IR pulse, $\mathbf{d_p}(t)$ is the dipole matrix element between the ground state and the continuum state with momentum $\mathbf{p}(t)$ and $\phi(t)$ is the quantum phase acquired by the electron due to its interaction with the IR field. The phase it accumulates along its trajectory is thus temporally modulated by the dressing field. The latter can be written as follows:

$$\phi(t) = -\int_{t}^{\infty} dt' \left[\mathbf{v} \cdot \mathbf{A}(t') + \frac{\mathbf{A^2}(t')}{2} \right]. \tag{2.37}$$

For deriving the expression of the phase modulation, one can assume a linearly polarized IR pulse, whose electric field has the form $\mathbf{E_{IR}}(t) = \mathbf{E_0}(t)\cos(\omega_{IR}t)$ and whose temporal duration is long enough to assume the slowly varying envelope approximation. With these assumptions, the phase modulation $\phi(t)$ reads as the sum of three contributions [38]:

$$\phi_1(t) = -\int_{t}^{\infty} dt' \left[U_p(t) \right], \tag{2.38}$$

$$\phi_2(t) = \frac{\sqrt{8WU_p(t)}}{\omega_{IR}} \cos\theta \cos\omega_{IR}t, \tag{2.39}$$

$$\phi_3(t) = \frac{-U_p}{2\omega_{IR}} \sin 2\omega_{IR} t. \tag{2.40}$$

Here $U_p(t) = E_0^2(t)/(4\omega_{IR}^2)$ is the ponderomotive energy and θ is the angle between the electron velocity $\mathbf{v}$ and the polarization direction of the IR field. From the equations above, it appears that the phase modulation has two oscillating components: $\phi_2(t)$ and $\phi_3(t)$ at frequency ω_{IR} and $2\omega_{IR}$ respectively. Considering that often $W \gg U_p$, the phase term $\phi_2(t)$ is the leading one for all the observation angles θ, except for $\theta \approx \pi/2$, and has a slow angular dependence around $\theta = 0$.
The maximum energy shift of the measured photo-electron spectrum due to IR field, is given by the maximum value of $|\partial\phi/\partial t|$ [41]. Thus Eqn. (2.39) allows to identify the requirements on the phase modulation for the characterization of the electron wave-packet, leading to the correct reconstruction of the attosecond pulse: the phase modulation should be fast enough and the bandwidth of the phase modulation should be a large fraction of the bandwidth of the attosecond pulse to be characterized. In Fig. 2.12(a) it is shown an example of complete reconstruction of attosecond bursts (CRAB) trace: a sequence of photo-ionization spectra calculated as a function of the delay τ between the attosecond pulse and the IR streaking pulse. The photo-electron spectra (spectrogram) have been calculated for photo-ionization by a 315-as chirped XUV pulse (transform limited pulse duration: 250 as) in the presence of a 6-fs 800-nm streaking pulse. In this calculation, the photoelectron spectra are detected around $\theta \approx 0$. The trace oscillations correspond to the oscillation of the vector potential $\mathbf{A}(t)$ of the streaking IR pulse.

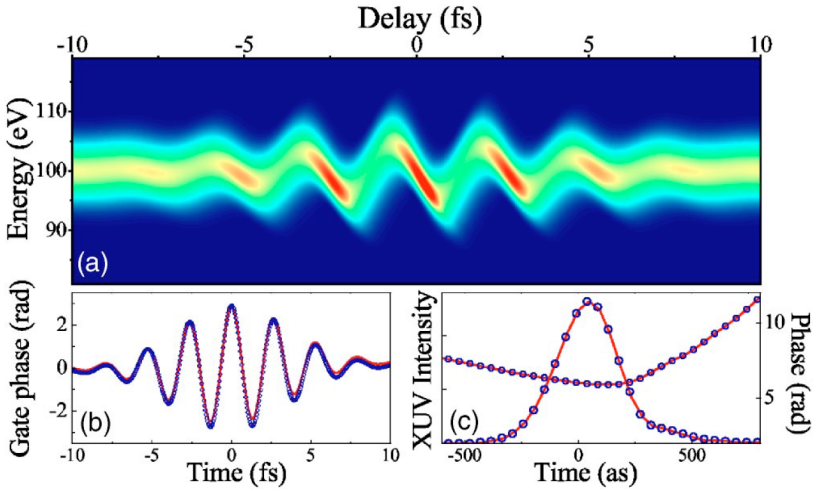

FIGURE 2.12: (a) CRAB trace of a single 315 as pulse having second- and third order spectral phases (Fourier limit = 250 as), gated by a Fourier limited 6-fs 800 nm laser pulse. (b) (c) A comparison of the exact as pulse and the laser induced gate phase (solid red line) with the corresponding reconstructions (blue dots) obtained from the CRAB trace after 100 iterations of the PCGPA algorithm [42]. The gate modulus $|G(t)|$ is constant and equals to 1. Sketch taken from [40].

2.3.2 FROG-CRAB retrieval

Frequency resolved optical gating for complete reconstruction of attosecond bursts (FROG-CRAB, or simply CRAB) is a very well established technique for the retrieval of the temporal structure of isolated attosecond pulses and offers the advantage of accurately recostructing arbitrary attosecond fields [38].
FROG-CRAB is inspired from frequency-resolved optical gating (FROG), a widely used technique for the full characterization of visible pulses [43]. In a FROG measurement the pulse to be characterized is decomposed in temporal slices due to a temporal gate $G(t)$, and then the spectrum of each slice is recorded. This provides a two-dimensional set of data, called a spectrogram or FROG trace, given by:

$$S(\omega,\tau) = \left| \int_{-\infty}^{\infty} dt G(t) E(t-\tau) e^{i\omega t} \right|^2, \tag{2.41}$$

where $E(t)$ is the field of the unknown pulse and τ is the delay between the gate and the pulse. The gate may either be a known function of the pulse, as in most implementations of FROG, or an unrelated, and possibly unknown, function. Various iterative algorithms can then be used to extract both $E(t)$ and $G(t)$ from $S(\omega,\tau)$. The principle of FROG-CRAB can be derived by comparing the Eqn. (2.36) with Eqn. (2.41), i.e. the spectrum $S(\omega,\tau)$ with the photoelectron spectrum $|a_{\mathbf{v}}(\tau)|^2$. This comparison shows that, by scanning the delay τ, the dressing laser field can be used as a temporal phase gate $G(t) = e^{i\phi(t)}$ for FROG measurements on photoelectron wave packets generated by attosecond fields. The full characterization of the wave packets provides all the information on the temporal structure of the XUV attosecond pulses as well as the unknown gate fields. Therefore the iterative principal component generalized projections algorithm (PCGPA) [42] can be used to retrieve the amplitude and phase of the pulses as shown in Figs. 2.12(b) and 2.12(c).

Chapter 3

XUV and soft X-ray efficiency performances of ultrafast single-grating monochromators

3.1 Introduction

The development of new experimental techniques for determining the electronic structure of materials in the XUV and soft X-ray spectral regions has been possible with the wide availability of free-electron lasers (FELs) and table-top high harmonics (HHs) sources [44], providing highly intense, short-pulsed radiation.
Instrumentation capable of maintain the few-femtoseconds or even attosecond time scale of HHs generated pulses is needed in order to perform high-resolution pump-probe experiments and for maximizing the instantaneous power during chemical interactions. In particular, the selection of a single harmonic with the preservation of the pulse duration is a crucial task.
Harmonic spectral selection can be obtained with the use of a normal incidence multilayer mirror, which does not alter the pulse duration up to fractions of a femtosecond [45]. Although high efficiency performances and a wide range of focalization schemes, the main drawback is the lack of tunability, and therefore the necessity of using different optics to cover a wide spectral region. One possible solution to the last requirement is the use of an ordinary diffraction grating. In this case, the diffraction mechanism itself is the main effect that alters the duration of the pulse, since the pulse-front of the incident radiation is tilted after the diffraction by the difference of the optical paths of rays at the same wavelength diffracted by adjacent grating grooves. This effect generates a pulse-front tilt that can be considered negligible for picosecond or longer pulses, but it is dramatic for femtosecond ones. In fact, as an order-of-magnitude estimate, a grating illuminated over 10 mm with 1200 grooves/mm uses $N = 12,000$ grooves. At a XUV wavelength of 10 nm and first diffraction order ($m = 1$), the optical path difference is $\Delta_{OP} = Nm\lambda = 120\ \mu m$ which corresponds to a time delay of $\Delta t = \Delta_{OP}/c \approx 400$ fs.
As we will see in Chapter 4, a solution could be the design of grating monochromators that do not alter the temporal duration of ultrafast pulses by using two gratings

in a time-delay compensated (TDC) configuration [46]. The main drawback of these configurations is the use of two gratings, leading to a complexity increase and an efficiency reduction of the instrument.
A single-grating may be used for the spectral selection of ultrafast pulses at the first diffraction order without altering in a significant way the pulse duration, provided that the number of illuminated grooves is equal to the grating resolving power $R = \lambda/\Delta\lambda$. In fact, the minimum number of illuminated grooves N_{min} to support a bandwidth $\Delta\lambda$ at wavelength λ can be found using the relation valid for gratings $N_{min} = \lambda/\Delta\lambda$. Therefore the minimum pulse-front tilt at half-width, for a given bandwidth $\Delta\lambda$ is

$$\Delta\tau_{G,min} \simeq \frac{1}{2}\frac{\lambda N_{min}}{c} = 0.5\frac{\lambda^2}{c\Delta\lambda}, \tag{3.1}$$

which is comparable with the Fourier limit of a Gaussian pulse with no phase modulation

$$\Delta\tau_F = \frac{2\ln 2}{\pi}\frac{\lambda^2}{c\Delta\lambda} \simeq 0.44\frac{\lambda^2}{c\Delta\lambda}. \tag{3.2}$$

Assuming that a post-processed HHs XUV pulse is tipically close to its transform limit, if it passes through a monochromator with minimum pulse-front tilt the obtained pulse duration is the convolution the two previous equations.
Here we discuss the two grating configurations that can be used to realize ultrafast monochromators: the classical diffraction mount (CDM) and the off-plane mount (OPM) [47]. They originate from the CzernyTurner design, theoretically free of geometrical aberrations, if it uses two parabolic mirrors for collimation and refocusing. The OPM is normally used in the 10-83 nm wavelength range to minimize the pulse stretch due to diffraction (typically well below 100 fs), although with medium-to-low spectral resolution ($\lambda/\Delta\lambda < 500$). The CDM, on the other hand, gives a longer time response (in the range of few hundreds of femtoseconds), but a definitely higher spectral resolution. The main advantage of the OPM when compared with the CDM is the higher diffraction efficiency, which is close to the coating reflectivity at the same altitude angle [48, 49]. The OPM also introduces a smaller XUV pulse-front tilt.

In this chapter, a comparison in terms of throughput between the two geometries has been done. Section 3.2 reports the classical and off-plane geometries layouts and working principle. In Section 3.3 the two experimental setups implemented for the diffraction efficiency measurements are reported. In Section 3.4, the algorithm employed by the GSolver software to perform the efficiency simulations of the tested gratings is analyzed. Section 3.5 reports the derivation of the gratings simulation parameters from the Atomic Force Microscope (AFM) scan results. Finally, Section 3.6 gives a comparison of simulation and experimental results.

3.2 Classical and off-plane geometries for ultrafast monochromators

The CDM design is represented in Fig. 3.1 and consists of three optical elements: a first mirror which collimates the light on a plane diffraction grating with uniform spaced grooves oriented perpendicular to the incidence plane, and a second mirror acting as focusing element on a vertical exit slit placed on the image plane. The mirrors have equal incidence angles and unity magnification (see Appx. A.1.1) to minimize aberrations at the output. The wavelength selection is performed by rotating the grating around an axis, which is tangent to the surface, passes through the grating center, and is parallel to the grooves. With this layout, the entrance and output arms of the grating have fixed directions. Therefore the subtended angle $k = \alpha - \beta$ is constant, naming α and β, respectively, the grating positive incidence and negative diffraction angles. After some manipulations of the grating equation $\sin\alpha + \sin\beta = m\lambda\sigma$ where σ is grating density; the relation between the grating incidence angle and the desired wavelength becomes:

$$\alpha = \frac{k}{2} + \arcsin\left[\frac{m\lambda\sigma}{2\cos\left(\frac{k}{2}\right)}\right]. \tag{3.3}$$

The number of illuminated grooves is $N_c = 2w\sigma/\cos\alpha$, where w is the half-width section of the collimated beam. N_c is smaller in case of $m = -1$, i.e. the external diffracted order with $\alpha < \beta$. Therefore, the grating should be operated in the external order if a lower pulse-front tilt is desired.

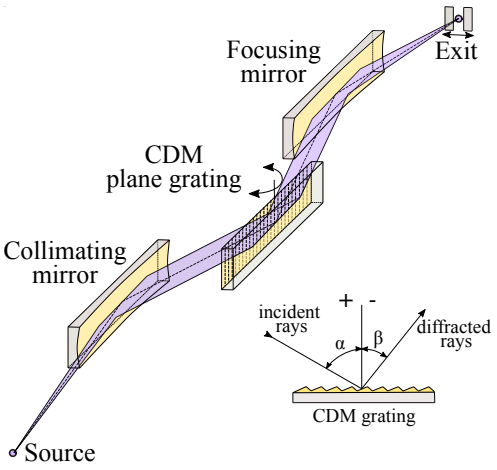

FIGURE 3.1: Layout of a plane-grating monochromator in CDM geometry.

On the other hand, the OPM is shown in Fig. 3.2. The design is similar to the CDM, and it consists of two mirrors responsible of the collimating and focusing actions, with a plane grating in between, but this time, having grooves oriented almost parallel to the incidence plane. As for CDM, the grating performs the wavelength

selection through the rotation around an axis which is tangent to the grating surface, passes through its center, and is parallel to the grooves. Here the exit slit has to be placed horizontally since the diffracted orders are distributed over a semi-cone with altitude angle γ. The grating equation is $\sin\gamma\,(\sin\mu + \sin\nu) = m\lambda\sigma$, where μ and ν are the incidence and diffraction azimuth angles, respectively. As a consequence of fixed optical elements positions $\nu = \mu$ and the equation becomes $2\sin\gamma\sin\mu = m\lambda\sigma$. Therefore, in this case the spectral selection can be performed by following the relation:

$$\mu = \arcsin\left(\frac{m\lambda\sigma}{2\sin\gamma}\right). \tag{3.4}$$

The number of illuminated grooves is $N_o = 2w\sigma/\cos\mu \simeq 2w\sigma$, where the approximation holds for small $\mu \leq 15^\circ$ and is fully verified for low resolution configurations. The grating in the OPM can be used indifferently at the orders m $= \pm 1$, since this does not affect the illuminated area.

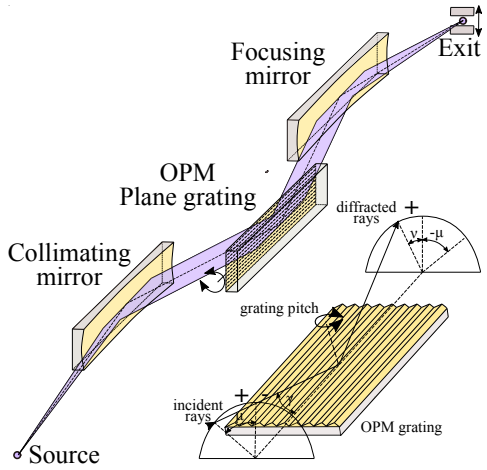

FIGURE 3.2: Layout of a plane-grating monochromator in OPM geometry.

3.3 Experimental setup for efficiency measurements

Since the throughput of monochromators is dominated by the diffraction efficiency of gratings, a comparison between theoretical and experimental results has been done for the two configurations described before. The efficiency of blazed gold-coated plane gratings, respectively in CDM and OPM has been measured in the 41–310 eV region using the Circular Polarization beamline (CiPo) [50] at ELETTRA Synchrotron. The gratings are commercially manufactured by Newport-Richardson Gratings^{TM}, and are obtained from a master grating ruled mechanically, which is then used to create a mould for replicating other gratings. The groove shape is transferred using a thin layer of liquid resin that is hardened while in contact with the master surface as represented in Fig. 3.3.

The CiPo beamline provides to the users a wide energy range between 5–1000 eV,

with high flux and control of the light polarization (from circular to linear). The photon beam is generated by the Electromagnetic Elliptical Wiggler (EEW) using both undulator and wiggler modes of operation. Under wiggler conditions the EEW operates for different values of the vertical and horizontal magnetic field providing an elliptically polarized radiation and a continuum soft X-ray emission spectrum extending from 40 eV to more than 1000 eV. When the EEW approaches the undulator mode, it emits a spectrum of harmonics in the low photon energy side (less than 40 eV), whose fundamental energy is at 4.5 eV. In plane linear polarization of the emitted radiation is also available in wiggler mode by switching off the horizontal (vertical) magnetic field, producing linearly polarized radiation parallel (perpendicular) to the orbit plane of electrons.

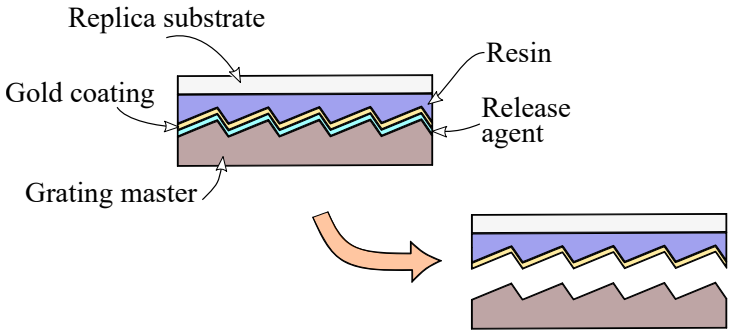

FIGURE 3.3: Master grating replication procedure. First, a thin and uniform release agent is applied to the surface of the master; a metallic (aluminum or gold) coating is then applied (100 nm); finally, the replica blank is cemented from above using a resin of 10 *mu*m thick that hardens under UV exposure or over time. Once the resin is cured, the grating is separated at the parting agent layer, leaving the hardened resin in the shape of the grooves, with the metal coating adhered to the top.

After the broadband generated radiation, the beamline is basically made up of two monochromators, that share the entrance and exit slits as well as the pre- and post-focusing optics. The normal incidence monochromator (NIM), covers the photon energy range of 5–35 eV using two different holographic gratings (gold and aluminum). The spherical grating monochromator (SGM), covers the energy range of 30–1000 eV, working in Padmore-type configuration, being equipped with a variable angle plane mirror and four spherical gratings.
As represented in Fig. 3.4, the gratings have been positioned on a X-rays reflectometer [51] that has been installed at the output of the beamline. The precision of the combined positioning of grating sample and detector (photodiode) angles is better than 0.01°. The beam section on the sample plane is in the range 200–400 μm.
The sample mounting inside the reflectometer allows five degrees of freedom: the three translations along the Cartesian coordinates, and the rotation around two axes: the first perpendicular to the direction of the incoming beam (for CDM measurements), and the second parallel to it (for OPM measurements). The detector can only scan along a circumference parallel to the incidence plane. By switching off

the wiggler horizontal magnetic field, a linearly s-polarized (TE) radiation has been obtained.

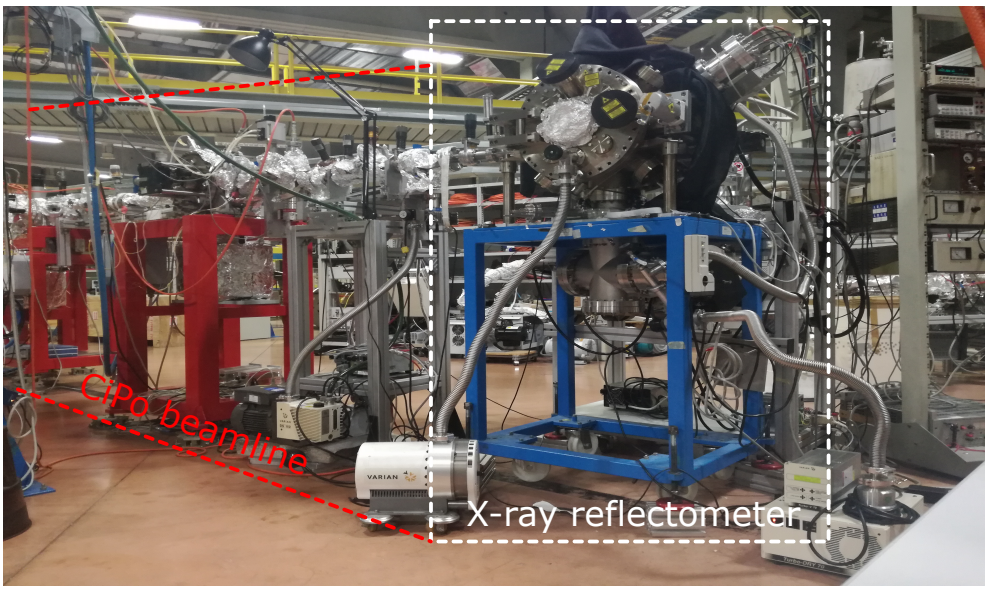

FIGURE 3.4: Overall experimental setup installed at CiPo beamline.

3.3.1 Scanning procedure

The condition for maximum efficiency is reached when the relationship between the incidence angle of the light and the mth-order diffracted light angle describes a specular reflection with respect to the groove surface. In case of blazed profiles with blaze angle δ, the condition is fulfilled when $\delta = (\alpha + \beta)/2$ in the CDM and $\delta = \mu$ in the OPM. We assume in the following that the gratings are operated in the first diffracted order (m = 1).
In the CDM case, the theoretical maximum efficiency is obtained at the subtended angle

$$k_{me} = 2 \arccos\left(\frac{\lambda\sigma}{2\sin\delta}\right), \tag{3.5}$$

or equivalently, at the specific incidence and diffraction angles α_{me} and β_{me} obtained by Eqn. (3.3). As represented in Fig. 3.5(a), for each photon energy of interest, the grating has been rotated of θ_{me} = 90° - α_{me} with respect to the incident beam.

The full diffracted signal has been acquired through an angular scan of the detector. Moreover, the adjacent angles of α_{me} has been scanned to find the most intense first diffraction maximum. As an example, one of the scans performed at three different incidence angles is shown in Fig. 3.6. The first-order diffracted signal is maximum between 83° and 84°. As can be seen, the effect of considering a slightly different angle from α_{me} leads to a first-order diffracted signal decrease. At each photon energy change, the direct beam has been acquired.

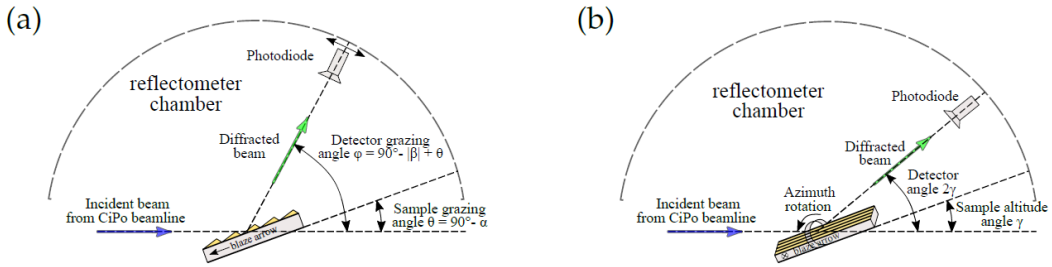

FIGURE 3.5: Reflectometer configuration setup. (a) CDM efficiency measurements. Once the grating grooves are perpendicular to the beam, the variables are θ and φ. (b) OPM efficiency measurements. Once the grating grooves are parallel to the beam, the variables are γ and the azimuth $\mu = \nu$.

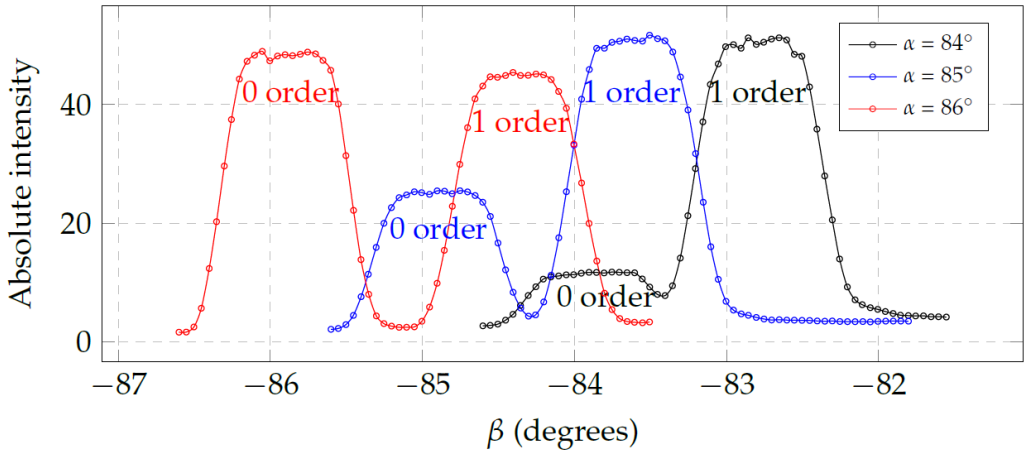

FIGURE 3.6: Grating 180 gr/mm zero and first diffracted orders β scan at 103 eV photon energy in the CDM reflectometer setup for three different α angles near α_{me}.

Analogously, in the OPM, the altitude angle that satisfies the maximum efficiency is

$$\gamma_{me} = \arcsin\left(\frac{\lambda\sigma}{2\sin\delta}\right), \tag{3.6}$$

with the azimuth angle μ_{me} obtained by Eqn. (3.4). As represented in Fig. 3.5(b) for each photon energy, grating and detector have been rotated, respectively, of γ_{me}, and $2\gamma_{me}$ with respect to the incident beam. As for CDM, at each photon energy change, the direct beam has been acquired. The grating efficiency was calculated as the ratio of the diffracted intensity (with background subtraction) to the incident-beam intensity. In Tab. 3.1, the characteristics of the four tested gratings are shown.

Groove density (gr/mm)	**Blaze angle** (deg.)	**Anti-blaze angle** (deg.)	**Groove height** (nm)	**Geometry**
180	0.77	89.23	74.5	CDM
600	2	88	58.1	CDM
1800	9.3	80.7	87.4	OPM
2400	10.36	79.64	73.6	OPM

TABLE 3.1: Properties of the four gold-coated tested gratings.

3.4 The GSolver grating model

GSolver is a full vector implementation of a class of algorithms known as rigorous coupled-wave (RCW) analysis. These algorithms give a numerical solution of Maxwell's equations for a periodic grating structure that lies at the boundary between two homogeneous linear isotropic infinite half spaces: the substrate, and the superstrate. The solution is rigorous in the sense that the full set of vector Maxwell's equations are solved with only the following two simplifying assumptions: (i) a piecewise-linear approximation to the grating construction, and (ii) a truncation parameter for the Fourier series representation of the permittivity (and impermittivity) within each grating layer. GSolver is set up to work with linear isotropic homogeneous materials. Here, a grating is specified by a series of thin layers. Each layer consists of (box shaped) regions of constant indices of refraction. With reference to Fig. 3.7, the solution i.e., the strength of the electric or magnetic field of the waves is projected onto some periodic basis in the x-direction, but with an unknown dependence on z. The task is to determine the z-dependence by ensuring that the total field satisfies the boundary conditions on the grating surface and at infinity. The RCW method assumes a rectangular groove profile, so that the boundary conditions are simplified: this implies that the tangential and normal field components at the grating interface are purely along either the x- or z-direction. Therefore an eigenvalue technique can be used instead of a full numerical integration along z, with a reduction of the problem to an algebraic solution.
In the XUV/soft X-ray range, metals behave as absorbing, weak dielectrics with a complex refractive index $n = (\epsilon_r)^{1/2} \simeq 0.99 + i0.01$. Moreover, at grazing incidence, polarization effects are minimized; there turns out to be very little difference between measured and calculated results for transverse electric (TE) and transverse magnetic (TM) polarization.
In the z direction, there are three distinct regions:

- Region 1: vacuum, with uniform relative permittivity $\epsilon_{r,1} = 1$;
- Region 2: intermediate region where the permittivity changes as a function of the x position: $\epsilon_{r,2}$ is either $\epsilon_{r,1}$ or $\epsilon_{r,3}$;
- Region 3: below the grooves, with a uniform relative permittivity $\epsilon_{r,3}$.

Since all measurements have been performed on gold coated diffraction gratings, the permittivity in region 3 is $\epsilon_{r,3} = \epsilon_{r,Au}$ and has been obtained from Ref. [37].

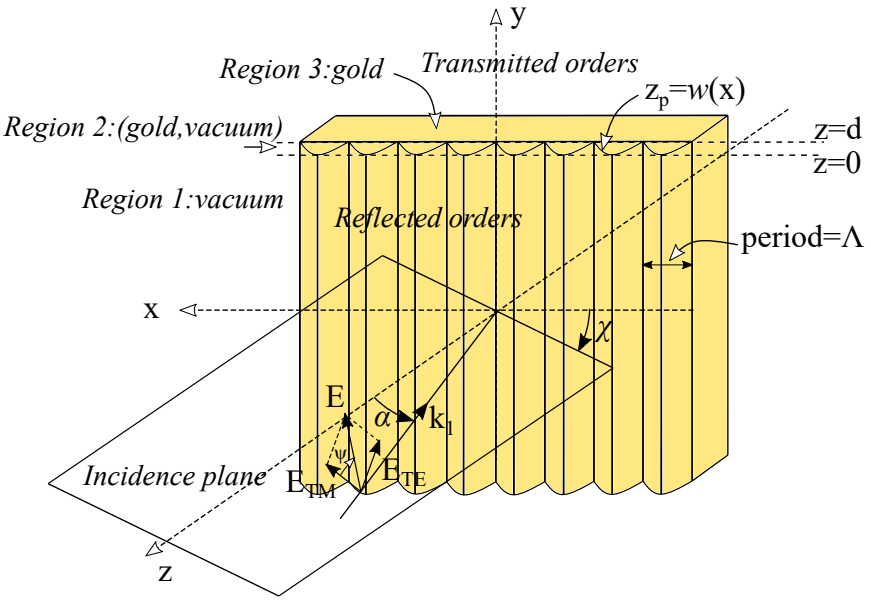

FIGURE 3.7: Three-dimensional model of the x-direction periodic grating with a generic incidence plane orientation χ.

Without any loss of generality, the planar grating has periodicity along the grating vector **K**. Furthermore, **K** may have any arbitrary orientation with respect to the plane of incidence. This is the general case in which the grating vector is not in the plane of incidence, and is useful to calculate the efficiency in the conical diffraction mount, i.e. when $\chi = 90°$.
Therefore, without any loss of generality, the following assumptions are used: (i) the boundary normal is in the z-direction, (ii) the grating vector is in the x-direction ($\mathbf{K} = K_x\hat{x}$) having $K_x = \frac{2\pi}{\Lambda}$ (as in Fig. 3.7), (iii) α is the angle of incidence (the angle between the wave vector $\mathbf{k_1}$, and the z axis), and (iv) the plane of incidence makes an angle χ with respect to the x axis.
The grating may be characterized by a periodic complex relative permittivity expandable in Fourier series as

$$\epsilon_r(x) = \sum_{h=-\infty}^{\infty} \epsilon_{r,h} \exp\{(ihK_x x)\}. \tag{3.7}$$

The quantity $\epsilon_{r,h}$ is the h-th Fourier component of the complex relative permittivity. In region 1, the incident normalized electric-field for a plane-wave is

$$\mathbf{E_{inc}} = \hat{u} exp(i\mathbf{k_1} \cdot \mathbf{r}), \tag{3.8}$$

with

$$\mathbf{k_1} = k_1 \left(sin\alpha cos\chi + sin\alpha sin\chi - cos\alpha\right). \tag{3.9}$$

Here $k_1 = k(\epsilon_{r,1})^{1/2}$, $k = \frac{2\pi}{\lambda}$, λ is the free-space wavelength, and $\hat{u}$ is the polarization

unit vector, characterized by the angle ψ.
The general approach to solve the exact electromagnetic boundary value problem associated with the diffraction grating is to find solutions that satisfy Maxwell's equations (or the corresponding wave equations) in each of the three regions and then to match the tangential electric and magnetic fields at the two boundaries ($z = 0$ and $z = d$). In the general three-dimensional problem, the polarization can't be decomposed into TE and TM components, and therefore we can't treat each of these separately for combining the results to obtain the total diffracted field. All the field components are coupled to one another, and solutions for all the electric-field and magnetic-field components have to be obtained simultaneously. The normalized total vector electric field in region 1 ($z < 0$) and in region 3 ($z > d$) can be expressed as

$$\mathbf{E_1} = \mathbf{E_{inc}} + \sum_{n=-\infty}^{\infty} \mathbf{R_n} exp(i\mathbf{k_{1,n}} \cdot \mathbf{r}) \tag{3.10}$$

and

$$\mathbf{E_3} = \sum_{n=-\infty}^{\infty} \mathbf{T_n} exp[i\mathbf{k_{3,n}} \cdot (\mathbf{r} - \mathbf{d})], \tag{3.11}$$

where $\mathbf{R_n}$ is the normalized vector electric field of the n-th backward-diffracted (reflected) wave in region 1 with wave vector $\mathbf{k_1}, \mathbf{n}$ and $\mathbf{T_n}$ is the normalized vector electric field of the n-th forward-diffracted (transmitted) wave in region 3 with wave vector $\mathbf{k_3}, \mathbf{n}$. For plane waves, the condition $\mathbf{k_{1,n}} \cdot \mathbf{R_n} = \mathbf{k_{3,n}} \cdot \mathbf{T_n} = 0$ must be satisfied. Phase matching requires that

$$\mathbf{k_{l,n}} = k_{x,n}\hat{x} + k_y\hat{y} + k_{z,l,n}\hat{z}, \tag{3.12}$$

where

$$k_{x,n} = k_1 sin\alpha cos\chi - nK_x, \tag{3.13}$$

$$k_y = k_1 sin\alpha sin\chi, \tag{3.14}$$

$$k_{z,l,n} = \left(k_l^2 - k_{x,n}^2 - k_y^2\right)^{1/2}, \tag{3.15}$$

for l = 1..3 (the region index) and $k_l = k(\epsilon_{r,l})^{1/2}$. The z-component of the wave vector, $k_{z,3,n}$, is either positive real (a propagating wave) or negative imaginary (an evanescent wave). Likewise, for region 1, $k_{z,1,i}$ is either negative real (propagating wave) or positive imaginary (evanescent wave). The wave vectors of all diffracted orders (forward and backward) have the same y-component i.e. perpendicular to the grating vector. This is more clearly shown in Fig. 3.8, in which the backward-diffracted waves are represented.

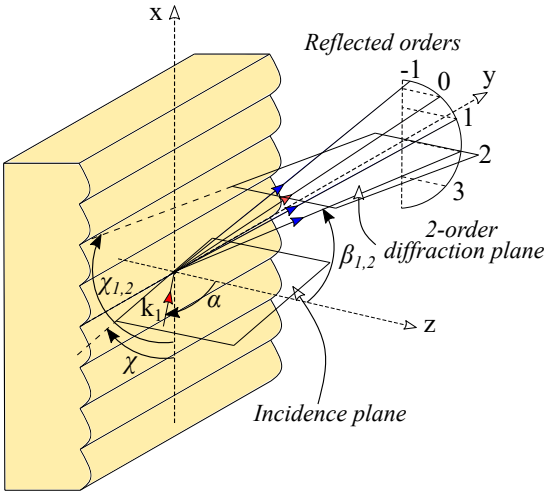

FIGURE 3.8: Geometry of the backward-diffracted (reflected) wave vectors showing the conical nature of diffraction. All diffracted waves have wave vectors that are equal in magnitude and have the same y-component.

The angle of diffraction for the n-th order is given by

$$\tan \beta_{l,n} = \left(k_{x,n}^2 + k_y^2\right)^{1/2} / k_{z,l,n} \tag{3.16}$$

and the angle of inclination of the output plane is given by

$$\tan \chi_n = k_y / k_{x,n}. \tag{3.17}$$

The plane of diffraction, in general, is different for each diffracted order. In the limiting case when the plane of incidence is the $x - z$ plane, $k_y = 0$ and all diffracted orders lie in the same plane (the plane of incidence). However, if the plane of incidence does not contain the grating vector, the k_y is a nonzero constant. The wave vectors of all diffracted orders (forward and backward) have the same y-component (perpendicular to the grating vector). The magnitude of the wave vectors for all diffracted waves is k_l. The two last conditions mean that the wave vectors lie on the surface of a cone (with the cone axis in the y direction); hence the terminology "conical diffraction" for this general three-dimensional geometry. The cone axis is in the $\hat{n}$ x $\hat{x}$ direction, where $\hat{n}$ is the normal to the grating boundary.
The magnetic-field vector in regions 1 and 3 can be obtained by using the Maxwell equation

$$\mathbf{H} = \frac{i}{\omega \mu_0} \nabla \times \mathbf{E}. \tag{3.18}$$

In the modulated region 2 ($0 < z < d$), the electric and magnetic fields may be expressed as Fourier expansions in terms of the space-harmonic fields as

$$\mathbf{E_2} = \sum_{n=-\infty}^{\infty} \left[S_{x,n}(z)\,\hat{x} + S_{y,n}(z)\,\hat{y} + S_{z,n}(z)\,\hat{z}\right] \exp\{(i\boldsymbol{\sigma_n} \cdot \mathbf{r})\}, \tag{3.19}$$

$$\mathbf{H_2} = \left(\frac{\epsilon_0}{\mu_0}\right)^{1/2} \sum_{n=-\infty}^{\infty} \left[U_{x,n}(z)\,\hat{x} + U_{y,n}(z)\,\hat{y} + U_{z,n}(z)\,\hat{z}\right] \exp\{(i\boldsymbol{\sigma_n}\cdot\mathbf{r})\}, \tag{3.20}$$

where

$$\boldsymbol{\sigma_n} = k_{x,n}\hat{x} + k_y\hat{y} + nK_z\hat{z}. \tag{3.21}$$

The x- and y- components of $\boldsymbol{\sigma_n}$ are determined by the phase-matching condition; the z-component K_z is arbitrary.
$\mathbf{S_n}(z)$ and $\mathbf{U_n}(z)$ are the normalized amplitudes of the n-th space-harmonic vector electric and vector magnetic fields such that $\mathbf{E_2}$ and $\mathbf{H_2}$ satisfy the appropriate wave equations derived from Maxwell's equations in the grating region.

3.4.1 The RCW algorithm in the modulated region

In the general three-dimensional vectorial problem under consideration, all the electric and magnetic space-harmonic fields are coupled to one another. Therefore, rather than solve two vector wave equations, it is more convenient and straightforward to solve Maxwell's equations

$$\nabla \times \mathbf{E_2} = -i\omega\mu_0\mathbf{H_2} \tag{3.22}$$

$$\nabla \times \mathbf{H_2} = i\omega\epsilon_0\epsilon_r(x)\,\mathbf{E_2} \tag{3.23}$$

directly. Substituting Eqns. (3.19) and (3.20) into these two expressions, and eliminating the components of $\mathbf{E_2}$ and $\mathbf{H_2}$ normal to the boundary, we obtain a set of four first-order coupled-wave equations:

$$\frac{dS_{x,n}}{dz} = -i\left\{nK_zS_{x,n} + \left(\frac{k_{x,n}}{k}\right)\sum_{p=-\infty}^{\infty} a_{r,n-p}\left[k_{x,p}U_{y,p} - k_yU_{x,p}\right] + kU_{y,n}\right\}, \tag{3.24}$$

$$\frac{dS_{y,n}}{dz} = -i\left\{nK_zS_{y,n} + \left(\frac{k_y}{k}\right)\sum_{p=-\infty}^{\infty} a_{r,n-p}\left[k_{x,p}U_{y,p} - k_yU_{x,p}\right] - kU_{x,n}\right\}, \tag{3.25}$$

$$\frac{dU_{x,n}}{dz} = i\left\{-nK_zU_{x,n} + \left(\frac{k_{x,n}}{k}\right)\left[k_{x,p}S_{y,n} - k_yS_{x,n}\right] + \sum_{p=-\infty}^{\infty}\epsilon_{r,n-p}S_{y,p}\right\}, \tag{3.26}$$

$$\frac{dU_{y,n}}{dz} = i\left\{-nK_zU_{y,n} + \left(\frac{k_{y,n}}{k}\right)\left[k_{x,p}S_{y,n} - k_yS_{x,n}\right] - \sum_{p=-\infty}^{\infty}\epsilon_{r,n-p}S_{x,p}\right\}, \tag{3.27}$$

where $p = n - h$ and $a_{r,h}$ is the h-th coefficient of the Fourier expansion of $\epsilon^{-1}(x,z)$ in the form

$$\epsilon_r^{-1}(x) = \sum_{h=-\infty}^{\infty} a_{r,h}\exp\{(ihK_xx)\}. \tag{3.28}$$

The grating is described by the profile function $z_p = w(x)$, which has a minimum at $z = 0$, a maximum at $z = d$, and is periodic in Λ:

$$z_p = w(x) = w(x + \Lambda). \tag{3.29}$$

The exact groove profile is required to determine $\epsilon_r(x)$ as a function of position. For a profile of arbitrary shape, at any height $(0 < z < d)$, $\epsilon_r(x;\tilde{z})$ is a periodic step function going from $\epsilon_{r,1}$ to $\epsilon_{r,3}$. We can then determine a Fourier expansion for $\epsilon_{r,2}$ that applies inside the grooves, as represented in Fig. 3.9.

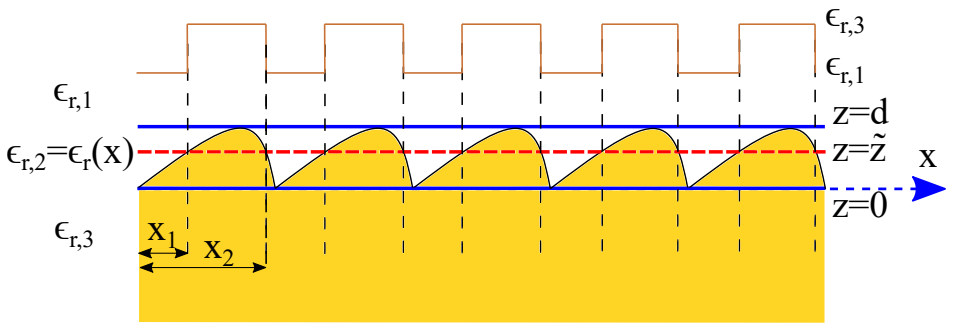

FIGURE 3.9: The $\epsilon_{r,2}$ function for a simple groove profile. At any height $(0 < \tilde{z} < d)$, the $\epsilon_r(x;\tilde{z})$ function is a periodic step function going from $\epsilon_{r,1}$ to $\epsilon_{r,3}$.

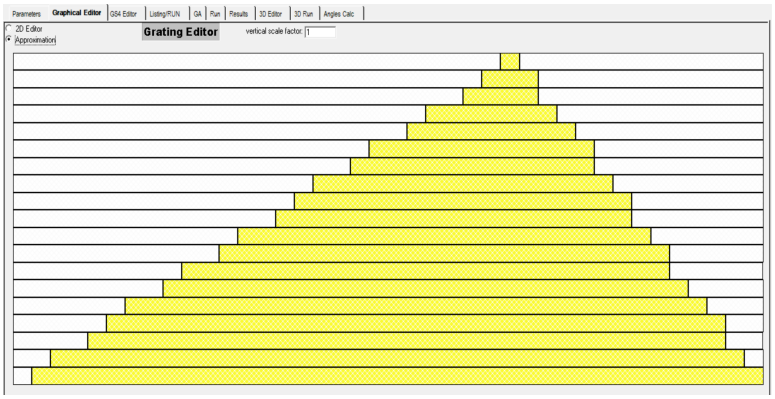

FIGURE 3.10: GSolver approximation of a blazed profile with a stack of rectangular gratings.

The RCW method approximates every real grating as a stack of rectangular gratings, as shown in Fig. 3.10. This simplifies the boundary conditions since the normal and tangential field components line up either along the x- or z-axis. Every layer is treated as a separate grating with its own effect on the incoming and outgoing fields; the total grating effect is propagated to the upper stack using matrix methods.
Note that, when the grating vector is in the plane of incidence, $k_y = 0$ and the coupled-wave equations are reduced to two sets of coupled-wave equations; the first pair—Eqs. (3.24) and (3.27)—gives the solution for the E-mode polarization case, and the second pair—Eqs. (3.25) and (3.26)—gives the solution for H-mode polarization. The coupled-wave Eqs.(3.24)–(3.27) can be written in a matrix form as

$$\begin{bmatrix} \dot{S}_{x,n} \\ \dot{S}_{x,n} \\ \dot{U}_{x,n} \\ \dot{U}_{y,n} \end{bmatrix} = \begin{bmatrix} a & 0 & c & d \\ 0 & f & g & h \\ i & j & k & 0 \\ m & n & 0 & p \end{bmatrix} \cdot \begin{bmatrix} S_{x,n} \\ S_{x,n} \\ U_{x,n} \\ U_{y,n} \end{bmatrix}, \tag{3.30}$$

or in compact form as

$$\dot{\mathbf{V}} = \mathbf{A} \cdot \mathbf{V}. \tag{3.31}$$

The coefficient matrix **A** is the system matrix composed of the 16 submatrices in Eqn. (3.30) that are in turn specified by the 4 sets of coupled-wave equations. Equation (3.35) may be solved using a state-variable method by calculating the eigenvalues and eigenvectors associated with the matrix **A**. The solutions of the coupled-wave equations using the state-variable method may be expressed as

$$S_{x,n}(z) = \sum_{m=-\infty}^{\infty} C_m v_{1,n,m} \exp\{\lambda_m z\}, \tag{3.32}$$

$$S_{y,n}(z) = \sum_{m=-\infty}^{\infty} C_m v_{2,n,m} \exp\{\lambda_m z\}, \tag{3.33}$$

$$U_{x,n}(z) = \sum_{m=-\infty}^{\infty} C_m v_{3,n,m} \exp\{\lambda_m z\}, \tag{3.34}$$

$$U_{y,n}(z) = \sum_{m=-\infty}^{\infty} C_m v_{4,n,m} \exp\{\lambda_m z\}, \tag{3.35}$$

where C_m's are the unknown constants to be determined from boundary conditions, λ_m's are the eigenvalues of the matrix **A**, and $v_{q,n,m}$'s (q = 1..4) are the elements of the eigenvector matrices corresponding to a given value of n (space-harmonic field inside the grating or diffracted order outside the grating). Note that, if N space harmonics are retained in the analysis, the matrix **A** will be 4N X 4N and the vector **V** will be of length 4N. This system of equations produces 4N eigenvalues and 4N values of the unknown constants C_m, and each of the four eigenvector submatrices $v_{q,n,m}$ will be an N X 4N matrix (N values of n and 4N values of m).
The amplitudes of the diffracted fields $\mathbf{R_n}$ and $\mathbf{T_n}$ (together with C_m) are calculated by matching the tangential electric and magnetic fields at the two boundaries. At $z = 0$:

$$u_x \delta_{n,0} + R_{x,n} = S_{x,n}(0), \tag{3.36}$$

$$u_y \delta_{n,0} + R_{y,n} = S_{y,n}(0), \tag{3.37}$$

$$\delta_{n,0}(k_y u_z + k_1 \cos\alpha u_y) + k_y R_{z,n} - k_{z,1,n} R_{y,n} = -kU_{x,n}(0), \tag{3.38}$$

$$\delta_{n,0}(-k_1 \cos\alpha u_x - k_{x,0} u_z) + k_{z,1,n} R_{x,n} - k_{x,n} R_{z,n} = -kU_{y,n}(0). \tag{3.39}$$

On the other side, at $z = d$:

$$T_{x,n} = S_{x,n}(d) \exp\{inK_z d\}, \tag{3.40}$$

$$T_{y,n} = S_{y,n}(d) \exp\{inK_z d\}, \tag{3.41}$$

$$k_y T_{z,n} - K_{z,3,n} T_{y,n} = -kU_{x,n}(d) \exp\{inK_z d\}, \tag{3.42}$$

$$k_{z,3,n} T_{x,n} - K_{x,n} T_{z,n} = -kU_{y,n}(d) \exp\{inK_z d\}. \tag{3.43}$$

The last two conditions are given by $\mathbf{k_{1,n}} \cdot \mathbf{R_n} = 0$ and $\mathbf{k_{3,n}} \cdot \mathbf{T_n} = 0$, therefore we have

$$k_{x,n}R_{x,n} + k_y R_{y,n} + k_{z,1,n}R_{z,n} = 0, \tag{3.44}$$

$$k_{x,n}T_{x,n} + k_y T_{y,n} + k_{z,3,n}T_{z,n} = 0. \tag{3.45}$$

The system of simultaneous linear equations given by Eqns. (3.36)–(3.45) may be solved for $\mathbf{R_n}$ and $\mathbf{T_n}$ by using specific techniques such as Gauss elimination.
The number of equations is exactly equal to the number of unknowns. For example, if N waves (values of n) are retained in the analysis, there will be 4N values of C_m and 3N components of each of $\mathbf{R_n}$ and $\mathbf{T_n}$. Thus the total number of unknowns is 10N, which is exactly the number of equations given by Eqns. (3.36)–(3.45). The computational time and storage requirements is reduced appreciably by eliminating $\mathbf{R_n}$ and $\mathbf{T_n}$ from Eqns. (3.36)–(3.43) by solving for the C_m's and then calculating $\mathbf{R_n}$ and $\mathbf{T_n}$.

The amount of light we get out of the grating (in the useful order), compared to how much light went in is quantified by grating efficiency. This depends on how much energy is absorbed in the grating itself, and how the remaining energy is distributed between orders. For electromagnetic plane waves, the complex Poynting vector represents the energy flux (or energy per unit area) carried by the wave:

$$\mathbf{P} = \frac{\mathbf{E} \times \mathbf{H}^*}{2}. \tag{3.46}$$

This gives the instantaneous energy flux, which oscillates in time with the wave. The time-averaged Poynting vector gives the average flux delivered over a full period of the wave. For harmonic waves, this is equal to the real part of $\mathbf{P}$.
Energy is conserved between incidence, reflection, transmission, and absorption over a constant grating area. Therefore, we define the grating diffraction efficiency (DE) formally as the ratio of the total time-averaged Poynting flux through a surface parallel to the mean grating plane (x–y plane) of the outgoing diffracted order relative to the incident wave.
This is equal to

$$DE_{1,n} = \mathrm{Re}\left\{\frac{k_{z,1,n}}{k_1 \cos\alpha}\right\}\left|\mathbf{R_n}^2\right|, \tag{3.47}$$

for reflected orders and

$$DE_{3,n} = \mathrm{Re}\left\{\frac{k_{z,3,n}}{k_1 \cos\alpha}\right\}\left|\mathbf{T_n}^2\right|, \tag{3.48}$$

for transmitted ones.
Power conservation requires that for lossless phase gratings the sum of the efficiencies for all the propagating waves be unity. That is

$$\sum_{n=-\infty}^{\infty} (DE_{1,n} + DE_{3,n}) = 1. \tag{3.49}$$

Thus it sums to unity for any number of space harmonics retained, independently of whether the corresponding fields outside the grating are propagating or evanescent. Any significant deviation in the sum would indicate the presence of round-off errors in the numerical calculations.
In summary, the algorithm used to solve the efficiency problem proceeds as follows:

- The coefficient matrix **A** is constructed;
- The eigenvalues and eigenvectors are calculated;
- The system of linear Eqns. (3.36)–(3.45) or a modified version of these, is constructed and solved for the $\mathbf{R_n}$'s, since we study only reflection with gold coated gratings;
- The diffraction efficiencies are calculated using Eqns. (3.47) and (3.48).

3.5 AFM analysis and simulation pattern derivation

The groove profile of each grating central area has been characterized using the non-contact AFM mode.
We observed that the pattern of the grooves is not constant along the direction orthogonal to the incidence plane, therefore we derived an average cross-section profile [52, 53]. Each average profile was made-up of a sufficient number of grooves, i.e. between 4 and 6, with the aim of defining an average single-groove pattern. The adopted x resolution for the scans was between 4.8 and 7.3 nm, while the z-resolution was 1.4 Å. The images were leveled to subtract the background slope, which is an artifact of the machine.
A typical AFM clipped image recorded with 4.8 nm pixels resolution is shown in Fig. 3.11(a), where the vertical scale has been expanded to reveal the shape of the groove surface. As represented in Fig. 3.11(b), the exact groove density has been obtained from the power spectral density (PSD) of the average cross-section profile.

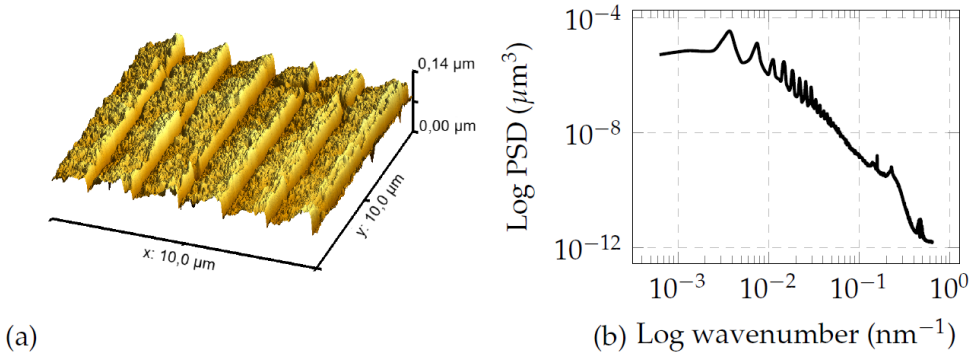

FIGURE 3.11: AFM analysis of the 600 gr/mm grating. a) 10 μm x 10 μm AFM topography of the grating; b) PSD as a function of the wavenumber. The fundamental spatial frequency is located at 0.58 μm^{-1}, which corresponds to a period of 1.72 μm.

From the average single-groove pattern, with a linear least squares fitting routine the blaze and anti-blaze angles of a triangular groove pattern has been derived, as shown in Fig. 3.12. This model has been used for the efficiency simulations performed with GSolver.

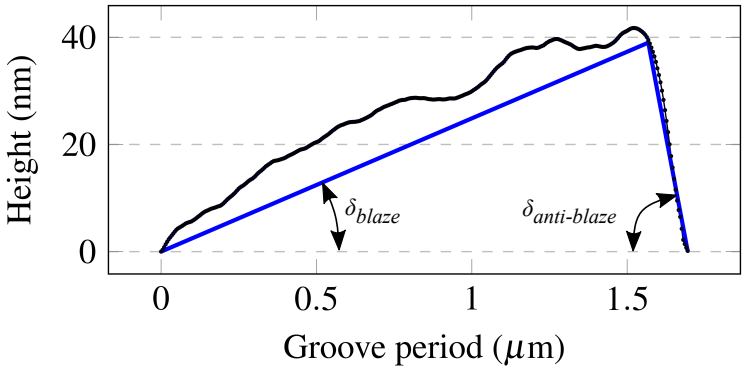

FIGURE 3.12: Average single-groove profile (black-dotted) and derived triangular pattern (blue-solid) of the 600 gr/mm grating. Here δ_{blaze} = 1.42° and $\delta_{anti-blaze}$ = 17° are, respectively the blaze and anti-blaze angles.

3.6 Simulation results with the AFM derived groove profiles

For CDM, simulation results demonstrated that the efficiency, in general, is fairly insensitive to the anti-blaze angle, while it is highly sensitive to a blaze angle variation. In fact, as represented in Figs. 3.13 and 3.14, the efficiency peaks for the brown curves are shifted to a lower incidence angle α compared to the theoretical prediction α_{me}.

From the PSD in Fig. 3.11(b) we noticed that most of the microroughness is concentrated at low spatial frequencies, which are comparable with the grating period, therefore we subtracted the triangular form to the cross-section averaged profiles, in order to find the residual grating roughness. This result amounts to a mirror roughness profile underlying the perfectly periodic grating.

The chosen approach to include the roughness as a scaling factor in the efficiency is based on modelling the grating roughness by substituting the equivalent fold mirror, such that the mirror is used at the same subtended angle k as the grating, and the simulated efficiency results are scaled by the ratio of the gold mirror reflectivity with and without roughness. Results obtained for the 600 gr/mm grating at two different energies of 62 eV and 177 eV with an AFM derived roughness of 6.47 nm rms are reported in Figs. 3.13 and 3.14.

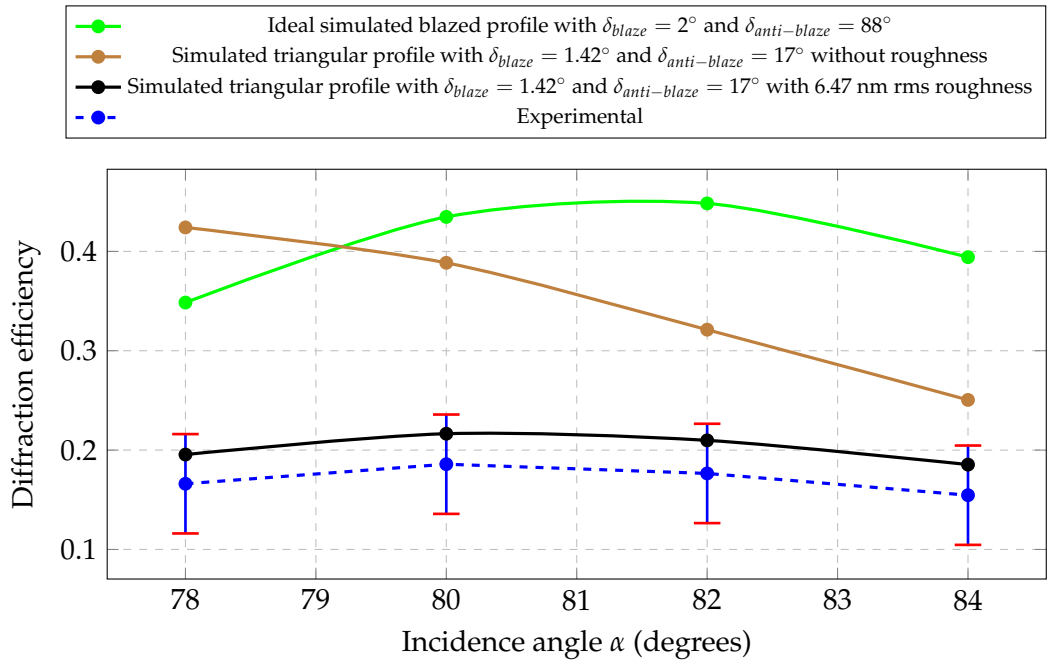

FIGURE 3.13: CDM 600 gr/mm grating 1^{st} order efficiency, 62 eV photon energy, at different α near $\alpha_{me} = 82.1°$.

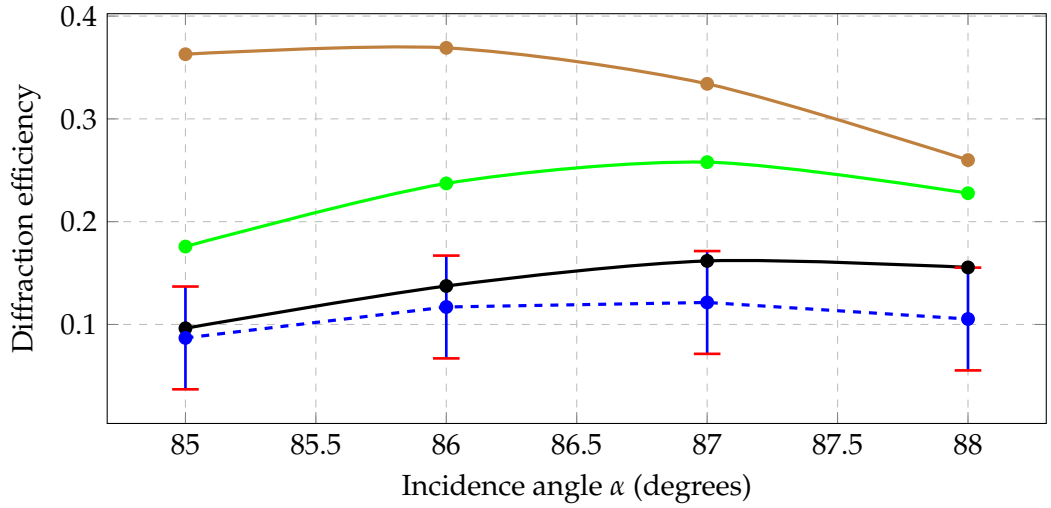

FIGURE 3.14: CDM 600 gr/mm grating 1^{st} order efficiency, 177 eV photon energy, at different α near $\alpha_{me} = 88.5°$.

The treatment of the roughness is a very important part of the analysis of soft X-rays specular reflectivity [54]. Usually this is done by the introduction of a roughness factor Q in the Fresnel reflection coefficient r_s. For low spatial frequencies of the roughness spectrum ($< 1\mu m^{-1}$), the Fresnel reflection coefficient is multiplied by the Debye-Waller factor

$$Q = e^{-2\sigma k_z^2}, \tag{3.50}$$

where σ represents the roughness rms and k_z is the vertical component of the refracted wave vector

$$k_z = kn\cos\alpha_r = \frac{2\pi}{\lambda}\left(n^2 - \sin\alpha_i^2\right)^{1/2}. \tag{3.51}$$

Here we make use of the Snell law $\sin\alpha_r = \sin\alpha_i/n$ to express the refraction angle α_r. In Tab. 3.2 all the AFM derived parameters are reported, which have been used for the simulations of the two CDM gratings, including the calculated low-frequency rms roughness. The residual difference between the experimental and simulation-AFM curves are due to high-frequency roughness effects, dust, scratches, pinholes, reflections out of the incidence plane and other manufacturing errors. We can notice in black curves of Figs. 3.13 and 3.14 that roughness plays an important role in the efficiency decrease.

180 gr/mm	**Blaze angle** (deg.)	**Anti-blaze angle** (deg.)	**Height** (nm)	**Period** (μm)	**Roughness rms** (nm)
Ideal	0.77	89.23	74.5	5.55	-
AFM measurement	0.48	4.76	44	5.72	7.9

600 gr/mm	**Blaze angle** (deg.)	**Anti-blaze angle** (deg.)	**Height** (nm)	**Period** (μm)	**Roughness rms** (nm)
Ideal	2	88	58.1	1.67	-
AFM measurement	1.42	17	39	1.69	6.47

TABLE 3.2: Comparison between ideal and AFM-measured parameters for the CDM gratings.

In the OPM, four variables are responsible of variations of the efficiency curves: the blaze and anti-blaze angles, the surface roughness and the misalignment of the grating pitch, i.e. an unwanted rotation around the axis perpendicular to the grating surface z, as represented in Fig. 3.2. The AFM analysis, reveals small increments from the ideal blaze angles, which contribute to a decrease of the simulated efficiency at higher altitude angles γ; on the other hand a significant anti-blaze angle reduction was measured, which would be responsible of an efficiency drop at lower altitude angles. The OPM configuration compensates partially the last effect through the grating conical rotation. The combination of pitch misalignment with the change of the μ angle during the grating scan made difficult the determination of the resulting χ angle. Therefore we decide to perform simulations at the $\chi = 90°$ condition (which gives the highest efficiency), i.e. we adopt $\mu = 0$ and $\nu \neq \mu$ derived from the OPM grating equation. Furthermore we considered an ideal saw-tooth profile with the AFM-measured blaze angle as shown in Figs. 3.15 and 3.16. The last choice is justified by the fact that the grating rotation in the azimuth angle make less effective the anti-blaze angle reduction.

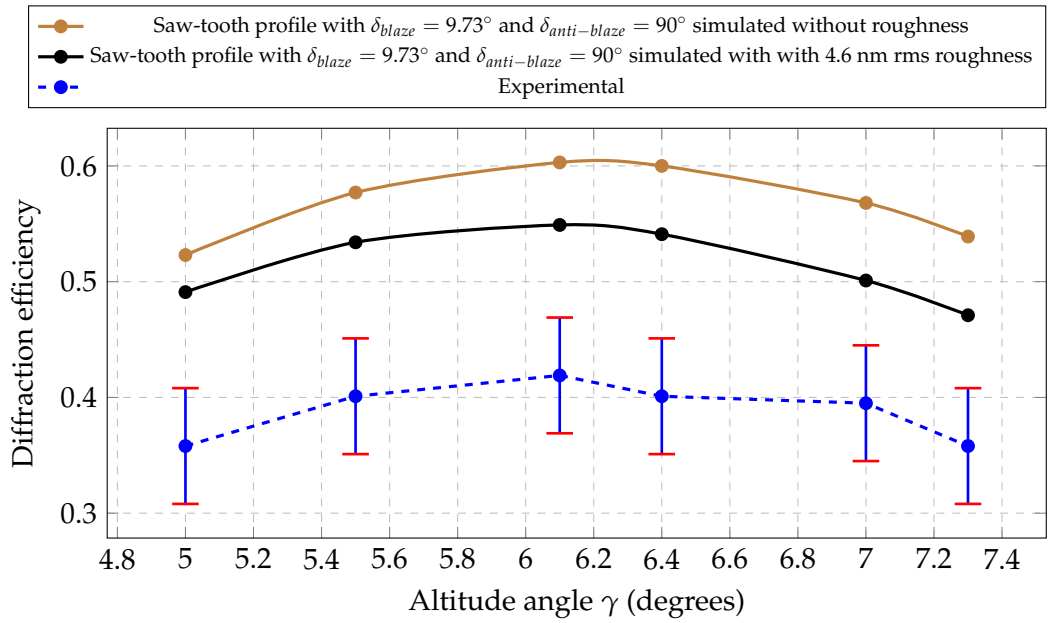

FIGURE 3.15: OPM 1800 gr/mm grating 1^{st} order efficiency, 62 eV photon energy, at different γ near $\gamma_{me} = 6.40°$.

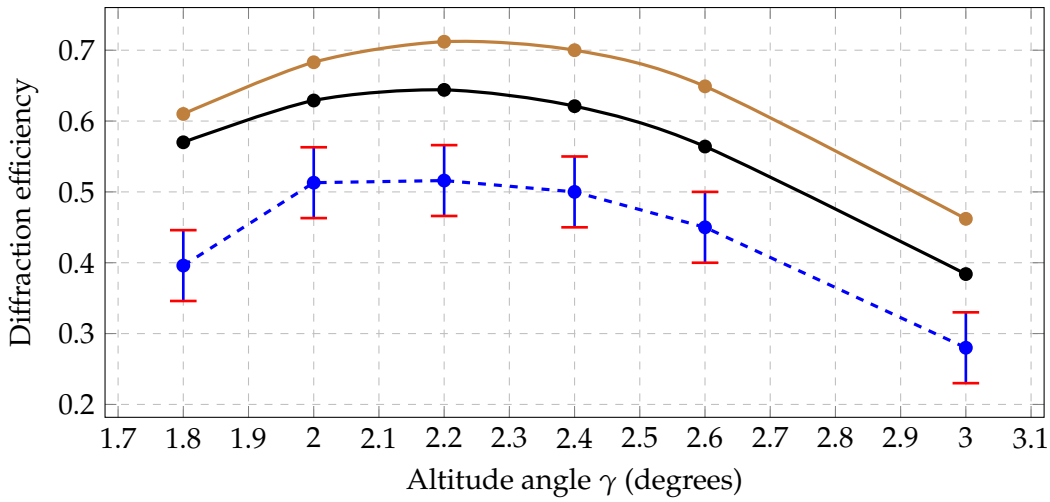

FIGURE 3.16: OPM 1800 gr/mm grating 1^{st} order efficiency, 177 eV photon energy, at different α near $\alpha_{me} = 2.22°$.

The efficiency decrease given by the low-frequency roughness in the direction parallel to the grating grooves, even if lower than CDM, is not negligible, especially for the grating with lower groove density. In Tab. 3.3 the AFM-measured parameters for the two OPM gratings are listed.

1800 gr/mm	**Blaze angle** (deg.)	**Anti-blaze angle** (deg.)	**Height** (nm)	**Period** (μm)	**Roughness rms** (nm)
Ideal	9.3	80.7	87.4	0.55	-
AFM measurement	9.73	16	61.1	0.57	4.6

2400 gr/mm	**Blaze angle** (deg.)	**Anti-blaze angle** (deg.)	**Height** (nm)	**Period** (μm)	**Roughness rms** (nm)
Ideal	10.36	79.64	73.6	0.42	-
AFM measurement	10.68	14.7	46	0.42	1.4

TABLE 3.3: Comparison between ideal and AFM-measured parameters for the OPM gratings.

3.6.1 OPM misalignment of the grating pitch

The grating pitch is a relevant variable to be considered in the efficiency decrease. OPM grating mountings have to be designed in order to precisely adjust this feature to obtain the maximum photon flux. The misalignment of the grating pitch χ, as represented in Figs. 3.17 and 3.18, has the effect of both decrease and shift the ideal efficiency maximum located at γ_{me}, especially for rotations towards the valley of the groove. Unfortunately, our measurement experimental setup does not allow the control of this feature, therefore we could not take into account this effect in our simulations.

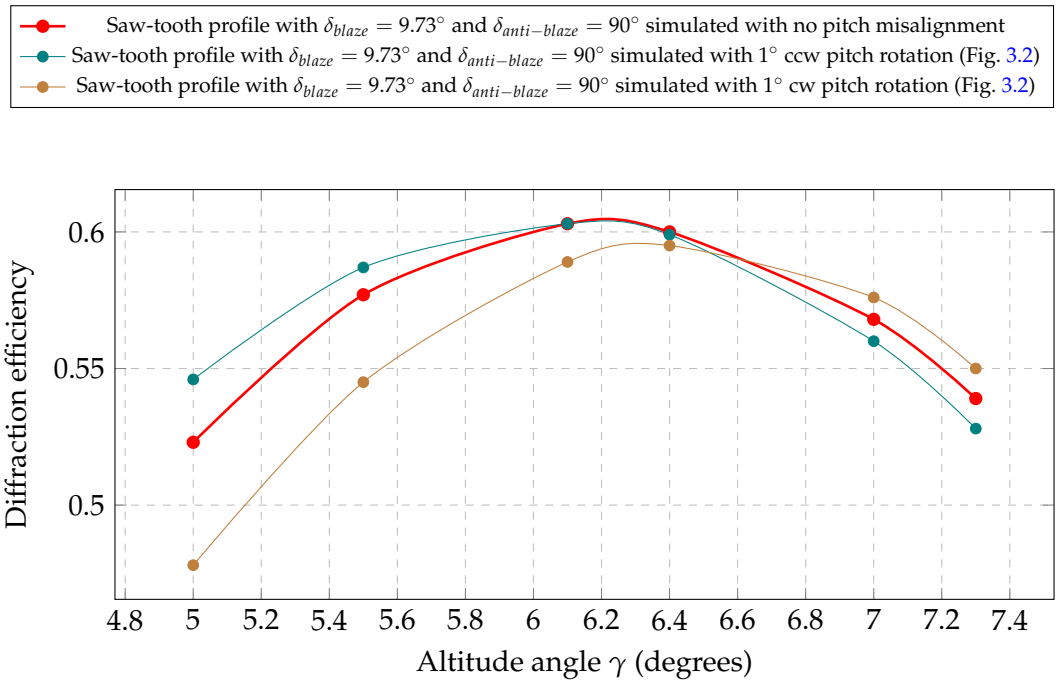

FIGURE 3.17: OPM 1800 gr/mm grating 1^{st} order efficiency, 62 eV photon energy at different γ near γ_{me} = 6.40°.

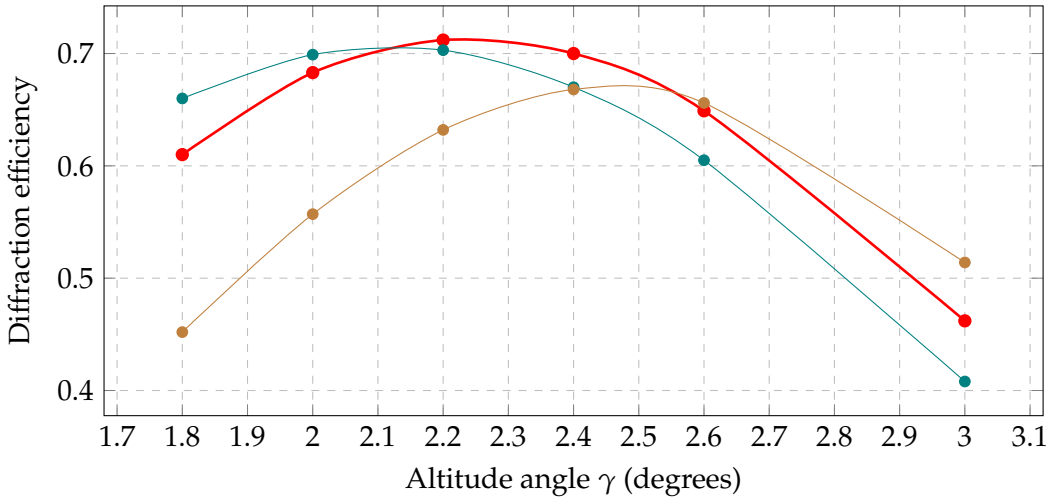

FIGURE 3.18: OPM 1800 gr/mm grating 1^{st} order efficiency, 177 eV photon energy at different γ near $\gamma_{me} = 2.22°$.

3.6.2 Comparison between CDM and OPM diffraction efficiencies

In Figs. 3.19 and 3.20 are reported the first order experimental efficiency peak values for the discrete 41–310 eV photon energy range of interest.

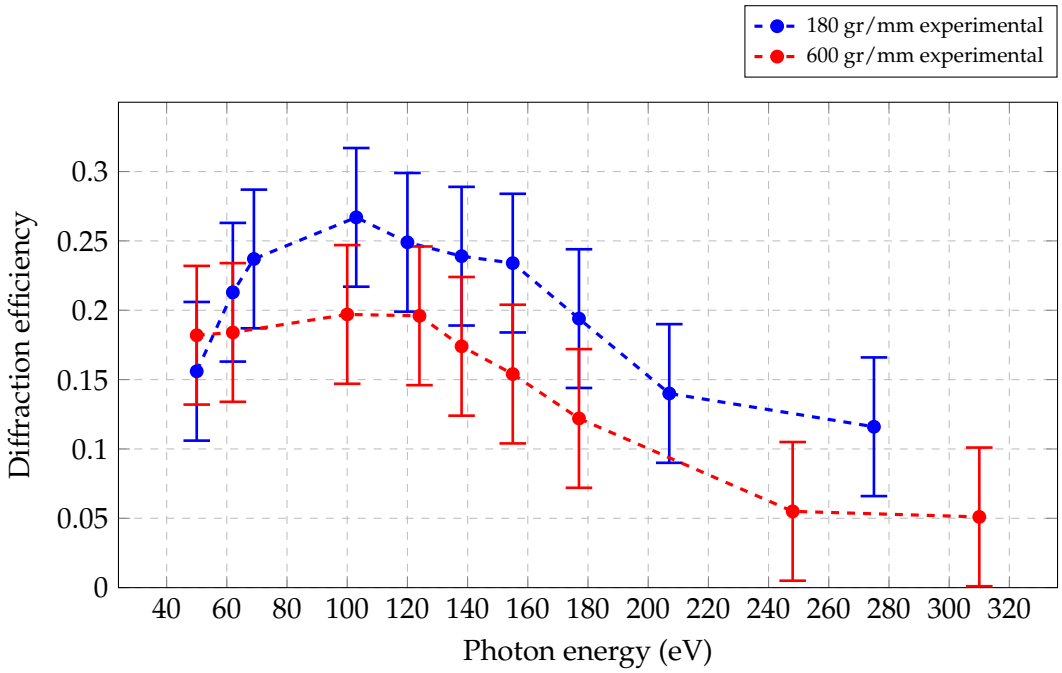

FIGURE 3.19: CDM 180 and 600 gr/mm grating 1^{st} order peak efficiencies for the entire spectral range.

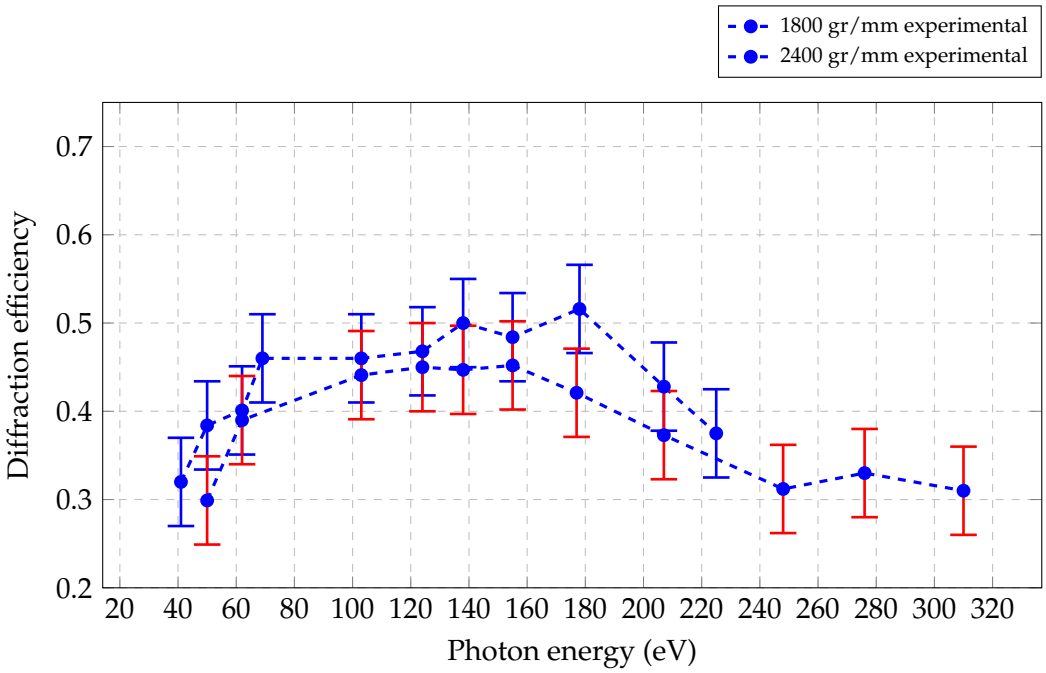

FIGURE 3.20: OPM 1800 and 2400 gr/mm grating 1^{st} order peak efficiencies for the entire spectral range.

The efficiency maximum angles are obtained by interpolating the experimental curves. Efficiencies as high as 45% at 100 eV and 35% at 310 eV have been measured for OPM grating configurations for soft X-rays.

Despite of the use of low-price commercially-available replica gratings, we demonstrate the capability of maintaining high efficiency up to the Carbon K-edge (≈284 eV). Compared to the CDM configuration, the efficiency of a single grating is increased by a factor of almost 2 at 100 eV and almost 7 at 310 eV. The results confirm the benefit of employing the OPM configuration not only for the realization of single-grating monochromators, but even for double-grating time-delay compensated ones even in the soft X-ray region.

Chapter 4

Setup of a time-delay compensated monochromator for the spectral selection of attosecond XUV pulses

4.1 Introduction

I have contributed at the project aimed at the setup of a beamline section of the Extreme Light Infrastructure – Attosecond Light Pulse Source, ELI-ALPS facility (Szeged-Hungary) commissioned to CNR-IFN. The ELI-ALPS is one of the three large European laser pillars built under the umbrella of the Extreme Light Infrastructure project for development of world leading European ultra-bright lasers and their interactions with matter. The beamline is based on a HHG source and has been designed for ultrafast IR-pump–XUV-probe experiments on surfaces and solid state targets.
The target is to improve the beamline initial design in order to add a double stage monochromator for the selection of a single generated harmonic or a sub-band of it. This is required because the major part of the experiments executed with the end station (e.g., photoelectron spectroscopy) may need an XUV pulse with a narrow spectrum, with a pulse duration from few to tens of femtoseconds. The monochromator should provide to the facility users the possibility of selecting discrete photon energies in a range between 17–90 eV. The monochromator has to be designed to avoid further temporal stretching of the pulses by i.e. pulse-front tilt, and preserve an XUV pulse duration allowed by the inherent properties of the generation process. The geometry of the modified beamline has only an additional vacuum chamber and a slit block with respect to the initial setup without the monochromator.

As will be explained, the monochromator introduces three different operational phases on the beamline which can be selected based on the experimental requirements of the users:

- **Time-compensated monochromator operation (OP1)** to obtain monochromatic pulses with few femtoseconds duration;

- **Broadband operation (OP2)**, in which pulses remain polychromatic, obtaining pulses with minimum duration and maximum intensity determined by the source features (no modification with respect to the initial configuration of the beamline);
- **High-flux monochromator operation (OP3)** to obtain monochromatic pulses with few hundreds of femtoseconds duration but higher flux with respect to the first operational phase.

Section 4.2 gives a first overview of the adopted solution consisting in a double stage time-delay compensated (TDC) monochromator. Then, a detailed layout description of the ELI-ALPS beamline with the monochromator insertion is reported in Sections 4.3 and 4.4. Section 4.5 explains the Labview software implementation, including all the tasks necessary for the future alignment and calibration of the instrument. Section 4.6 reports the chosen parameters of the monochromator, in order to obtain the requested bandwidth and temporal performances. Finally, Section 4.7 illustrates the test experiments that will be performed by using the XUV monochromator.

4.2 Off-plane mount time-delay compensated monocromator

The monochromator uses a couple of consecutive gratings in the OPM (or "conical") configuration already described in Sect. 3.2. It has been shown both theoretically and experimentally in Sect. 3.6.2 and [55], that the efficiency of the off-plane mounting is much higher than that of the classical configuration, therefore the off-plane mounting is a suitable candidate to achieve the highest possible throughput from a grating monochromator.

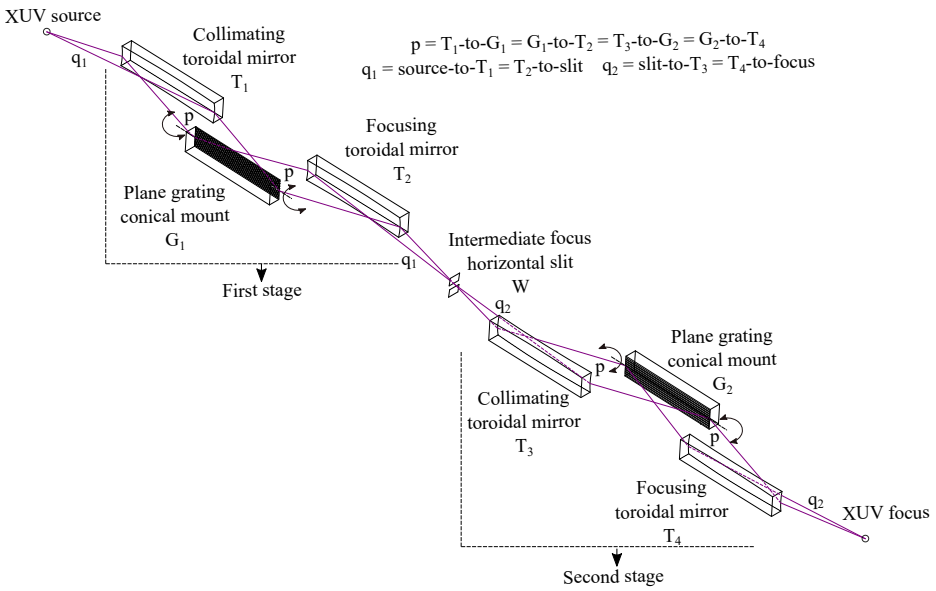

FIGURE 4.1: Double-grating TDC monochromator in the OPM.

As explained in Sect. 3.1, a single grating introduces necessarily a pulse front-tilt because of the diffraction, therefore the temporal resolution gets worse after the monochromator. A monochromator with negligible front-tilt requires the use of at least two gratings in the compensated configuration. The design of a time-delay compensated (TDC) monochromator in the OPM geometry requires four toroidal mirrors and two plane gratings, as shown in Fig. 4.1. The first mirror collimates the light coming from the entrance source point, the first grating is operated in parallel light, then the second mirror focuses the diffracted light on the exit slit. After the slit, the light is monochromatized and the pulse-front is tilted.
The second section compensates for the pulse-front tilt, therefore the number of grooves illuminated on G_2 has to be the same as G_1. Since typically the gratings are equal and are operating at the same altitude angle γ, this condition is fulfilled with a symmetrical configuration, i.e. $q_1 = q_2$. Conversely, as we will see, we adopted an asymmetrical geometry to fit exactly the existing focusing geometry. Furthermore, in order to minimize the aberrations, each of the two sections is operating with unity magnification, i.e., the input arm of the collimator is equal to the output arm of the successive focusing element (see Appx. A.1.1). The wavelength scanning is provided by rotating the gratings around an axis passing through the grating center and parallel to the groove direction. The last mirror of the second section is also required to focus the radiation at the output.

4.3 The ELI-ALPS high repetition primary source

The target of the in gas higher harmonic generation (GHHG) high repetition (HR) CONDENSED beamline is the generation and application of attosecond pulses at a repetition rate of 100 kHz using HHG in noble gases. The beamline will act as a secondary source and will be driven by the HR laser (the primary source), providing users with attosecond and auxiliary pulses to perform ultrafast IR-pump–XUV-probe experiments.

Parameters	**HR 1**	**HR 2**
Center wavelength λ_c	1030 nm	1030 nm
Repetition rate	100 kHz	100 kHz
Average power	$>$ 100 W	$>$ 500 W
Pulse energy	$>$ 1 mJ	$>$ 5 mJ
Pulse duration (@λ_c)	$<$ 6.2 fs (1.85 cycles)	$<$ 6.2 fs (1.85 cycles)
CEP stability	$<$ 100 mrad (rms)	$<$ 100 mrad (rms)

TABLE 4.1: Parameters of the HR laser system in phase 1 and phase 2.

The HR laser is an optical fiber based system that operates at 100 kHz repetition rate and delivers pulses with sub-2cycle duration at 1 mJ (phase 1) and 5 mJ (phase 2) pulse energy. The HR laser system relies on optical fiber technology [56, 57] featuring coherent combination [58] with subsequent non-linear compression [59], which enables highly efficient amplification and compression to TW pulse peak powers centered around 1030 nm. High quality, coherent attosecond pulses in the XUV spectral region has been obtained with this system. The parameters of the HR laser in phase 1 and phase 2 are listed in Tab. 4.1.
Figure 4.2 shows a schematic of the HR laser system. The laser system is based upon a carrier-envelope phase (CEP) stable fiber oscillator emitting pulses around 1030 nm with 20 nm bandwidth. The repetition rate of the 80 MHz oscillator is reduced to 100 kHz using two acousto-optic modulators. Two subsequent preamplifier systems, consisting of large pitch fibers (LPFs, 65 μm core diameter, 1 m length), enhance the average power to 20 W. The front end is completed by a double-pass grating stretcher, providing enough dispersion to stretch the pulses to 1.5 ns.

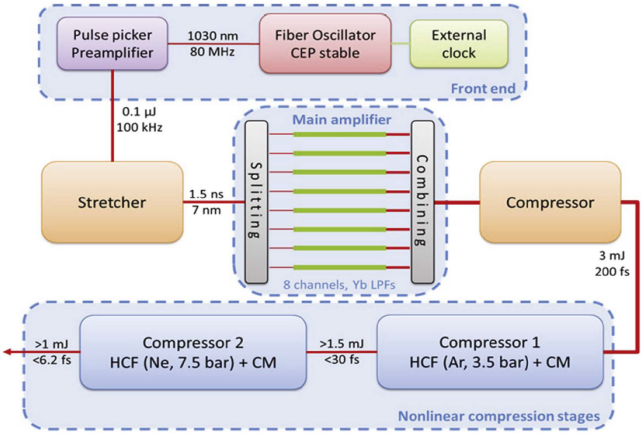

FIGURE 4.2: Scheme of the HR laser system with three major subsystems: the front end, the main amplifier and the non-linear compression stages. (CM: chirped mirror stage).

The output pulse from the front end is divided to eight channels, and each channel is coupled to a separate LPF amplifier pumped by high-power continuous wave diodes, each with a pump power of 80 W. Each single fiber channel (Fig. 4.2) is pumped at 100 W, which results in amplifying the nanosecond pulses up to 60 W average power per channel without any spectral and spatial distortion. The amplified pulses are then coherently combined with 90 % efficiency, resulting in a 100 kHz repetition rate pulse train of 440 W average power.

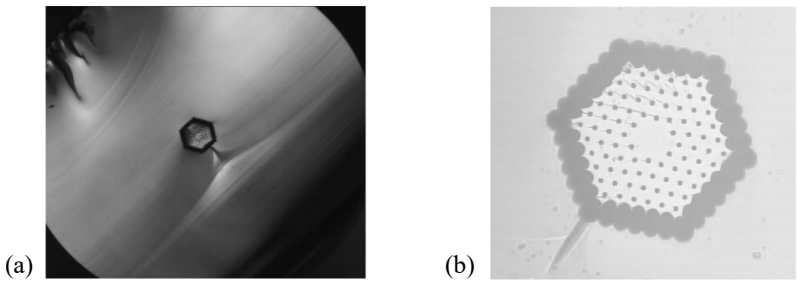

FIGURE 4.3: (a) Microscope image of a Yb rod-type photonic crystal fiber and (b) close up of the inner cladding and core regions.

A compressor is used after the main amplifier, to shorten the pulses close to the transform limit (≈200 fs). The pulses are compressed below two optical cycles in a two-stage non-linear hollow core fiber (HCF) compressors, each filled with a noble gas in order to achieve a high nonlinearity of the propagation medium. The residual dispersion is compensated by chirped mirrors after each HCF stage.

4.4 The secondary source GHHG beamline

The HR laser drives the GHHG HR CONDENSED and GAS beamlines (the second one is based on experiments on gas targets and is not discussed here). The CONDENSED beamline will feature a double XUV-IR interaction region geometry: the first one dedicated to the temporal characterization of the XUV radiation, and the second one dedicated to the experimental users-defined interchangable end stations.

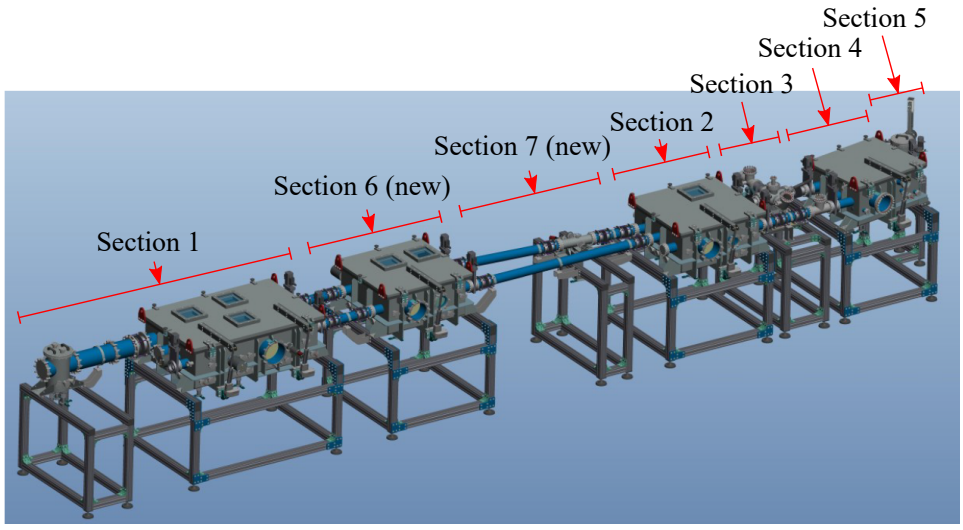

FIGURE 4.4: General 3D layout of the GHHG Condensed beamline.

The beamline is designed to probe different samples or targets, in particular non-transparent samples, such as solid targets. Figure 4.4 shows the designed layout, consisting of seven main Sections or vacuum chambers (CHs):

- **Section 1**: IR splitting, IR gating and XUV generation;

- **Section 2**: second stage of the TDC monochromator, first XUV-IR recombination chamber and focusing section for the first target area;
- **Section 3**: time-of-flight (TOF) electron spectrometer placed in the first target area to measure the XUV pulse duration;
- **Section 4**: second XUV-IR recombination chamber and focusing section for the second target area: the user end station;
- **Section 5**: intensity monitor and XUV photon spectrometer;
- **Section 6**: first stage of the TDC monochromator;
- **Section 7**: intermediate slit for the wavelength selection between the two stages of the monochromator.

All Sections before the user end station are placed on the same optical table , in order to improve the mechanical stability of the beamline. The vacuum chambers are mounted on external frames, and are mechanically isolated from the optical table to improve the isolation of the attosecond section from the external vibrations. Since test samples are intended to be solid, the diagnostic section cannot be inserted after the second target area but is on a different optical path, and is operated alternatively to the users experiments.

4.4.1 IR splitting, polarization gating and XUV HHs generation

Here a fundamental IR beam with a central wavelength of 1030 nm and a full width at half maximum (FWHM) diameter of 12 mm is assumed. This IR beam is initially split by a holey mirror at 45° into the annular external part, used to generate attosecond pulses (beam 1), and the central part that is later recombined with the XUV (beam 2). The diameter of the central hole that gives a 70 : 30 ratio is 8.5 mm, although mirrors with holes of various diameters will be tested to optimize the IR/XUV ratio for pump-probe experiments. A central hole with 8 mm diameter is assumed. Immediately after the splitting mirror, two systems can independently stop the two IR beams.
The beam stop is a mirror at 45° with a broadband coating centered at 1030 nm, deflecting the laser beam 90° toward a high average power beam dump mounted externally to the vacuum chamber.
Beam 1 initially propagates through two wedges, used to compensate for dispersion and to change the relative phase between beam 1 and beam 2, and then passes through two ultra-broadband birefringent plates, used to realize the polarization gating for the generation of isolated attosecond pulses [60]. As shown in Figs. 4.5 and 4.6, the beam is finally focused by a spherical mirror at almost normal incidence, located in either the auxiliary chamber CH-01.03 for phase 1 or in CH-01.04 for phase 2. Assuming a laser peak intensity in the gas cell of the order of 10^{15} W·cm^{-2} results in estimated focal lengths of 2.2 m (phase 1) and 5.7 m (phase 2).

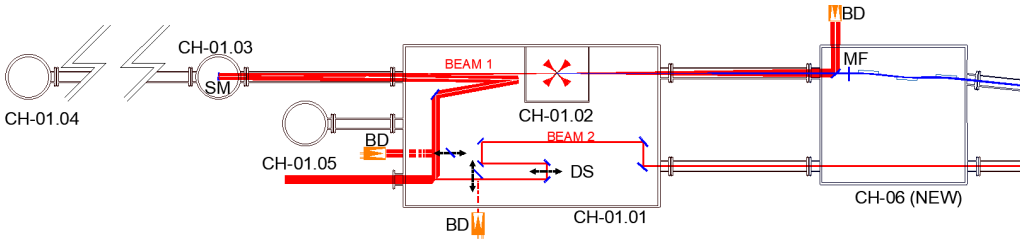

FIGURE 4.5: Optical layout of the Section 1 CONDENSED beamline, with IR (red) and XUV (blue) paths, phase 1. Legend: BD, beam dump; DS, delay stage; SM, spherical mirror; MF, metallic filter.

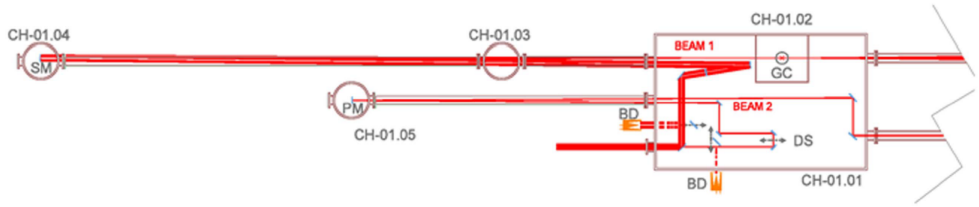

FIGURE 4.6: Optical layout of the Section 1 CONDENSED beamline in phase 2. With respect to phase 1, two accessory chambers are added to the layout to host: respectively, a long-focal spherical mirror to generate XUV attosecond pulses, and a folding mirror to realize a longer path for beam 2. The subsequent sections of the beamlines are unchanged. Legend: Fig. 4.5 + PM, plane mirror; GC, gas cell.

Attosecond pulses are generated in a gas cell with a length ranging from 2 to 10 mm, containing noble gases. After the generation, the XUV beam propagates collinearly with the annular IR beam, although with a smaller divergence [61].

Beam 2 propagates through two wedges that compensate for dispersion and change the relative phase. The beam is delayed by a motorized optical delay stage and finally propagates toward the recombination chamber. If the optical path of the beam 2 has to be increased to match the XUV and IR path lengths, it can be sent to a folding plane mirror placed in the auxiliary chamber CH-01.05. The use of this chamber is required only for phase 2.

4.4.2 Double stage monochromator

Upon entering Section 6, the annular IR beam, that generates XUV pulses is blocked by a suitable beam stop: a deflecting holey mirror placed in vacuum, a window and an external beam dump placed in air. This mirror has a central hole to allow the XUV to further propagate; this hole's diameter is the same as that of the hole of the beam splitting mirror in Section 1 projected by the spherical focusing mirror. For phase 1, the hole is assumed to be 6 mm and small enough to stop the annular IR portion and possible IR diffracted light.

An XUV full divergence of 2.7 mrad is acceptable in this case. Section 6 hosts: (i) the optical elements of the first stage of the monochromator: collimating toroidal mirror,

plane gratings, focusing toroidal mirror and (ii) the first stage for the broadband operation: focusing toroidal mirror.
After the annular IR beam block, the operations performed are:

1) in operational phases OP1 and OP3, as shown in Fig. 4.7(a), the XUV beam is collimated by the first toroidal mirror (TM-06.01) of the monochromator, then it is spectrally dispersed in the vertical direction by one of the five plane gratings (G-06.01 in Fig. 4.7(c)) used in the off-plane geometry, finally it is focused by the second toroidal mirror (TM-06.02) of the monochromator on the plane of the exit slit in Section 7;

2) in operational phase OP2, the XUV beam is filtered by a metallic thin foil (typically aluminum), demanded to block any residual IR light that is diffracted through the holey mirror of the beam dump and to introduce the required Group-Delay-Dispersion (GDD) to correct for the XUV pulse chirp. After filtering, as shown in Fig. 4.7(b), the mirrors of the monochromator (TM-06.01 and TM-06.02) are extracted from the optical path. A focusing toroidal mirror (TM-06.05) collinear with the gratings is inserted in the optical path at grazing incidence (3°) in 1:1 configuration, with 2.25 m entrance arm and 2.25 m exit arm. Due to this mirror, the XUV beam is focused on the plane of the exit slit in Section 7.

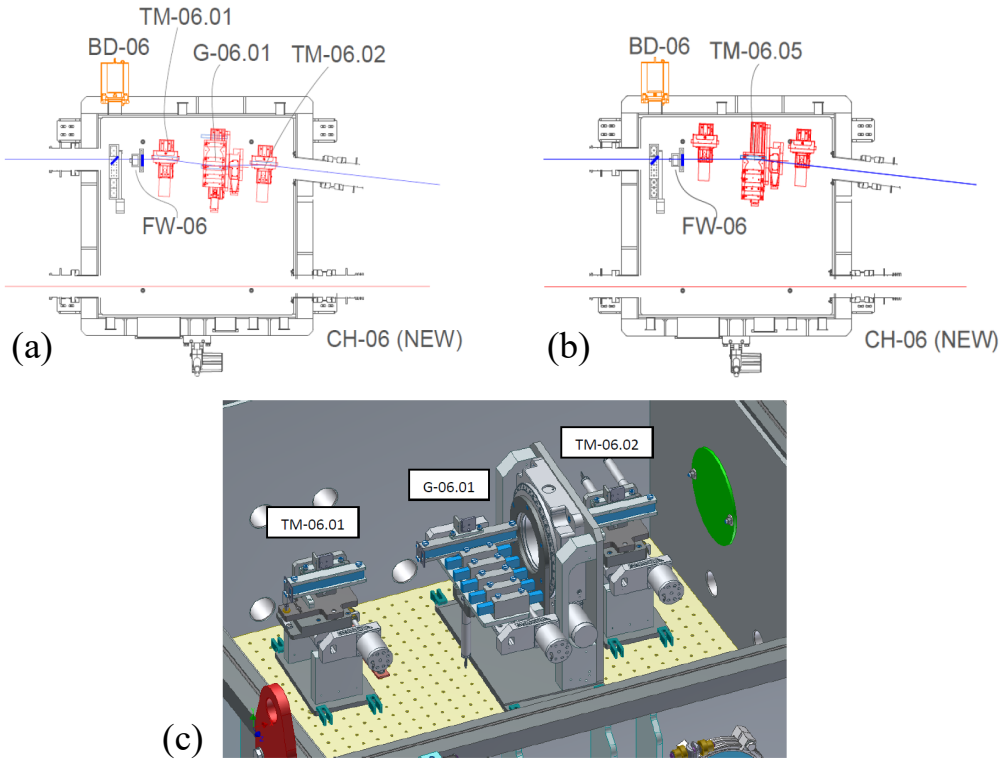

FIGURE 4.7: Optical layout of System 6: (a) TDC or high-flux monochromator operations, OP1 and OP3; (b) Broadband operation, OP2; (c) 3D internal layout with optical mounts. Legend: TM, toroidal mirror; G, grating; FW, filter wheel.

On a filter wheel placed before the first mirror TM-06.01, in addition to the mentioned filter, there is a free slot to be used during the alignment procedure and a closed slot to be used to block the XUV beam without acting on the IR generating laser.

Beam 2 has a cross section slightly larger than 8 mm (including the contribution of the diffraction), and is transmitted through the Section 6 toward the Section 2, where it is recombined with the XUV.

Section 7 hosts the slit block shown in Fig. 4.8(b). It has two operative conditions associated with the previous operations 1) and 2):

3) in operational phases OP1 and OP3, the slit is required to perform the spectral selection of a single harmonic (or a sub-band of it). Typical slit apertures are in the range 100–200 μm;

4) in operational phase OP2, the slit is completely open (typically, up to few millimiters), to let the whole XUV beam propagate.

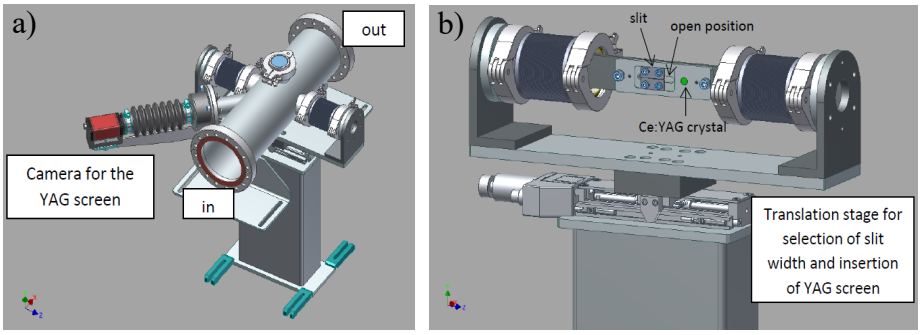

FIGURE 4.8: General 3D layout of System 7: a) external view; b) internal view, showing the slit realized by two blades mounted with a V-shaped profile, the open position and the Ce:YAG crystal slot.

The slit aperture is controlled by acting on a motorized stage. The slit block will host also a Ce:YAG crystal that can automatically be inserted by acting on the same motorized stage that is used to control the slit aperture. The Ce:YAG crystal is used to visualize the XUV spot and check the co-propagation of the XUV beam in the three operational phases.

Section 2 contains the second stage of the monochromator and the recombination IR-XUV optics.
There are two possible operations:

5) in operational phases OP1 and OP3, the XUV beam after being mochromatized on the slit plane, passes through Section 2. In OP1 case, the pulse-front tilt correction is required, followed by a focusing on the TOF focal plane in Section 3. Therefore, analogously to point 1), a collimating toroidal mirror TM-06.03, one between five plane gratings (G-06.02 in Fig. 4.9(c)) and a focusing toroidal mirror TM-06.04 are used as shown in Fig. 4.9(a). Instead, in OP3 case, only the

focusing in the TOF focal plane is needed, performed by the TM-06.06 toroidal mirror in 1:1 configuration collinear with the gratings shown in Fig. 4.8(b);

6) In operational phase OP2, the XUV broadband beam enters Section 2 after the first focusing toroidal mirror. Here, analogously to OP3, it is focused in the TOF focal plane by the toroidal mirror TM-06.06.

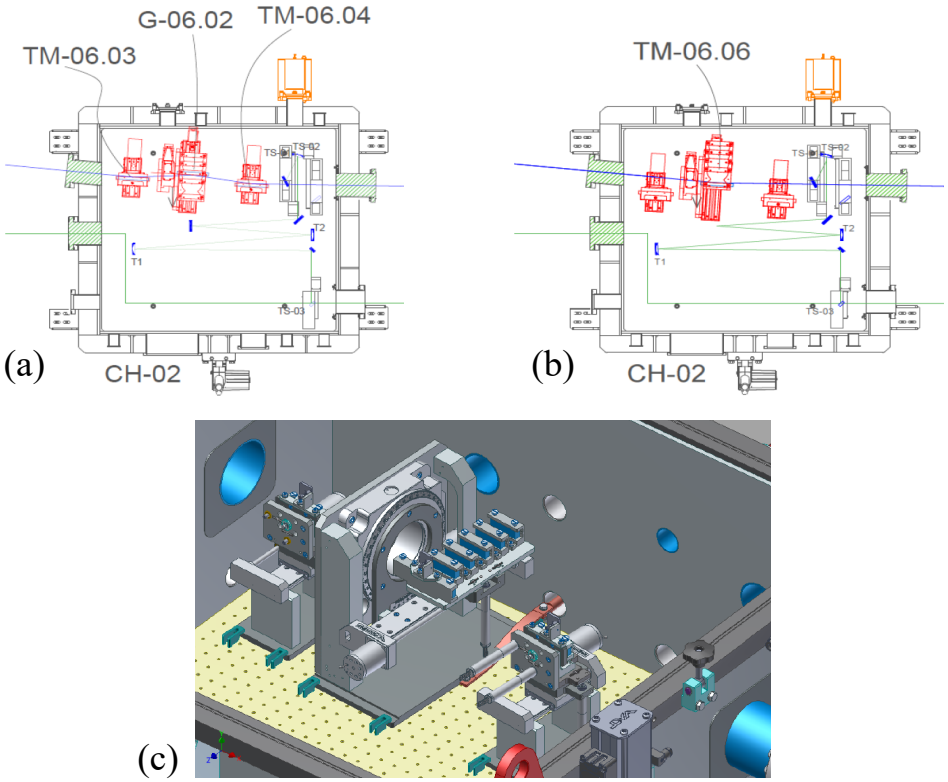

FIGURE 4.9: Optical layout of System 2: (a) TDC monochromator operation, OP1; (b) Broadband and high-flux monochromator operations, OP2 and OP3; (c) 3D internal layout with optical mounts. Legend: Fig. 4.7 + T1-T2-TS, concave telescope and spherical mirrors.

The three operational phases are reported in Fig. 4.10.

Beam 2, entering in Section 2, has a cross-section comparable to the XUV, and therefore has to be increased in size, through a telescope arrangement realized with two concave mirrors, before the XUV-IR recombination.
Finally, the beam is focused by a spherical mirror and recombined with the XUV by a holey mirror at 45° that reflects only an annular portion of the IR and lets the XUV propagate through its central hole. The position and the focus of the spherical mirror have to be chosen in order to ensure that the IR and XUV focus overlaps with the necessary intensity to permit electron streaking in the TOF.

Two optical configurations of the XUV-IR recombination may be realized in order to provide the final XUV and IR beams to the users:

- **Configuration 1**: the XUV and IR beams recombine in Section 2 and then, after the TOF chamber, propagate collinearly to a grazing incidence toroidal mirror hosted in Section 4, which focuses both beams in the second target area;
- **Configuration 2**: the XUV and IR beams can be recombined in either Section 2, in case of measurements with the TOF, or Section 4, for measurements in the second target area. A movable plane mirror accommodated in Section 2 is inserted in the optical path to choose between the two options.

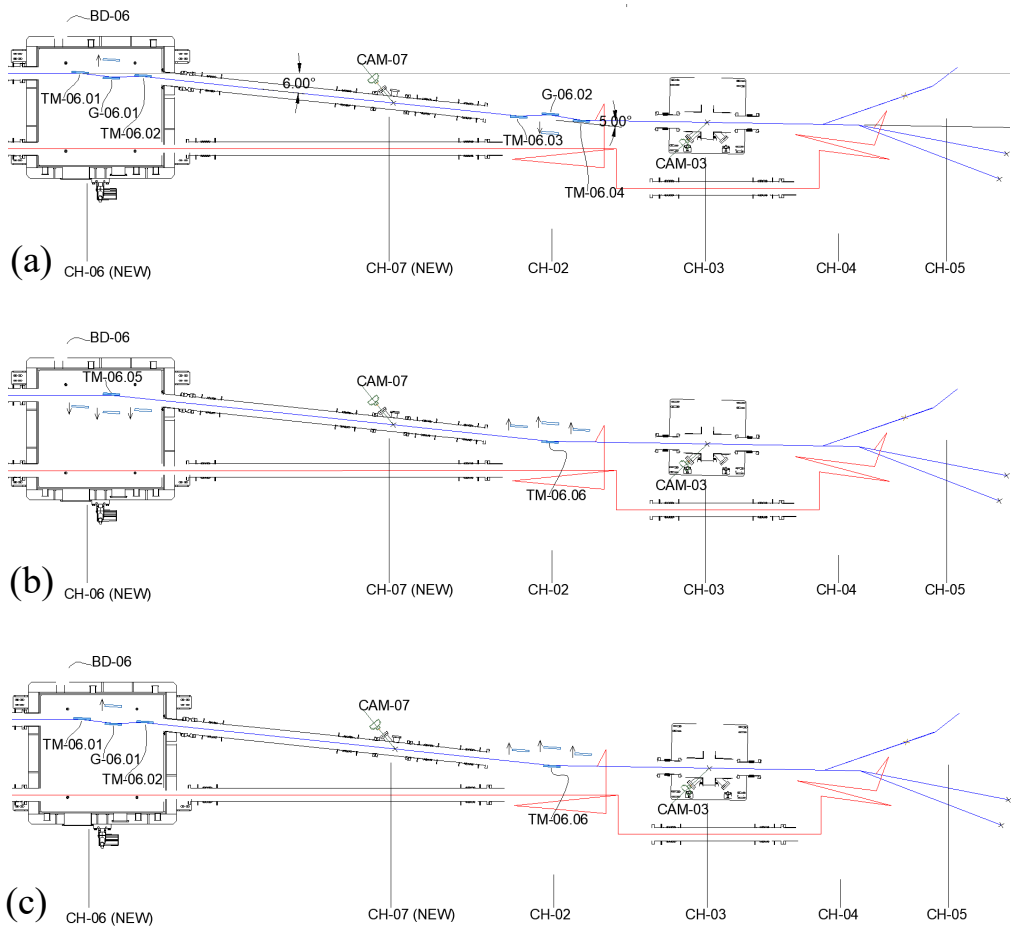

FIGURE 4.10: Schematic of the beamline operation: (a) time-delay compensated monochromator (OP1); (b) broadband operation (OP2); (c) high-flux monochromator (OP3). Here the holey mirror (for IR blocking) and the filter wheel are not shown. Legend: TM, toroidal mirror; G, grating; CAM, camera.

4.4.3 TOF electron spectrometer, user end station and XUV spectrometer

The temporal duration of the attosecond pulses will be measured in the first target area shown in Fig. 4.11(a) by a TOF electron spectrometer [62] applying the FROG-CRAB technique discussed in Sect. 2.3.2 and [63].
In Fig. 4.11(b) the layout of Section 4 is shown.
In configuration 1, both XUV and IR beams are propagating collinearly to Section 4

to a moderate grazing incidence (10°) toroidal mirror in 1:1 configuration, i.e. 1.2-m entrance and exit arms, that focus both beams in the second target area. In 1:1 configuration, the toroidal mirror gives negligible aberrations, as all the terms up to the third order are corrected—in particular, defocusing, coma and astigmatism [64]. The toroidal mirror is assumed to have a 40-nm-gold coating, a standard value for XUV coatings. The average XUV reflectivity is 0.7 in s-polarization and 0.5 in p-polarization.
In case of configuration 2, the IR-XUV recombination occurs either in Section 2 or in Section 4. Inside Section 4, the XUV beam is focused by a toroidal mirror at grazing incidence (5°) in 1:1 configuration, i.e. 1.2-m entrance and exit arms. The mirror is used at a lower grazing angle than configuration 1, i.e. 5° versus 10°, to increase the XUV reflectivity. The average XUV reflectivity is 0.85 in s-polarization and 0.70 in p-polarization. Therefore, both XUV and IR are focused in the second target area, where the user end station can be placed.

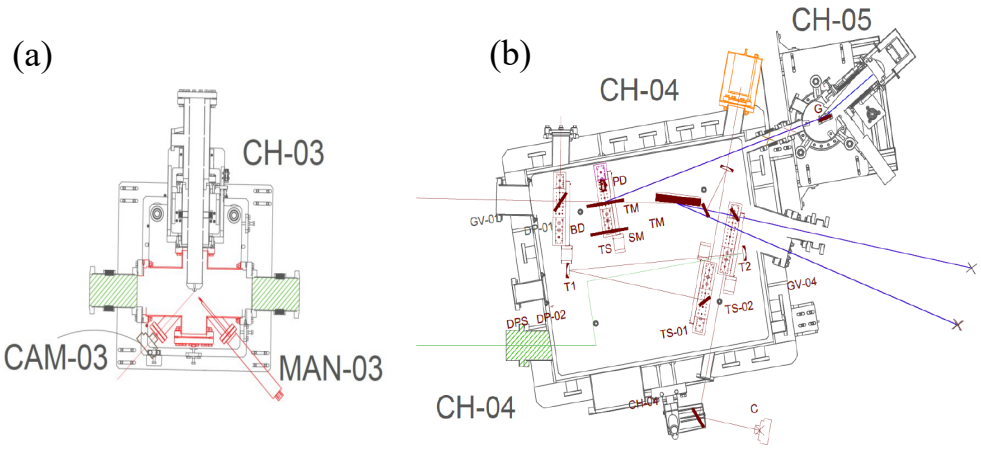

FIGURE 4.11: Layouts of (a) TOF electron spectrometer in Section 3 and (b) second XUV-IR recombination chamber with intensity monitor and XUV photon spectrometer connected to it (Sections 4 and 5). The XUV beam is directed to the two second target areas according to the chosen configuration: either 1 (lower target) or 2 (upper target). Legend: MAN, manual translation stage to insert the Ce:YAG crystal; CAM, camera to look at the crystal surface.

Section 5 is dedicated to spectral and intensity diagnostics of the XUV beam. The XUV absolute intensity is measured by a metallic calibrated photodiode, that is completely blind to any contribution possibly coming from the IR diffused light. The XUV spectrum is measured through a spectrometer equipped with a pre-focusing concave mirror, a flat field variable-line-spaced grating and a microchannel-plate detector with phosphor screen and charge-coupled device (CCD) camera. Two different pre-focusing mirrors can be inserted. The first is a toroidal mirror with its tangential focus on the virtual entrance slit in front of the grating and its sagittal focus on the detector, to obtain a stigmatic spectrum and therefore the best signal-to-noise ratio, even when measuring faint signals.

The alternative is a cylindrical mirror having its tangential focus on the virtual entrance slit in front of the grating, to obtain an astigmatic spectrum that may be useful to measure the divergence of the XUV beam as altered by the XUV-target interaction [65].

4.5 Labview software implementation

In the following, a description of a graphical user interface (GUI) required for controlling the monochromator stages in the three operational phases is presented.

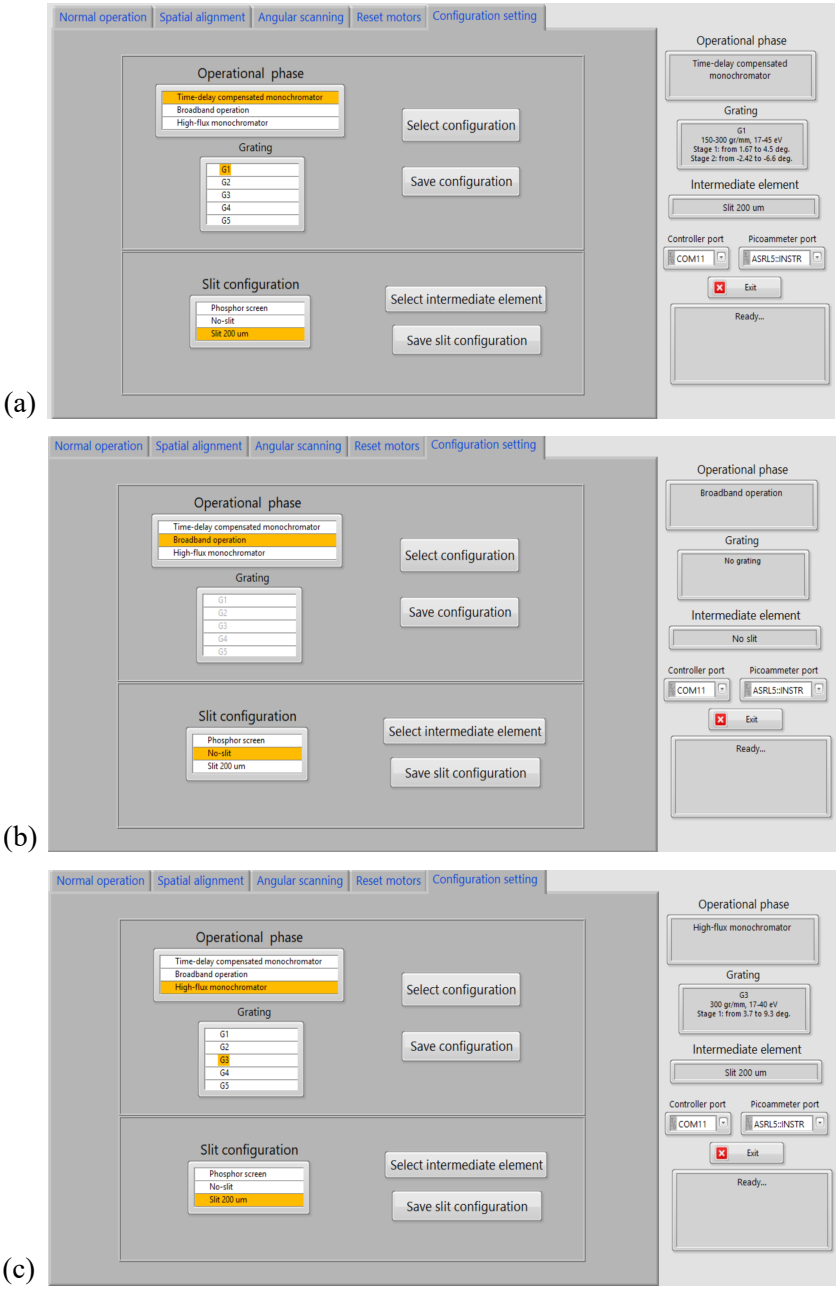

FIGURE 4.12: Window for the selection of the operational phases: (a) OP1, (b) OP2 and (c) OP3.

The software has been developed through the Labview development environment in order to be ready for a first alignment of the monochromator. Once the alignment will be performed, an improvement of the software, and a networked control will be realized, (for example by means of the TANGO toolkit).

4.5.1 Selection of operational modes

A proposed interface for the selection of the operational phases (OP1, OP2, OP3) is shown in Fig. 4.12. The user can select one of the three operational phases. When OP1 or OP3 are selected, the user must select also the pair of gratings that will be inserted. The operations to be performed by the software, once the operational phase has been selected (with reference to Fig. 4.10), are:

1) close the main shutter of the laser;

2) move the optical elements in order to insert the selected configuration

   a) OP1: insert TM-06.01, TM-06.02, TM-06.03, TM-06.04. Insert G-06.01 at a predefined rotation angle far from the zero order. Insert G-06.02 at the zero order. Set the slit aperture to 200 μm.

   b) OP2: insert TM-06.05, TM-06.06. Select the open position in the intermediate focal plane in Section 7.

   c) OP3: insert TM-06.01, TM-06.02, TM-06.06. Insert G-06.01 at a predefined rotation angle far from the zero order. Set the slit aperture to 200 μm.

When the monochromator option is selected, the user can also select the grating pair to be used. When the grating is changed, the operations to be performed are:

i) close the main shutter of the laser;

ii) insert the selected grating.

In addition, the user has the possibility to insert in any operative phase the Ce:YAG screen in the intermediate slit in order to see the XUV spot size.

4.5.2 Normal operation

The commands available to the users depend on the selected operational phase.
The normal operation window is shown in Fig. 4.13. Here the user can insert a calibrated XUV photodiode mounted in Section 4 and control the settings (scale and voltage supply) of the picoammeter that is used to read current from the photodiode. For OP1 and OP3, the user has the possibility to choose a specific wavelength/photon energy within the specified gratings working range. After the "SELECT" button has been pressed, the rotary stage that holds the gratings of Section 6 and 2, start to rotate to a specific angle based on a second order calibration-derived equation. Obviously, the OP2 operation does not allow a photon energy selection, since we want

a polychromatic radiation at the output of the monochromator.
After photon energy selection, the user can adjust finely (with absolute and relative rotation movements) the two mountings that host the gratings in order to have the maximum photon flux at the output from a single HH. To perform the last task a intensity-versus-time plot (given by the photodiode) has been implemented.

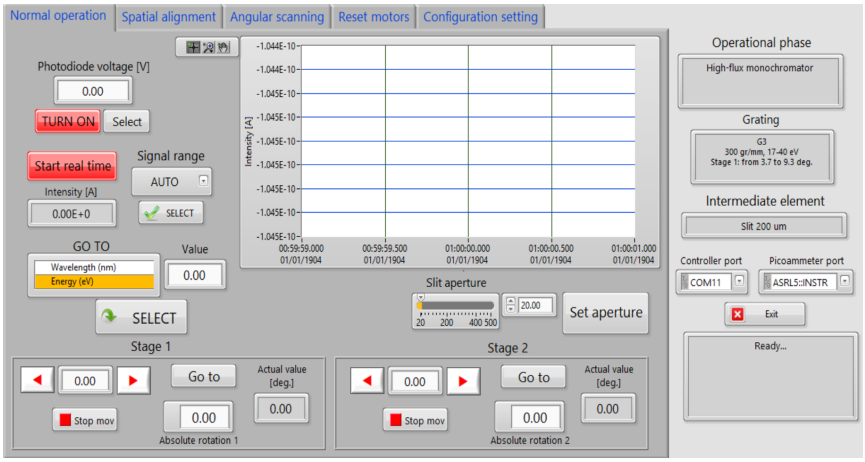

FIGURE 4.13: Normal operation window.

In addition, for OP1 and OP3 the user can select different values (from the initial equal to 200 μm) of the intermediate slit width. The aperture to translation values conversion is based on a linear equation since the two blades of the slit are mounted with a V-shaped profile (see Fig. 4.8(b)).
A a drop-down menu will be implemented to select one of the two cameras:

i) CAM-07 looks at the Ce:YAG crystal in Section 7;

ii) CAM-03 looks at the Ce:YAG crystal in Section 3. When CAM-03 is selected, the user is asked to confirm that the Ce:YAG screen has been manually inserted.

4.5.3 Spatial alignment

The alignment procedure has to be performed in the following steps:

1) alignment of the focusing toroidal mirrors for the broadband configuration;

2) alignment of the first stage of the monochromator;

3) alignment of the second stage of the monochromator;

4) alignment of the second focusing stage for the high-flux monochromator.

The alignment could be periodically checked by ELI-ALPS expert operators. In the following, only the first two steps are described. The other two are similar.

Alignment of the focusing toroidal mirrors for the broadband operation

When OP2 is selected, the operator can finely tune the position of the focus by acting on the mirrors TM-06.05 and TM-06.06. The operator can select one of the following options:

1.1) alignment with the IR at zero order;

1.2) alignment with the XUV;

Alignment with the IR at zero order is enabled only when the laser is operated in the low-power mode. After removing the beam dump in Section 6, the software allows to perform the following operations:

1.1.1) close the slit in the range 50–100 μm

1.1.2) select CAM-03 and insert the Ce:YAG crystal on Section 3;

1.1.3) act on the pitch of TM-06.05 to move the beam in the vertical direction in order to be centered on the slit;

1.1.4) select CAM-07 and insert the Ce:YAG crystal on Section 7;

1.1.5) mark the position of the focus in CAM-07;

1.1.6) act on the roll of TM-06.05 to improve the beam quality on the focus of CAM-07;

1.1.7) if the focus has moved from its original position as marked in point 1.1.5), act on translation and pitch of TM-06.05 to recover the position;

1.1.8) select CAM-03 and remove the Ce:YAG crystal in Section 7;

1.1.9) mark the position of the focus in CAM-03;

1.1.10) act on the roll of TM-06.06 to improve the beam quality on the focus of CAM-03;

1.1.11) if the focus has moved from its original position as marked in step 9, act on translation and pitch of TM-06.06 to recover the position;

1.1.12 save the settings of the motorized actuators by clicking on the "Save configuration" button in the Configuration setting window (Fig. 4.12).

Alignment with the XUV operation is enabled only when the laser is operated in the full power mode. After inserting the metallic filter in Section 6, the alignment procedure is the same as 1.1), steps 1–12. The spatial alignment window for the broadband operation is shown in Fig. 4.14.

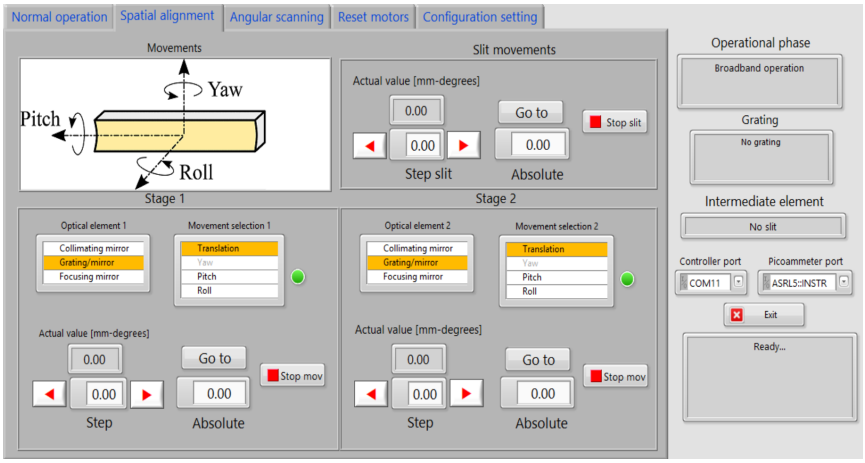

FIGURE 4.14: The spatial alignment window for the broaband operation phase.

For each of the two focusing mirror stages, the operator can select one between four available motorized actuators: translation, angular pitch, angular roll, angular yaw. Translation, pitch and roll are available for gratings. Only translation is available for the collimating mirrors. The named angular rotations are defined as usual for mirror mountings, anyway they are illustrated by the software in Fig. 4.14 to avoid any misunderstanding.

Alignment of the first stage of the monochromator

The XUV beam from the first stage of the monochromator has to be co-aligned with the XUV beam in the broadband configuration. The operator can select one of the following options:

2.1) alignment at zero order with IR;

2.2) alignment at zero order with XUV;

2.3) alignment at diffracted order with XUV.

Alignment at zero order with IR operation is enabled only when the laser is operated in the low-power mode. After removing the beam dump in Section 6, the software allows to perform the following operations:

2.1.1) select CAM-07 and insert the Ce:YAG crystal on Section 7;

2.1.2) insert the first grating pair and the two collimating mirrors (TM-06.01 and TM-06.03). The grating is automatically inserted at the zero order;

2.1.3) act on the roll of TM-06.02 to improve the beam quality on the focus of CAM-07;

2.1.4) if the focus has moved from its original position as marked in point 1.1.5), act on pitch and yaw of TM-06.02 to recover the position;

2.1.5) save the settings of the motorized actuators by clicking on the "Save configuration" button in the configuration window (see Fig. 4.12);

2.1.6) insert the second grating pair;

2.1.7) if the focus is moved with respect to the reference position, act on pitch and translation of the grating stage G-06.01 to recover the position;

2.1.8) save the settings of the motorized actuators by clicking on the "Save configuration" button;

2.1.9) repeat points 6-8 for each of the remaining grating pairs (see Fig. 4.15).

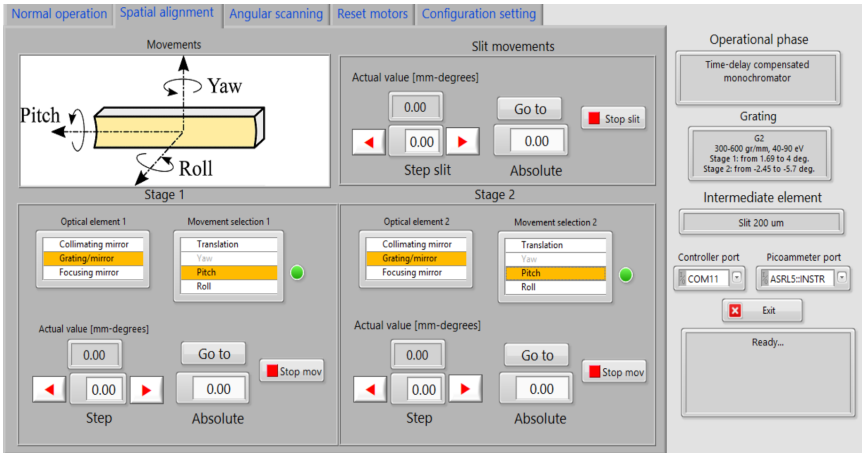

FIGURE 4.15: Spatial alignment of the second grating in the first monochromator stage.

Alignment at zero order with XUV operation is enabled only when the laser is operated in the full power mode. After inserting the metallic filter in Section 6, the alignment procedure is the same as point 2.1).

Alignment at XUV diffracted beam operation is enabled only when the laser is operated in the full-power mode. This operation is assumed to be done immediately after point 2.2). After removing the metallic filter in Section 6, the alignment procedure is the following:

2.3.1 select CAM-07 and insert the Ce:YAG crystal on Section 7;

2.3.2 insert the first grating pair of the first stage of the monochromator. The grating is automatically inserted at an angle far from the zero order;

2.3.3 rotate the grating to the angle corresponding to one selected wavelength, that is typically one of the high-order harmonics;

2.3.4 if the focus is moved with respect to the reference position, act on the roll of the grating stage G-06.01 to restore the position;

2.3.5 save the settings of the motorized actuators by clicking on the Save configuration button;

2.3.6 repeat points 2–5 for each of the remaining grating pairs.

4.5.4 Angular scanning

The calibration equation for the normal operation window will be given in form of a second-order polynomial law expressed as angle-versus-wavelength:

$$\mu = A + B \cdot \lambda + C \cdot \lambda^2, \tag{4.1}$$

where μ is the grating azimuth angle. For each grating, the calibration coefficients A, B, C are derived from the angular scanning window shown in Fig. 4.16.

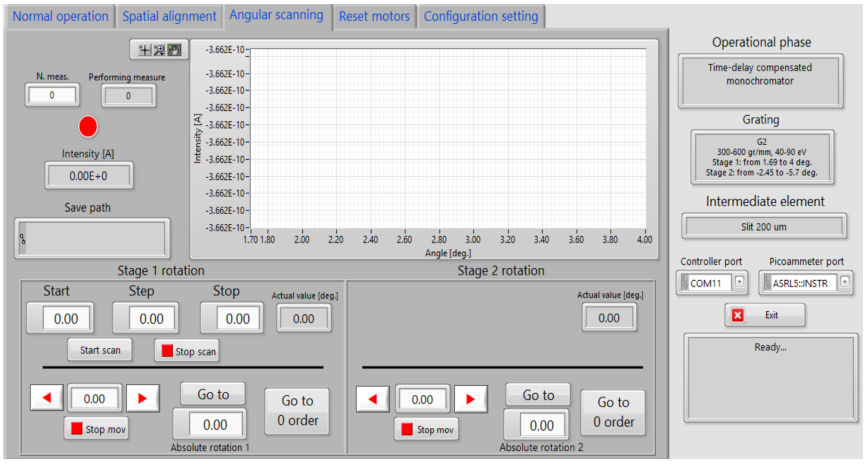

FIGURE 4.16: Angular scanning window for the calibration of the monochromator.

The scan operation is performed on the first stage of the monochromator. The operator selects the initial and final angles and the scanning steps. The program controls that the values inserted are within the available range of the grating. Once the Start scan button has been pressed, the program automatically performs the following steps:

1) the grating of the second stage G-06.02 is moved to the zero order;

2) the calibrated photodiode mounted in Section 4 is inserted in the optical path;

3) the scan starts and the signals read from the photodiode as a function of the grating azimuth rotation are plotted on the screen;

4) the acquired spectra can be saved.

The operator can finely adjust the grating rotation with absolute and relative movements to see some HHs features (lower commands in Fig. 4.16).

Once data have been acquired, they can be analysed through Matlab or similar programs. Known spectral features have to be identified, in order to link wavelengths to angles. A polynomial fit will be performed and the calibration coefficients can be saved in the configuration file.
An example of HHs 15-37 obtained theoretical angular values from Eqn. (3.4) with grating pair 1 (17-45 eV photon energy range) in OP1 phase are shown in Fig. 4.17. A linear fit has been used for the calibration, therefore the coefficient C is equal to zero.

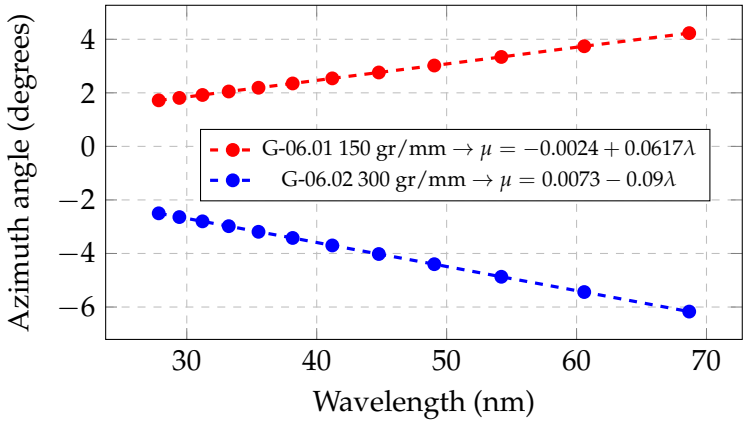

FIGURE 4.17: Theoretical angular values obtained for the first (red points) and second (blue points) monochromator stages with the first grating pair and OP1 operation). The performed interpolation is linear.

4.5.5 Reset motors

In case of some failure (e.g., software crash, electric failure etc.) a reset procedure has been implemented, as shown in Fig. 4.18.

FIGURE 4.18: Reset motors window. Every stage movement is monitored in the two tables on the right.

The reset procedure moves all the motorized actuators except the two rotary stages to the zero position, set by the limit switches. All the angles are defined with reference to the zero position. Then, all the normal operation can start again, from the selection of the operational phase.

4.6 Monochromator parameters and expected performances

4.6.1 TDC monochomator configuration

As discussed in Sect. 4.2, existing TDC monochromators have two equal sections consisting of two equal grating pairs (in terms of groove density), altitude angles and equal arms. In order to have a more compact layout, it is here proposed to adopt an asymmetrical geometry in which the input/output arms are 2000-mm long for the first section ($q_1 = q$) and 1000-mm long for the second section ($q_2 = q/2$) with different altitude angles of the gratings. Furthermore the toroidal mirror-to-grating distances (p) are chosen equal to 250 mm. Consequently, the groove density of the grating in Section 2 has to be twice that of the grating in Section 6, in order to compensate for the pulse-front tilt. The optical parameters of the monochromator for the OP1 operation are shown in Tab. 4.2. In Fig. 4.19 are shown the distances between the optical elements of each Section.

OP1: TDC monochromator	
MIRRORS	Toroidal gold
TM-06.01 and TM-06.02 (in Section 6)	$q_1 = q = 2000$ mm, $AOI = 86.5°$
TM-06.03 and TM-06.04 (in Section 2)	$q_2 = q/2 = 1000$ mm, $AOI = 86.0°$
Mirror-to-grating distance	$p = 250$ mm
GRATINGS	Plane gold, off-plane geometry
Gratings G-06.01 (in Section 6)	**Gratings G-06.02 (in Section 2)**
Low-energy resolution option	
Altitude $\gamma = 4°$	**Altitude** $\gamma = 5.5°$
G1-A, $\sigma = 150$ gr/mm, 17-45 eV, $\delta = 2.2°$	G2-A, $2\sigma = 300$ gr/mm, $\delta = 3.6°$
G1-B, $\sigma = 300$ gr/mm, 40-90 eV, $\delta = 2.5°$	G2-B, $2\sigma = 600$ gr/mm, $\delta = 4.3°$
High-energy resolution option	
G1-C, $\sigma = 300$ gr/mm, 17-40 eV, $\delta = 6.5°$	G2-C, $2\sigma = 600$ gr/mm, $\delta = 8.6°$
G1-D, $\sigma = 600$ gr/mm, 35-65 eV, $\delta = 7.0°$	G2-D, $2\sigma = 1200$ gr/mm, $\delta = 10.4°$
G1-E, $\sigma = 1200$ gr/mm, 60-90 eV, $\delta = 8.6°$	G2-E, $2\sigma = 2400$ gr/mm, $\delta = 10.4°$

TABLE 4.2: OP1 optical parameters of the monochromator.

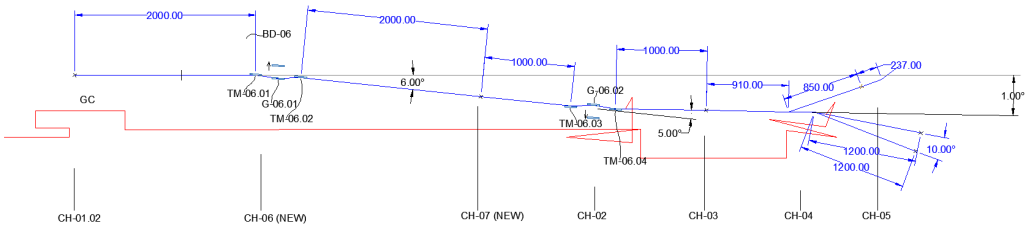

FIGURE 4.19: Overall beamline layout.

This geometry has two main advantages:

i) the arm of the input section is long enough to accommodate the beam dump that is demanded to stop the annular IR generating beam;

ii) the arm of the second section fits exactly the existing focusing geometry, therefore the second stage can be accommodated in Section 2 in place of the currently mounted ellipsoidal mirror.

The monochromator accommodates five gratings, which are required to cover the extended range of tunability (17–90 eV). Since it is assumed to be used with HHs generated by laser pulses centered at $E_0 = 1.2$ eV, the bandwidth transmitted by the slit has to be narrow enough to resolve two adjacent harmonics, that are separated by $2E_0 = 2.4$ eV. Therefore a bandwidth lower than 1 eV FWHM is high enough to separate two adjacent harmonics.

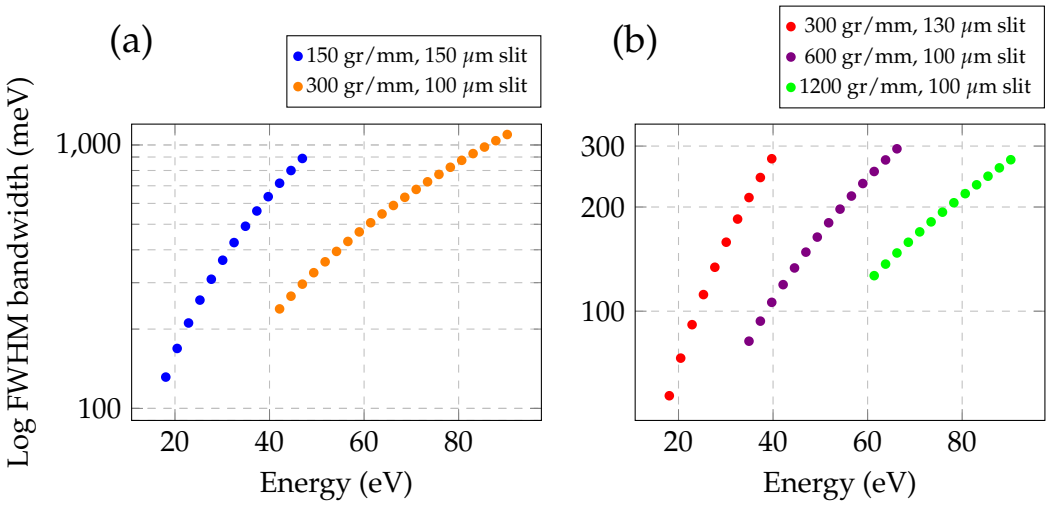

FIGURE 4.20: Simulated FWHM bandwidth response of the TDC monochromator configuration for (a) low resolution and (b) high resolution option.

For application to monochromatization of HHs, the monochromator can be used in two operative conditions: (1) low-resolution or (2) high-resolution option. In the first case, the bandwidth transmitted through the slit is wider than the intrinsic bandwidth of the single harmonic, although lower than the separation between

consecutive harmonics, therefore the monochromator is used as a tunable filter to select one of the harmonics and the output bandwidth is limited by the bandwidth of the harmonic. In the second case, the output bandwidth is narrower than the bandwidth of the single harmonic and the spectral resolution is limited by the instrumental response. Three gratings are used for high resolution (50–300 meV) and two for low resolution (100–1000 meV). The bandwidth performances are presented in Fig. 4.20.

The temporal response is evaluated considering two effects on the ultrafast pulse given by the TDC monochromator. The first effect is the compensation of the pulse-front tilt, that is ideally perfect for a double-grating configuration, although aberrations may give residual distortions of the pulse-front, that are expected to be anyway below 10 fs. The second effect is the group delay (GD) introduced by the two gratings, i.e., different wavelengths within the bandwidth transmitted by the slit travel different paths. Indeed, the pair of gratings can be considered as a XUV pulse shaper. The GD is calculated as the difference in the optical paths within the bandwidth $\Delta\lambda$, as discussed in details in [66]. In case of $\Delta\lambda/\lambda < 10\%$, the GD is linear with the wavelength and results:

$$GD(\lambda) = -(3q - 5p)\frac{\lambda\sigma^2}{c\cos^2\mu}\Delta\lambda \approx -(3q - 5p)\frac{\lambda\sigma^2}{c}\Delta\lambda, \tag{4.2}$$

where the distances q and p are defined in Tab. 4.2 and the term $\cos^2\mu \approx 1$ can be neglected, since the azimuth μ is typically lower than 15°.

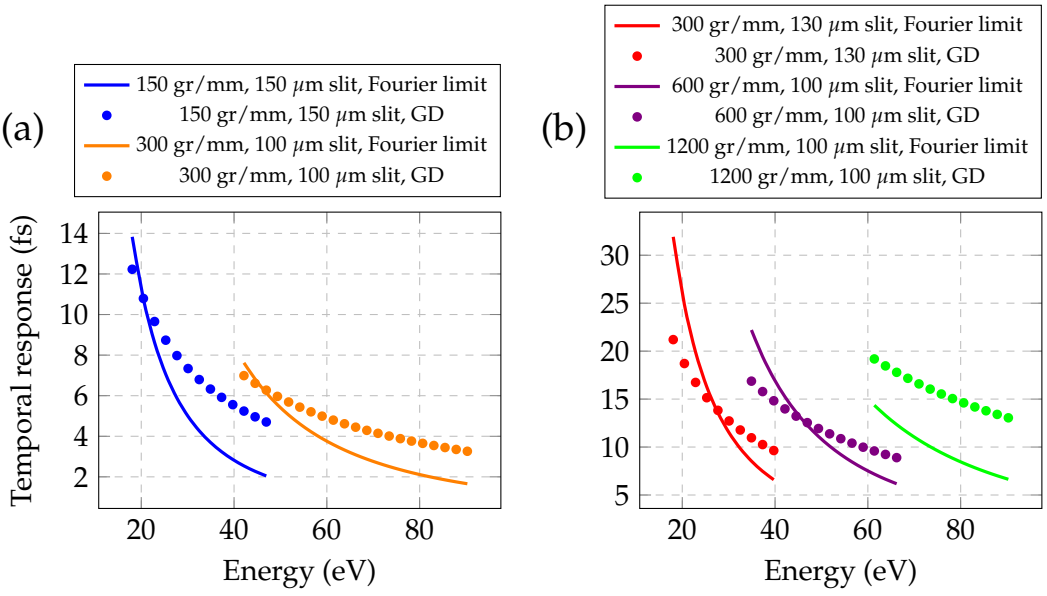

FIGURE 4.21: Simulated Fourier limit and GD of the TDC monochromator configuration for (a) low resolution and (b) high resolution option.

The actual temporal response is limited by the Fourier limit for the selected bandwidth $\Delta\tau_F$ in Eqn. (3.2) and by the GD. In the low- or high-energy resolution mode, it has been simulated to be respectively below 15 fs and below 30 fs. The temporal performances are presented in Fig. 4.21.

4.6.2 Broadband operation

When the beamline is used with broadband attosecond pulses, the mirrors and gratings of the monochromator are removed from the optical path, acting on the motorized translation stages. Furthermore, the slit has to be kept completely open. The XUV light is reflected by by two mirrors that are grating-collinear, which are toroidal in 1:1 configuration. Their optical parameters are shown in Tab. 4.3.

OP2: Broadband operation	
MIRRORS	Toroidal gold
TM-06.05 (in Section 6)	2250 mm arms, $AOI = 87°$
TM-06.06 (in Section 2)	1250 mm arms, $AOI = 87.5°$

TABLE 4.3: OP2 optical parameters of the monochromator.

Compared to the original configuration of the GHHG CONDENSED beamline, where the XUV light is focused in Section 3 by an ellipsoidal mirror at 85°, here the beam undergoes two reflections although at a more grazing angle on the two toroidal mirrors, being used respectively at 87° and 87.5°. The loss of flux due to the additional reflection is compensated by the increase of reflectivity with the grazing angle.

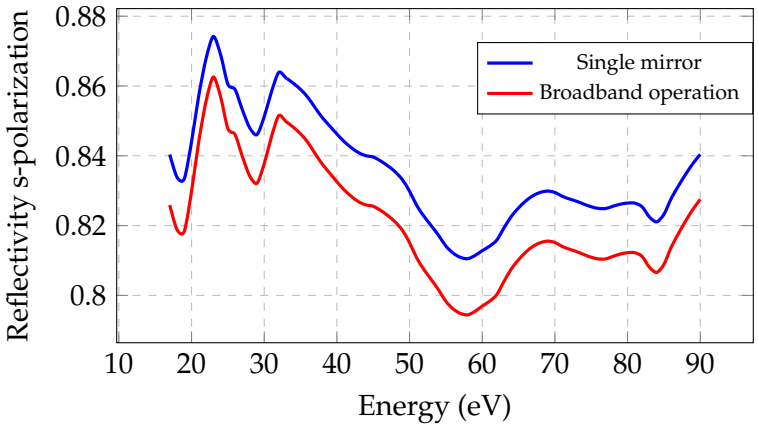

FIGURE 4.22: Transmission of the broadband option from the generation point to the TOF for s-polarized light. The reflectivity of one mirror at 85° (as in the original GHHG CONDENSED beamline) is compared to the reflectivity of two consecutive mirrors at 87° and 87.5°.

The simulated reflectivity curves are shown in Fig. 4.22 for s-polarized light. With respect to the original configuration, the expected throughput of the broadband option is decreased by few %.

4.6.3 High-flux monochromator

Depending on the requirements from the users, the monochromator may be used either as a double-stage TDC instrument with ultrafast response in the few femtoseconds range or as a single-stage with longer temporal response and higher flux. In the latter case, only the first section is used to monochromatize the light, that is later focused into the TOF spectrometer by the same toroidal mirror that is used to focus the attosecond pulses (TM-06.06) in OP2. Having a single diffracting section inserted in the optical path, the photon flux is increased, at the expenses of a hundreds of femtoseconds temporal response. Indeed, the pulse-front tilt is not corrected and it is the main factor limiting the temporal response of the monochromator. The simulated temporal performances of the gratings in the first stage is shown in Figure Fig. 4.23.

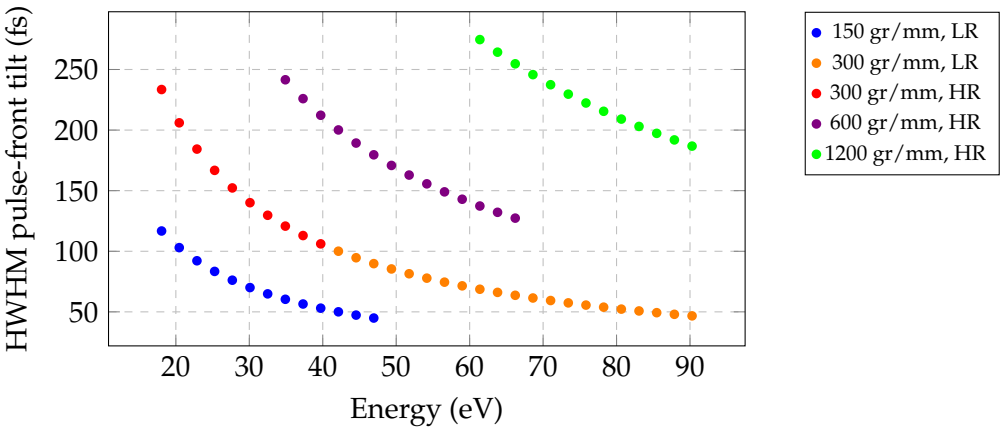

FIGURE 4.23: Simulated half width at half maximum (HWHM) pulse-front tilt given by the gratings of the first stage of the monochromator with 3.4-mrad full divergence.

4.7 Future test experiments

In this Section we will describe the test experiments, that will be performed by using the XUV monochromator. The monochromator performances will be characterized in terms of photon flux, beam size and temporal duration of the selected harmonic radiation. The methodology is described in detail in the following.

4.7.1 Efficiency

The monochomator efficiency will be measured as follows.

i) The two diffraction gratings (G-06.01 and G-06.02) are first used in zero-order diffraction configuration. The spectrum of the harmonic beam, composed by various harmonic peaks, is measured in this configuration with the XUV spectrometer in Section 5.

ii) The first grating is rotated in order to center on the slit the first diffracted order of the selected harmonic peak. The corresponding spectrum is measured as above. The diffraction efficiency of the first grating can be easily measured by comparing the spectra acquired in step i) and ii) Most of the radiation is diffracted in the order 1 when the grating is operated close to its blaze wavelength. Far from the blaze condition, the amount of radiation diffracted at order 0 increases.

ii) The second grating (G-06.02) is rotated in order to send the first diffraction order in the in the XUV spectrometer through the TOF electron spectrometer. The diffraction efficiency of the second grating can be easily measured by comparing the spectra acquired in step ii) and iii).

4.7.2 Photon flux

The photon flux on target is an important parameter that describes the number of photons per second interacting with a possible sample. The photon flux of a harmonic beam can be measured by using a calibrated photodiode. The XUV photons impinging on the active area of the photodiode create charges which are free to move. The generated photocurrent is usually in the pA to nA range and thus requires a high precision picoamperometer to be measured. Knowing the photodiode quantum efficiency and the spectrum of the impinging radiation, it is then possible to convert the measured current in number of impinging photons per second. This measurement will be performed in the case of two harmonics (H25 at 30 eV and H35 at 42.1 eV). For both cases, the flux will be measured for the operational phases OP1 and OP3.

4.7.3 Focal size

An important parameter to be measured is the quality of the spot size and its dimensions. First because a correct shape of the focal spot ensures a correct alignment of the monochromator. But even because it allows to estimate the harmonic pulse peak intensity once pulse duration is known. The actual measurement of the beam spot size in the focus will be performed by shining the selected harmonic onto the Ce:YAG crystal abvailable in Section 3. This material is commonly used as a phosphor in cathode ray tubes and white light-emitting diodes, and as a scintillator. The XUV radiation excites the Ce:YAG crystal which in response emits light in the visible (maximum wavelength 550 nm). An image of the spatial profile of the visible

light emitted by the crystal can then be acquired with a complementary metal-oxide-semiconductor (CMOS) camera. Taking into account for the relative angle between the camera and the Ce:YAG crystal, and knowing the harmonic incidence angle, it is possible to calibrate the axis of the image. After calibration, we will perform a Gaussian fit of the intensity profile extracted from the image and use the standard deviation to quantify the beam dimension along two orthogonal directions. This measurement will be performed for two harmonics, namely H25 and H35. The final size of the spot depends on the size of the harmonic source and it is expected to be below 150 μm.

4.7.4 Temporal characteristics

Since the expected time duration of the outcoming pulses from the TDC monochromator is of the order of a few femtoseconds, it can't be directly sampled with electronic devices. Furthermore, being in the wavelength range of few tens of nanometers and having a relatively low flux, it is not possible to use autocorrelation techniques. One possibility is to combine the XUV radiation with a portion of the generating infrared (IR) pulse as it is done in the FROG-CRAB technique described in Sect. 2.3.2. While this technique has been extensively tested and investigated for isolated attosecond pulses, its extension to few-femtosecond XUV pulses is not trivial and it was recently demonstrated, with the complete temporal characterization of 5-fs XUV pulses at the output of a TDC monochromator [67].

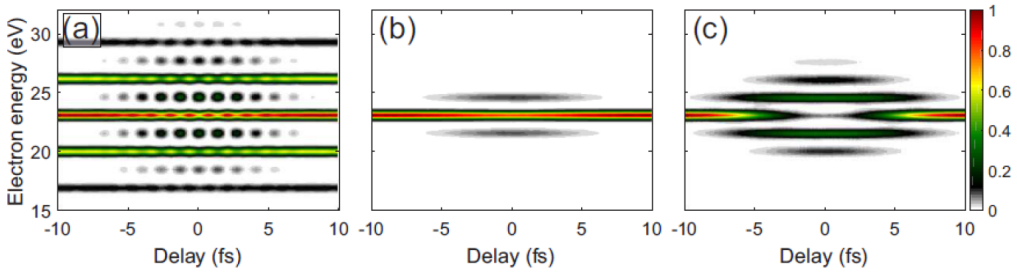

FIGURE 4.24: (a) RABBITT spectrogram calculated in the case of a complete harmonic comb (corresponding to an attosecond pulse train (APT)). (b), (c) Single harmonic spectrograms corresponding to H25, calculated assuming $I_{IR} = 10^{11}$ and 10^{12} W·cm^{-2}, respectively. Calculation parameters: temporal duration of each attosecond pulse in the train: 350 as; temporal duration of the APT: 5 fs; temporal duration of the IR pulse: 10 fs. IR center wavelength 800 nm. Both IR and XUV pulses are assumed to be transform limited. Ionization from argon.

In the case of attosecond pulse trains (characterized by a series of discrete harmonic peaks in the frequency domain), the spectrogram can be seen as a coherent superposition of isolated attosecond pulses streaking traces. As such, the collection of electron spectra is still sensitive to the XUV spectral phase. In this case, each harmonic will ionize the atom giving an electron spectrum characterized by discrete

peaks (main bands). When the IR field is present, additional peaks called sidebands (SBs) appear in between the harmonic peaks. Two indistinguishable paths lead to the formation of a given SB: i) absorption of a photon from the closest lower harmonic and additional absorption of an IR photon, ii) absorption of a photon from the closest upper harmonic and additional emission of one IR photon. These two paths interfere and thus the SB signal oscillates with twice the IR frequency, ω_{IR}, as shown in Fig. 4.24(a). In case of moderate IR peak intensities ($I_{IR} \simeq 10^{11}$ W$\cdot$ cm^{-2}), the SB signal can be analysed with the reconstruction of attosecond beating by two-photon transitions (RABBITT) method [3]. As the condition to apply RABBITT is the interference between different two-color ionization pathways, this technique can no longer be applied when a single high-order harmonic is selected from the comb. It has been recently demonstrated that it is possible to temporally characterize single harmonic pulses by employing the FROG-CRAB approach in combination with an advanced reconstruction technique [67].

Figures 4.24(b) and 4.24(c) show the simulated spectrogram after selection of a single harmonic. Additional peak pairs, spaced by $\hbar\omega_{IR}$ from the initial peak appear around zero time delay, produced by two-color ionization involving one XUV photon and at least one IR photon. As in the case of RABBITT, these peaks are called SBs and their number depends on the IR laser intensity, as shown in Figures 4.24(c), which has been obtained by increasing the IR intensity from 10^{11} to 10^{12} W$\cdot$cm^{-2}. In the case of a single harmonic peak there is only one path associated to the formation of a SB. Therefore, the SB signal does not oscillate. Nevertheless, the SB signal is still sensitive to the XUV and IR intensity envelopes and it can be used to estimate the pulse time duration. From the experimental viewpoint the temporal characteristics of harmonics H25 and H35 will be measured. The spectrograms generated by focusing H25 and H35 onto an argon or neon jet, respectively, will be measured as a function of the delay between the harmonic pulses an a portion of the fundamental IR pulse. A first rough estimation of the XUV pulse duration can be achieved directly from the FWHM of the sideband. In fact if a single pair of SBs is generated (moderate IR intensity regime), the SB yield as a function of XUV-IR temporal, SB(ω, τ), can be seen as a second order process that requires one IR photon and one XUV photon to ionize one electron. Following an approach similar to the one used for the second harmonic FROG [68], we can write:

$$SB(\omega,\tau) = \left| \int_{-\infty}^{+\infty} E'_{XUV}(t) E'_{IR}(t-\tau) e^{-i(\omega-\omega^+)t} dt \right|^2, \tag{4.3}$$

where $E'_{XUV}(t)$ and $E'_{IR}(t)$ are the electric-field envelopes of the XUV harmonic and IR pulses, respectively, and $\omega^+ = \omega_{XUV} + \omega_{IR}$, so that the previous equation refers to the upper SB (equivalent result can be obtained for the lower SB, where $\omega^- = \omega_{XUV} - \omega_{IR}$). For sufficiently long pulses, such that the phase term in Eqn. (4.3)

oscillates faster than the other terms, SB(ω, τ) can be written as follows:

$$SB(\omega = \omega^+, \tau) = SB^+(\tau) = \left| \int_{-\infty}^{+\infty} E'_{XUV}(t) E'_{IR}(t-\tau) dt \right|^2, \tag{4.4}$$

so that the SB yield, $SB^+(\tau)$, can be written as the cross correlation between the IR and XUV pulse envelopes. If the XUV and IR envelopes are Gaussians, $SB^+(\tau)$ will also have a Gaussian distribution with FWHM time duration:

$$\tau_{SB} = \sqrt{\tau'^2_{XUV} + \tau'^2_{IR}}. \tag{4.5}$$

By applying this simple expression to the experimental data it is possible to obtain a first rough estimation of the harmonic pulse duration. Nevertheless, the simple cross-correlation formula is not always accurate. In particular, it fails in case of relatively short and chirped XUV pulses.

A complete characterization of the temporal features of the harmonic pulses can be obtained by employing advanced reconstruction techniques. A very powerful technique, termed extended ptychographic iterative engine (ePIE) [69].

As 15-fs IR pulses at 1030 nm are used to generate harmonics, single harmonic peaks are quite broad and the clear aperture of the slit in Section 7 determines the spectral width of the selected portion of the XUV radiation. Therefore we can think about two families of experiments that will allow us to comprehensively test the GHHG condensed-phase beamline equipped with the monochromator. At first we will select harmonics maintaining their natural bandwidth. The monochromator will be operated in the low-energy resolution mode, with an expected pulse duration of a few-femtoseconds. Later we will operate the monochromator in the high-energy resolution mode to select a small portion of the harmonic bandwidth, associated to pulses with a duration of few-tens of femtoseconds. Furthermore, in order to test the functionality of the different gratings equipped in the monochromator, we will select two harmonics: H25 and H35. This leads us to a total of four characterization experiments to be performed: (i) H25 selected in low-energy resolution mode with a transform-limited (TL) time duration of 7.5 fs; (ii) H25 in high-energy resolution mode with a bandwidth of 120 meV; (iii) H35 selected in low-energy resolution mode with a TL of 7.5 fs; (iv) H35 selected in high-energy resolution mode giving a bandwidth of 201 meV.

Here we want to test the feasibility of such experiments by simulating the expected spectrogram and benchmarking the reconstruction procedure. In order to simulate the experiment we need to evaluate the temporal response of the monochromator. Since the optical path inside the monochromator decreases linearly with the wavelength, this forces the GDD to be almost constant and positive. In particular, it depends on the chosen grating, the photon energy and the actual XUV bandwidth. For H25 and H35 selected in low energy resolution mode, the residual GDD is estimated to be 12 fs^2 and 4 fs^2, respectively. For the same harmonics selected in high-energy

resolution scheme, a GDD of 40 fs^2 and 20 fs^2 is expected for bandwidths of 120 and 210 meV, respectively.

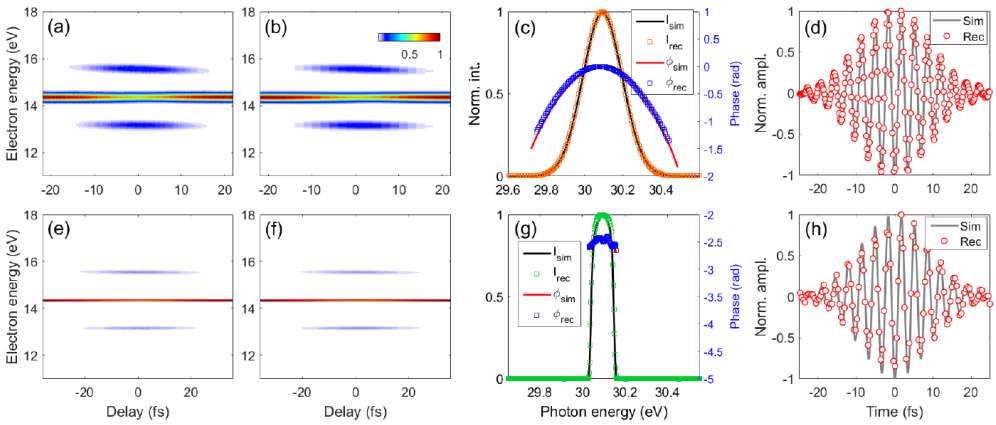

FIGURE 4.25: Spectrogram reconstruction for H25. (a) Simulated spectrogram in argon of H25 selected in low-energy resolution mode. The XUV pulse is characterized by a TL time duration of 7.5 fs and a GDD of 12 fs^2. (b) Reconstructed spectrogram after 2000 iteration of the ePIE algorithm. (c) Simulated and reconstructed XUV spectral amplitude and phase. (d) Simulated and reconstructed IR pulse. (e) to (h) display the same quantities but for H25 selected in the high energy resolution mode. In this case the harmonic radiation has a spectral bandwidth of 120 meV and a GDD of 40 fs^2.

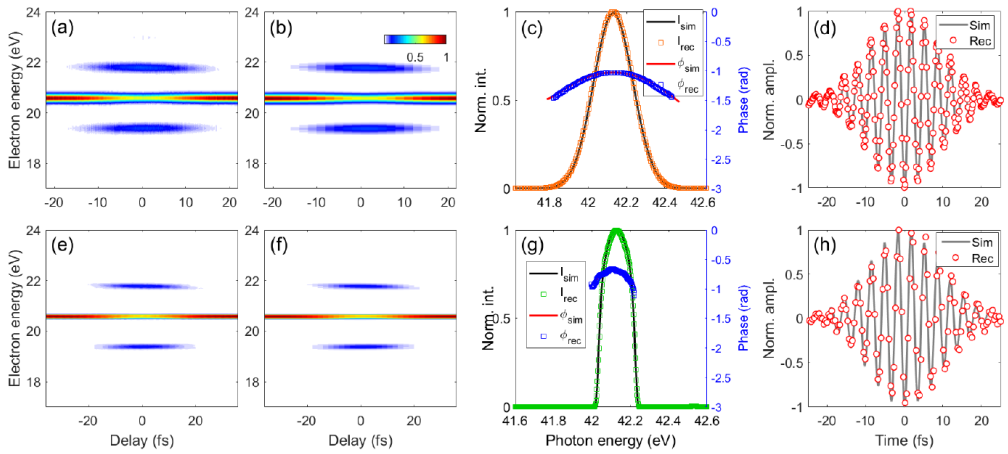

FIGURE 4.26: Spectrogram reconstruction for H35. (a) Simulated spectrogram in neon of H35 selected in low-energy resolution mode. The XUV pulse is characterized by a TL time duration of 7.5 fs and a GDD of 4 fs^2. (b) Reconstructed spectrogram after 2000 iteration of the ePIE algorithm. (c) Simulated and reconstructed XUV spectral amplitude and phase. (d) Simulated and reconstructed IR pulse. (e) to (h) display the same quantities but for H35 selected in the high energy resolution mode. In this case the harmonic radiation has a spectral bandwidth of 210 meV and a GDD of 20 fs^2.

Figures 4.25 and 4.26 show the simulated and reconstructed spectrograms, together with the IR field for the four experiments described above. The parameters

used in the calculations for the IR pulse are the following: time duration of 15 fs (FWHM in TL conditions), GDD of 20 fs^2, peak intensity of $1 \cdot 10^{11}$ $W \cdot cm^{-2}$, central wavelength 1030 nm. As it is possible to observe, ePIE technique is able to properly reconstruct the temporal and spectral characteristics of the input pulses for all the realistic cases under consideration.

Chapter 5

Characterization of a high resolution XUV grating monochromator

5.1 Introduction

The recent upgrade of HH generation in gases toward repetition rates of 50–100 kHz (10–200 μJ pulse energy), obtained with conventional Ti:Sapphire femtosecond laser amplifiers, allowed a reduction of the single-pulse photon flux. Thus having the benefit of reduced experimental data acquisition time and mitigation of undesired phenomena such as photoelectron space-charge effects revealed during time-resolved pump-probe experiments on solid samples [70, 71].
HH intrinsic bandwidth is too wide for a large class of experiments. An almost monochromatic emission with an intrinsic bandwidth as narrow as ≈50 meV has already been obtained at 26.6 eV just acting on the HH generation parameters [72]. Nevertheless, the energy resolution is often required to be higher, especially for experiments on solid samples where a narrow bandwidth is required to discern the electronic structure. This property can be achieved by means of synchrotron beamline setups [73] or plasma lamps [74] and can be extended to HHG with high-repetition laser drivers.

For these purposes, a grating monochromator with high energy resolution, i.e., below-10-meV bandwidth, has been realized using an innovative cost-effective design. Differently from low-resolution monochromators for HHs [75], in addition to the exit slit, an entrance slit is provided in order to have a reliable energy calibration almost independent from the source alignment.

Microscopy applications need to achieve focus at fixed entrance and exit arms. This condition is satisfied in the proposed configuration. In particular, a plane grating is illuminated by the converging light from a focusing mirror. The spectral focus is kept on the exit slit plane by changing the grating subtended angle, by means of an additional plane mirror. Once the spectral focusing has been achieved, the main aberration introduced by the grating is the coma. In the present design, the geometrical parameters of the focusing mirror are chosen to have, at a specific wavelength,

the coma from the grating compensated by the opposite coma given by the focusing mirror [76]. The possibility of using two interchangeable gratings made the set-up optimized for a broad energy range of 12–50 eV.
As a design test case, the set-up has been applied to the selection of the spectral lines emitted by a gas-discharge lamp, obtaining a resolving power $E/\Delta E > 3000$.

Section 5.2 describes the design and realization of the monochromator. Minimization of aberrations, resolution, and throughput performances of the realized configuration are reported in Section 5.3, demonstrating the good performance of the monochromator despite of the use of simple optical components, which are available on the market with high optical quality, although at modest prices. Section 5.4 presents a possible application of the instrument within a high repetition rate beamline dedicated to pump-probe experiments.

5.2 Monochromator design and realization

5.2.1 Optical design

The monochromator covers a broad spectral range through the selection of two or more interchangeable plane gratings (Gs), illuminated along the direction perpendicular to the grooves by the converging rays coming from a focusing cylindrical mirror (CM). The diffracted light is then reflected by a plane mirror (PM) toward a vertical exit slit acting as the filtering element. The PM optic can translate and rotate; this is required to maintain the spectral focus at the same position of the slit plane when the grating subtended angle is changed. A schematic layout of the design is shown in Fig. 5.1.

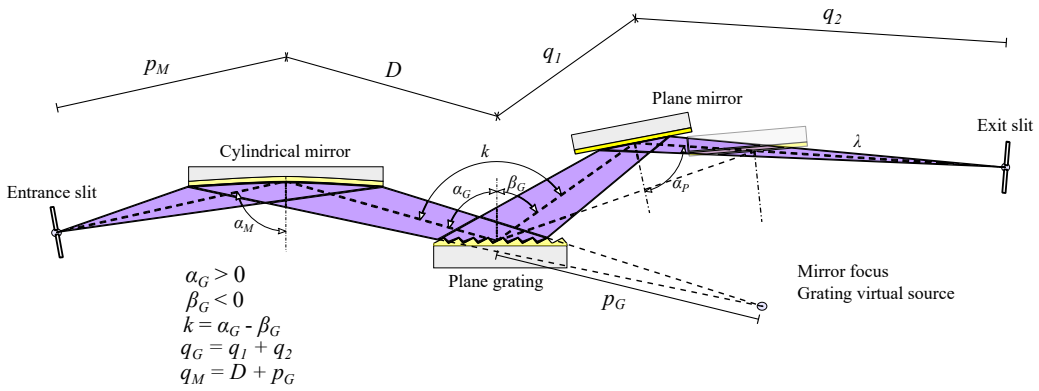

FIGURE 5.1: Tangential layout of the monochromator referred to the dispersion (spectral plane). The cylindrical mirror focus is placed after the grating. In order to maintain the final focal point at the same position, a variation of the grating subtended angle and the related translation and rotation of the plane mirror are required.

The realized configuration only cares for the tangential focus (i.e., on the plane of the spectral dispersion) provided by the CM. In the sagittal direction (i.e., perpendicular to the tangential one) the rays are assumed to be collimated from the source

and focused to the sample by some preliminary and post mirrors, as explained in Sect. 5.4. For each wavelength of interest, tangential aberrations on the focal plane must be minimized to obtain a high resolution. As demonstrated in Appx. A.1.2, the condition to have the spectral focus with fixed arms is

$$\frac{\cos\alpha_G}{\cos\beta_G} = const., \tag{5.1}$$

where α_G and β_G are the grating incidence and diffraction angles, respectively. The constant term is given by $\sqrt{p_G/q_G}$, where p_G and q_G are, respectively, the entrance and exit arms of the PG, as reported in Fig. 5.1. This condition must be fulfilled for each wavelength within the spectral interval of operation and can be expressed in terms of the grating subtended angle $k = \alpha_G - \beta_G$ as

$$\frac{\cos\left\{\arcsin\left[\frac{m\lambda\sigma}{2\cos\left(\frac{k}{2}\right)}\right] + \frac{k}{2}\right\}}{\cos\left\{\arcsin\left[\frac{m\lambda\sigma}{2\cos\left(\frac{k}{2}\right)}\right] - \frac{k}{2}\right\}} = const., \tag{5.2}$$

where σ is the groove density and m is the internal diffraction order ($m \geq 0$).
From Eqn. (5.2), the subtended angle k is calculated for each wavelength of interest; changed by translating the PM along an axis parallel to the beam output direction and rotating it around an axis passing through its center, as shown in Fig. 5.2(b). The variation of the length of q_G due to the translation of the plane mirror, i.e., the variation of the distance between the grating and the exit slit is almost negligible at grazing incidence.

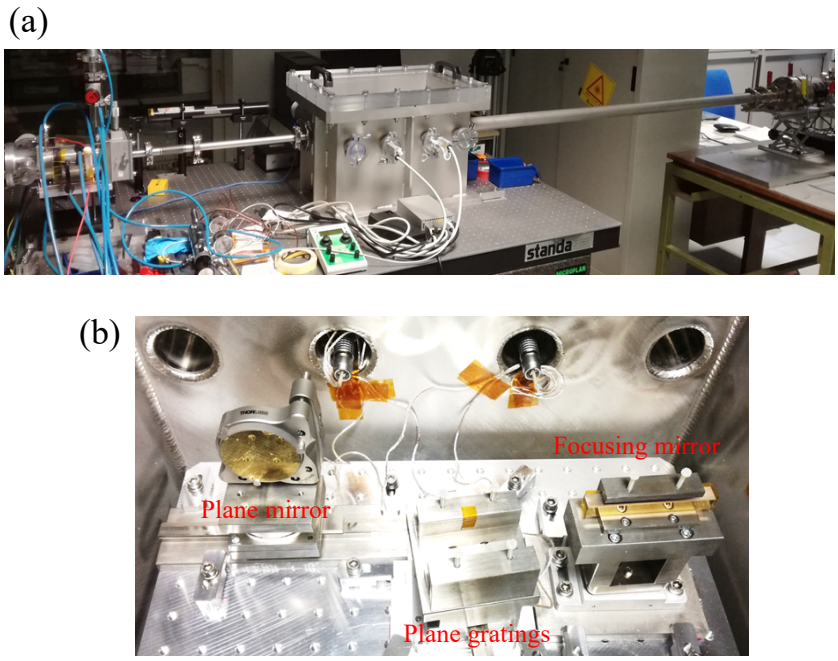

FIGURE 5.2: (a) External and (b) internal view of the three-elements monochromator vacuum chamber.

Tangential coma is the second main undesired aberration once the spectral defocusing has been corrected. This specific design allowed us to select the entrance arm p_M of the CM to have the coma given by the grating compensated by the coma that is specifically introduced by the mirror. As demonstrated in [76], the condition for coma compensation at the specific wavelength λ_C is given by

$$p_M = \left(q_G \frac{\cos^2 \alpha_{G,\lambda_C}}{\cos^2 \beta_{G,\lambda_C}} + D \right) \left[1 + A_{\lambda_C} \left(q_G \frac{\cos^2 \alpha_{G,\lambda_C}}{\cos^2 \beta_{G,\lambda_C}} + D \right)^{-1} \right]^{-\frac{1}{2}}, \tag{5.3}$$

where D is the mirror-to-grating distance, and α_{G,λ_C} and β_{G,λ_C} are the grating incidence and diffraction angles at the wavelength λ_C, respectively. The coefficient A_{λ_C} is given by

$$A_{\lambda_C} = 2 q_G \frac{1}{\tan \alpha_M} \frac{\cos^3 \alpha_{G,\lambda_C}}{\cos^4 \beta_{G,\lambda_C}} \left(\sin \beta_{G,\lambda_C} + \sin \alpha_{G,\lambda_C} \frac{\cos^2 \beta_{G,\lambda_C}}{\cos^2 \alpha_{G,\lambda_C}} \right). \tag{5.4}$$

The output bandwidth at FWHM is defined as

$$\Delta\lambda_{FWHM} = \frac{\cos \beta_G}{m \sigma q_G} W_{OUT}, \tag{5.5}$$

where W_{OUT} is the exit slit aperture. The optimal condition for no loss of flux is obtained by the following relation between the entrance and exit slits apertures

$$W_{OUT} = W_{IN} \left(\frac{q_M}{p_M} \right) \left(\frac{q_G}{p_G} \right) \left(\frac{\cos \alpha_G}{\cos \beta_G} \right), \tag{5.6}$$

where the three multiplication factors which give the projection of the entrance slit to the exit slit plane are, respectively: the mirror magnification (q_M/p_M), the grating magnification (q_G/p_G), and the grating anamorphic factor $(\cos \alpha_G / \cos \beta_G)$.

5.2.2 Parameters selection

The design has been demonstrated in the 12–50 eV region. Two gold-coated gratings manufactured by Newport-Richardson Gratings^{TM} were used, respectively, with 600 gr/mm (G_1) and 1200 gr/mm (G_2), both of them with 5.2° nominal blaze angle.
The coma-correction energies $E_C = hc/\lambda_C$ were 20.6 eV (60 nm) and 41.3 eV (30 nm), respectively, for G_1 and G_2. The subtended angle at E_C was selected equal to 156°. Further parameters, such as the grating output arm q_G, the mirror-to-grating distance D, and the CM incidence angle α_M were selected to satisfy both spectral bandwidth, as will be discussed in sub-Sect. 5.3.3 and compact realization requirements. Monochromator parameters are reported in Table 5.1.

TABLE 5.1: Parameters of the monochromator.

Entrance Slit Dimensions				**35 μm × 1 mm**	
Focusing Mirror		**Gratings G_1-G_2**		**Plane Mirror**	
p_M	675 mm	p_G	363 mm	q_1 range	60–200 mm
q_M	478 mm	q_G	2070 mm	q_2 range	1870–2010 mm
α_M	87°	k range	149°–158°	α_P	77.5°–82°
R_M (tang. radius)	10,700 mm	G_1 groove density	600 gr/mm		
		G_1 energy range	12–25 eV		
		G_2 groove density	1200 gr/mm		
		G_2 energy range	25–50 eV		
		D	115 mm		

Once the geometrical design was defined, the subtended angles were calculated from Eqn. (5.2). In the adopted configuration the gratings are used at a variable subtended angle, therefore the loss of efficiency due to the introduction of the additional plane mirror is almost recovered because the wavelength scan is maintained close to the blaze condition of maximum efficiency, shown in Fig. 5.3.
The FWHM energy bandwidth $\Delta E_{FWHM} = E\Delta\lambda_{FWHM}/\lambda$ is calculated from Eqn. (5.6), for the entire spectral range of the two gratings.
The entrance slit width was set to about 35 $\pm$ 3 μm, which is the typical width of a HHs source, with the laser focused tightly to reach sufficient intensity to ionize the gas [77].

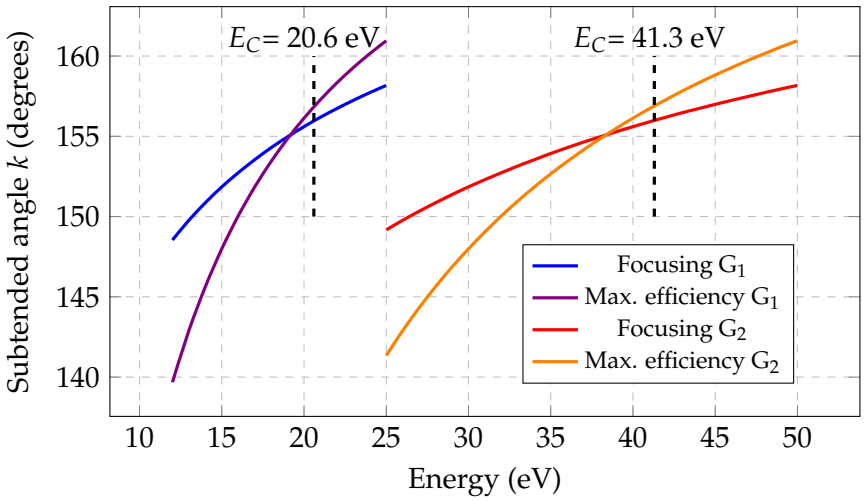

FIGURE 5.3: Comparison between the subtended angles adopted to satisfy the focusing condition and the ones to obtain maximum efficiency.

5.3 Characterization results

5.3.1 Spectral characterization

The spectral characterization of the monochromator was performed using the discrete emission lines in the 12.4–50 eV energy range of a gas-discharge lamp filled with different noble gases: He, Ne, and Ar. All the measurements were performed using a cooled CCD camera detector (Princeton Instruments PIXIS) with low readout noise ($3e^-$ rms), placed in the image plane, i.e., with the exit slit completely open, in a spectrometer fashion. The CCD format was 1340 × 1300 pixels, with 20 μm × 20 μm pixel size, determining the resolution of the detection.

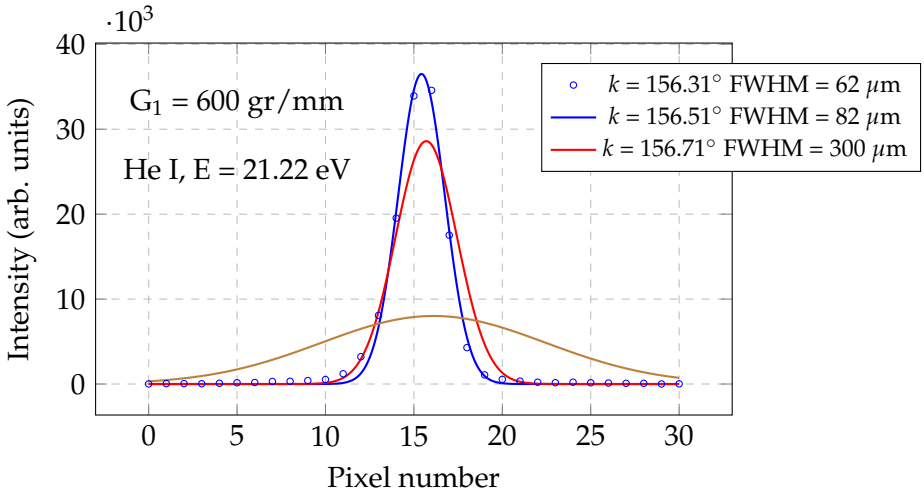

FIGURE 5.4: Line profile for k variation of 0.2° and 0.4° at 21.22 eV, G_1 grating.

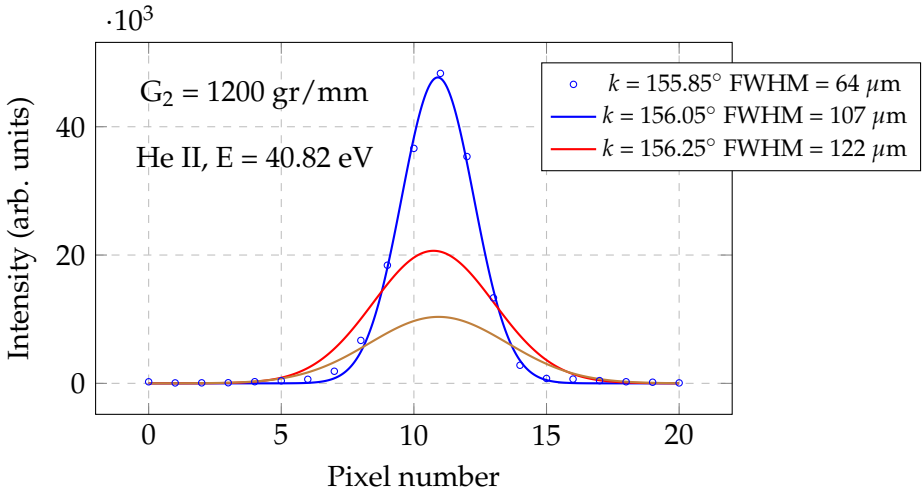

FIGURE 5.5: Line profile for k variation of 0.2° and 0.4° at 40.82 eV, G_2 grating.

The evaluation of the tangential defocusing aberration was performed by a Gaussian interpolation of the acquired CCD spectral image, before and after a variation

of k from its nominal position (associated to a specific photon energy) of 0.2° and 0.4°. In Figs. 5.4 and 5.5, the emission lines of He I ($1s^2 \rightarrow 1s2p$) at 21.22 eV and He II ($1s \rightarrow 2p$) at 40.82 eV are shown.

By applying Eqn. (5.6), we calculate an image width of 58 μm with a 35 μm entrance slit in the entire spectral range. The expression accounts only for the entrance slit magnification and not for residual aberrations. The typical width of the spectral lines at the optimum angle is in the range 60-65 μm, confirming the correction of defocusing and coma given by the design. The residual mismatch between theoretical and measured values is mainly due to the uncertainty on the width of the entrance slit.

5.3.2 Comparison with simulations

A comparison between the obtained CCD image widths in the tangential direction and the ray-tracing simulation results [78], performed with a source placed immediately before the entrance slit (assuming an angular half-divergence of 2.5 mrad $\times$ 2.5 mrad), has been performed. From Eqn. (5.5), this configuration allows for maintaining a constant value of the entrance slit magnification on the image plane ($M_t = 1.67$) within the entire spectral range. Therefore, only aberrations are responsible of a change in the image width when changing the energy. When we are not selecting E_C, we have no defocusing, therefore the main aberration to consider is the tangential coma.

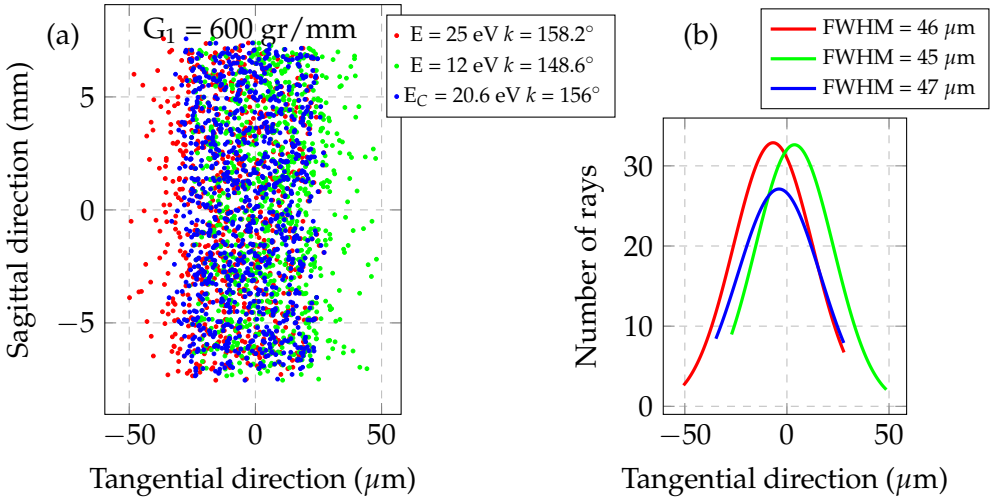

FIGURE 5.6: Ray-tracing results of the entrance slit projected to the output for the values given in Table 5.1 (G_1 grating). (a) Image shape for three different energies and (b) width in the tangential direction.

As represented in Fig. 5.6(a), at the two edge energies of G_1 some coma appears, as can be seen from the slightly asymmetrical images at 12 eV and 25 eV, although, as shown in Fig. 5.6(b) the width at FWHM is almost constant.

In Figure 5.7, the CCD acquired images at 13.48 eV (Ar II), and 21.22 eV (He I) emission lines are reported for the same grating. Coma aberration is not evident.

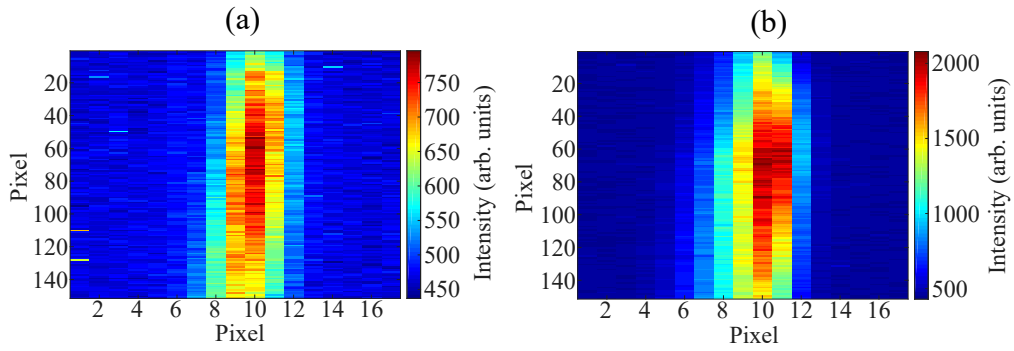

FIGURE 5.7: Acquired CCD images at the image plane of two emission lines selected by the G_1 grating. (a) 13.48 eV; and (b) 21.22 eV.

5.3.3 Resolution of the instrument

The output bandwidth ΔE_{FWHM} of a monochromator depends on both the widths of the entrance and exit slit. As the exit slit width is decreased, the effective bandwidth will generally decrease. If the exit slit is narrower than the projection of the entrance slit, the bandwidth would not be reduced appreciably. This situation is undesirable in that diffracted energy is lost. The opposite situation is also undesirable, since the FWHM bandwidth is excessively large (or, similarly, an excessively wide band of diffracted wavelengths is accepted by the slit). Therefore, the situation is optimal when the exit slit width matches the width of the spectral image, i.e. the relative intensity is maximized and the FWHM bandwidth is minimized.

Considering the discrete spectral lines emitted by the source, the measured spectral widths are reported in Table 5.2 and Fig. 5.8. The resulting spectral bandwidth is below 10 meV, with a ≈60 μm wide projection of the entrance slit. The measured values are best fitted assuming a 37 μm wide input slit, which is well within the uncertainty of the slit mounting.

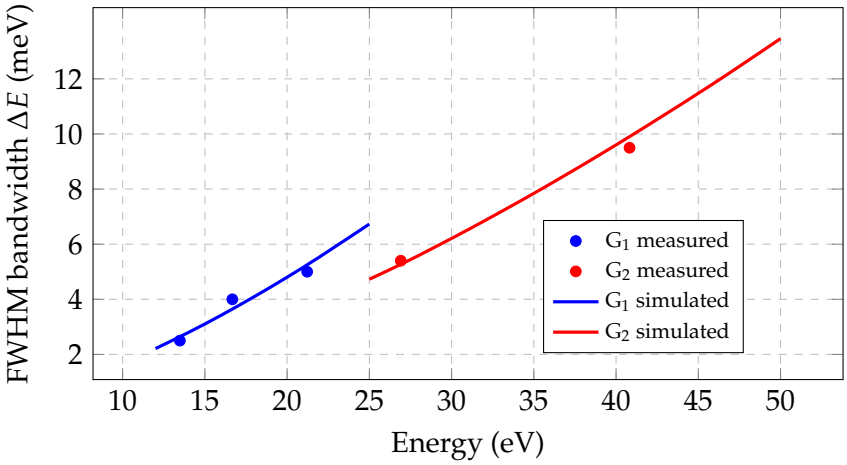

FIGURE 5.8: Full-width-at-half-maximum (FWHM) bandwidth measured on the exit slit plane (dot-points) and theoretical best-fit assuming a 37 μm entrance slit (solid lines).

TABLE 5.2: Widths of the spectral lines measured on the exit slit plane.

Energy (eV)	Grating Type	W_{OUT} (μm)	ΔE (meV)
13.48	G_1	60	2.5
16.67	G_1	70	4.0
21.22	G_1	60	5.0
26.91	G_2	65	5.4
40.82	G_2	60	9.5

5.3.4 Overall Efficiency

The efficiencies of the optical elements of the configuration (i.e., focusing mirror, plane grating, and plane mirror) were measured in the 12–62 eV region at the Circular Polarization (CiPo) beamline at ELETTRA Synchrotron [50]. The total efficiency of the instrument, defined as the product of the grating diffraction efficiency and the mirrors reflectivity was measured. As shown in Fig. 5.9, the efficiency of the monochromator for s-polarized light is in the 8–15% range. The efficiency of gratings is between 13–27%. The theoretical efficiency for p-polarized light was obtained by combining simulations with s-polarization experimental results. During the measurements, for each photon energy, the two gratings performed the spectral selection at the subtended angle for which the tangential defocusing is corrected. In order to retrieve the efficiency, the optics were positioned on an X-ray reflectometer [51] which was installed at the output of the beamline.

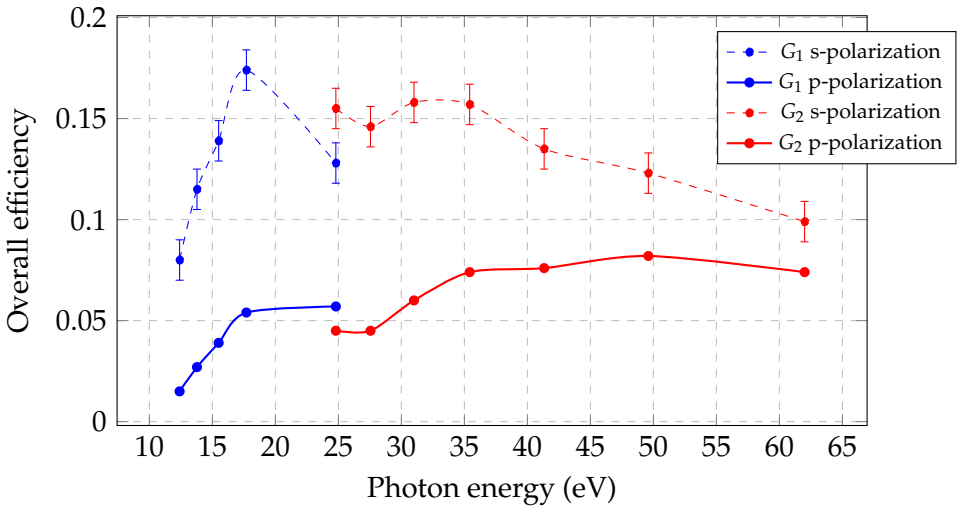

FIGURE 5.9: Experimental total efficiency of the monochromator for s-polarized light (dashed) and theoretical for p-polarized light (solid). For each measurement, the subtended angle has been selected to satisfy the tangential focus condition.

5.4 Application to HHs Selection

As schematized in Fig. 5.10, the high vacuum chamber containing the entire monochromator set-up, made up of three optical elements, can be used for high resolution applications dedicated to pump-probe IR-XUV experiments. After HHs gneration, a preliminary toroidal mirror TM_1 is used for the XUV-beam focusing on the entrance slit in the tangential (dispersion) direction. Similarly, after the monochromator exit slit, the toroidal mirror TM_2 in the XUV-IR recombination chamber acts to focus the XUV beam toward the experimental chamber. The output arm has to be long enough to accommodate such a chamber. Both TM_1 and TM_2 operate in the 1:1 configuration in order to minimize the aberrations. The total length of the high resolution monochromator setup (between entrance and exit slit) is approximately 3 m. The focus in the plane parallel to the slits, i.e. the sagittal plane, is assured by a suitable choice of the sagittal radii of the two pre- and post-toroidal mirrors: TM_1 is designed to collimate the beam coming from the source in the vertical direction and TM_2 to focus it toward the experimental chamber. These mirrors are assumed to be operated at incidence angles grater than 86° in order to have high reflectivity and high insensitivity to the polarization of the incoming light. The arms are chosen typically equal to 700 mm, in order to avoid a degradation of TM_1 caused by the plasma-debris from the HHG gas nozzle.

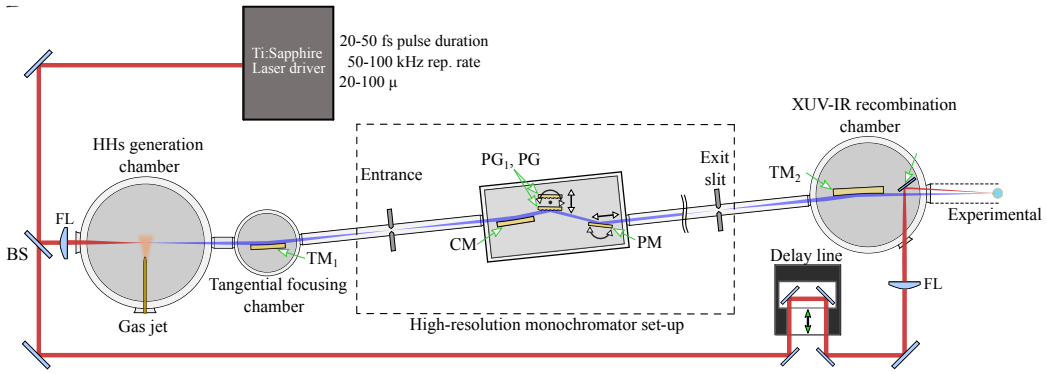

FIGURE 5.10: Top-view schematic representing the insertion of the high resolution monochromator within a high-repetition rate beamline dedicated to pump-probe experiments. The system includes a laser system and optics, the XUV beamline, and the IR delay-line. BS, beam splitter; FL, plano-convex focusing lens; TM_1, tangential focusing and sagittal collimating toroidal mirror; CM, tangential focusing cylindrical mirror; PG_1-PG_2, interchangeable rotating plane gratings; PM, rotating-translating plane mirror; TM_2, tangential focusing and sagittal focusing toroidal mirror; RM, IR recombination mirror.

Chapter 6

Conclusions

In this Chapter, the main results achieved on the three topics covered in this dissertation are summarized.

- In Chapter 3, the measurements of diffraction efficiency of commercially available replica reflection gratings which are applied to the realization of monochromators for soft X-rays in the classical and off-plane geometry have been performed. The efficiency curves for different blaze wavelengths have been measured at the Circular Polarization beamline of the ELETTRA Synchrotron (Italy) and simulated with GSolver, which is a full vector implementation of a class of algorithms known as Rigorous Coupled Wave Analysis (RCWA). Efficiencies as high as 45% at 100 eV and 35% at 310 eV has been measured for OPM grating configurations for soft X-rays. Despite of the use of low-price commercially-available replica gratings, we demonstrate the capability of maintaining high efficiency up to the Carbon K-edge. Compared to the CDM configuration, the efficiency of a single grating OPM is increased by a factor of almost 2 at 100 eV and almost 7 at 310 eV. The results confirm the benefit of employing the OPM configuration not only for the realization of single-grating monochromators, but even for double-grating time-delay compensated ones even in the soft X-ray region.

- Chapter 4 presents the project addressed to the design, development, construction, calibration, testing, and operation of a time-compensated monochromator to be integrated to be integrated on the GHHG Condensed beamline at the Extreme Light Infrastructure – Attosecond Light Pulse Source ELI-ALPS, the large European facility being built in Szeged, Hungary. It should provide users of the ELI-ALPS facility the possibility of selecting continuously different XUV photon energy regions of the generated high harmonic radiation. The monochromator has to be designed to avoid further temporal stretching of the pulses by i.e. pulse-front tilt, and preserve an XUV pulse duration allowed by the inherent properties of the generation process. The software which provides to the beamline three different operational modes has been realized.

- In Chapter 5, the performance of a three-elements grazing-incidence monochromator designed for high spectral resolution HHs experiments are presented.

The optical configuration uses a plane grating illuminated by the light converging from a cylindrical concave focusing mirror. The set-up maintains the spectral focus in a fixed position on the output-slit-plane by changing the subtended angle on the grating. The realized monochromator works in the 12–50 eV region. A resolving power in the 3700–5200 range (corresponding to an output bandwidth lower than 10 meV) has been achieved in the whole region of operation. When compared with synchrotron plane grating monochromators, for which the working range is between 60–410 eV, comparable performances in terms of resolution (5000–20,000) and efficiency have been obtained. The particularity of this design is related to the cost-to-benefit ratio. Since all the optical components used in the monochromator are available on the market with high optical quality and modest prices, the configuration can be useful for cost-effective instrumentation, both on synchrotron beamlines and on novel laboratory-based applications using HHs sources at high-repetition rates.

Chapter 7

Publications

List of publications on international journals

J1) Frassetto F.; Fabris N.; Miotti P. and Poletto L. "Design Study of Time-Preserving Grating Monochromators for Ultrashort Pulses in the Extreme-Ultraviolet and Soft X-Rays" Photonics 2017, 4, 14.
DOI: 10.3390/photonics4010014

J2) Lam R. K. et al. "Two-photon absorption of soft X-ray free electron laser radiation by graphite near the carbon K-absorption edge" Phys. Rev. Lett. 2018, 703, pp. 112–116.
DOI: 10.1103/PhysRevLett.120.023901.

J3) Lucchini M.; Lucarelli G. D.; Murari M.; Trabattoni A.; Fabris N.; Frassetto F.; De Silvestri S.; Poletto L. and Nisoli M. "Few-femtosecond extreme-ultraviolet pulses fully reconstructed by a ptychographic technique" Opt. Express 2018, 26, pp. 6771–6784.
DOI: 10.1364/OE.26.006771.

J4) Lam R. K. et al. "Soft X-Ray Second Harmonic Generation as an Interfacial Probe" Phys. Rev. Lett. 2018, 120, pp. 023901.
DOI: 10.1103/PhysRevLett.120.023901.

J5) Zhonghui N. et al. "Spin-ARPES EUV beamline for ultrafast materials research and development" Applied Sciences 2019, 9, 370.
DOI: 10.3390/app9030370.

J6) Fabris N.; Miotti P.; Frassetto F. and Poletto L. "A High Resolution XUV Grating Monochromator for the Spectral Selection of Ultrashort Harmonic Pulses" Applied Sciences 2019, vol. 9, 2502.
DOI: 10.3390/app9122502.

List of publications on conference proceedings

C1) Bonora S.; Fabris N.; Frassetto F.; Giovine E.; Miotti P.; Quintavalla M. and Luca Poletto "Design of compressors for FEL pulses using deformable gratings" SPIE Optics + Optoelectronics, SPIE Proceedings Vol. 10237, 23 June 2017.
DOI: 10.1117/12.226747310.1117/12.2267473.5463398582001.

C2) Miotti P.; Fabris N.; Frassetto F.; Turchini S.; Zuppella P. and Poletto L. "Soft x-ray grating compressor for free-electron-laser pulses" Advances in X-Ray/EUV Optics and Components XII, August 2017.
DOI: 10.1117/12.2275031.

C3) Fabris N.; Frassetto F.; Miotti P. and Poletto L. "Design and realization of a grazing-incidence plane-grating monochromator" SPIE Optical Engineering + Applications, August 2018.
DOI: 10.1117/12.2319691.

C4) Lucchini M.; Lucarelli G. D.; Murari M.; Trabattoni A.; Fabris N.; Frassetto F.; De Silvestri S.; Poletto L. and Nisoli M. Generation and complete temporal characterization of 5-fs EUV pulses The European Physical Journal Conferences, vol. 205:02009, January 2019.
DOI: 10.1051/epjconf/201920502009.

C5) Miotti P.; Fabris N.; Frassetto F.; Spezzani C. and Poletto L. Design and realization of a XUV plane-grating monochromator at variable included angle AIP Conference Proceedings, vol. 2054(1):060023, January 2019.
DOI: 10.1063/1.5084654.

C6) Frassetto F.; Zuppella P.; Samparisi F.; Fabris N. and Poletto L. Transition metal coatings for reflection polarimeters in the 50-100 eV region X-Ray Free-Electron Lasers: Advances in Source Development and Instrumentation, April 2019.
DOI: 10.1117/12.2522256.

C7) Fabris N.; Frassetto F.; Miotti P.; Samparisi F.; Spezzani C.; Zuppella P. and Poletto L. Comparison between classical and off-plane diffraction efficiency for the soft x-ray region X-Ray Free-Electron Lasers: Advances in Source Development and Instrumentation, April 2019.
DOI: 10.1117/12.2522609.

Appendix

A.1 Aberrations of a uniform line-space toroidal grating

We consider here a toroidal-surface grating with rectilinear uniform grooves parallel to z as shown in Fig. A.1. The analytical formulation of the operating conditions is based on the calculation of the light-path function, F, of a ray emitted from the point source A. Point B is the nominal focal point of the wavelength λ diffracted in the m^{th} order by the grating. The condition for two rays diffracted from adjacent grooves to reinforce at B is that their path difference must equal $m\lambda$.

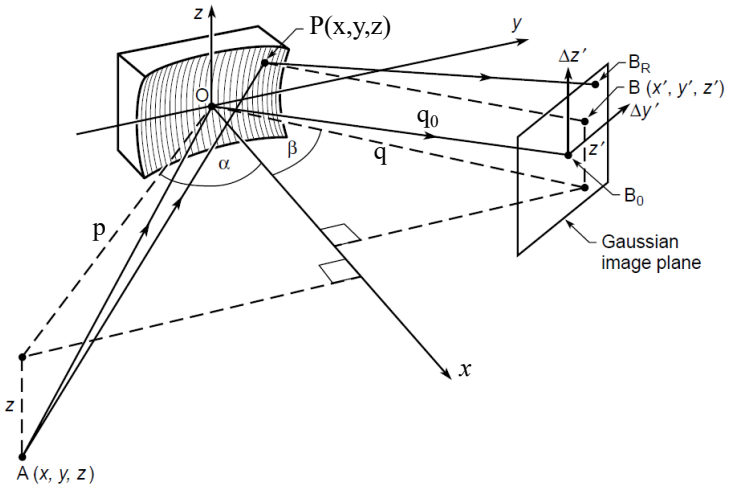

FIGURE A.1: Geometry and notation for grating theory. The axes and the rays are represented by solid lines and other distances by dashed lines. B is a general point, B_0 the Gaussian image point, and B_R the arrival point of the ray.

The light-path function is defined as $F = \langle AP \rangle + \langle PB \rangle + nm\lambda$, naming n the groove number at P counted from the origin O: $n = \sigma y$, where σ is the constant groove density. Taking into account the equation of the toroidal surface, the distances $\langle AP \rangle$ and $\langle PB \rangle$ can be defined as functions of the variables α, β, p, q, y and z, where α is the angle of incidence, β is the angle of diffraction, p and q are the lengths of the entrance and exit arms respectively (i.e. the distances between A and the grating center, O, and between O and B respectively), y and z span on the grating surface. The first two terms of the light-path function can be expressed as a power series of y

and z, assuming A(x,y,z=0):

$$\langle AP\rangle + \langle PB\rangle = p + q + F_{20}\cdot y^2 + F_{02}\cdot z^2 + F_{30}\cdot y^3 + F_{12}\cdot yz^2 + O(y^4, z^4), \quad \text{(A.1)}$$

where the series has been truncated to the third-order terms. For a toroidal-surface with tangential radius R and sagittal radius ρ, the F_{ij} terms are:

$$F_{20} = \frac{1}{2}\left[\left(\frac{\cos^2\alpha}{p} - \frac{\cos\alpha}{R}\right) + \left(\frac{\cos^2\beta}{q} - \frac{\cos\beta}{R}\right)\right], \quad \text{(A.2)}$$

$$F_{02} = \frac{1}{2}\left[\left(\frac{1}{p} - \frac{\cos\alpha}{\rho}\right) + \left(\frac{1}{q} - \frac{\cos\beta}{\rho}\right)\right], \quad \text{(A.3)}$$

$$F_{02} = \frac{1}{2}\left[\frac{\sin\alpha}{p}\left(\frac{\cos^2\alpha}{p} - \frac{\cos\alpha}{R}\right) + \frac{\sin\beta}{q}\left(\frac{\cos^2\beta}{q} - \frac{\cos\beta}{R}\right)\right], \quad \text{(A.4)}$$

$$F_{02} = \frac{1}{2}\left[\frac{\sin\alpha}{p}\left(\frac{1}{p} - \frac{\cos\alpha}{\rho}\right) + \frac{\sin\beta}{q}\left(\frac{1}{q} - \frac{\cos\beta}{\rho}\right)\right]. \quad \text{(A.5)}$$

The terms F_{ij} depend only on the geometrical parameters, and the series has been truncated to the third-order terms.
According to Fermat's principle of least time, the Gaussian image point B_0 of the central ray passing on $(y,z) = (0,0)$ is located such that F will be an extreme for any point P. Since points A and B_0 are fixed, while point P can be any point on the surface of the grating, aberration-free image focusing is obtained by the conditions

$$\frac{\partial F}{\partial y} = 0 \quad \text{(A.6)}$$

and

$$\frac{\partial F}{\partial z} = 0, \quad \text{(A.7)}$$

which must be satisfied simultaneously by any pair of y and z values on the grating surface. This is possible only if all F_{ij} terms are set to zero.
Instead, generally $\partial F/\partial y$ and $\partial F/\partial z$ are functions of y and z and can not be made zero for any y, z. In particular, when the point P wanders over the grating surface, diffracted rays fall on slightly different points on the focal plane and an aberrated image is formed. With reference to Fig. A.1 aberrations are displacements of B with respect to B_0. The nonzero terms of the derivatives of the optical path function F give rise to the aberration terms. Indeed, since the partial derivatives have the geometrical significance of angles, the maximum tangential (y) and sagittal (z) displacements of the reflected rays from the true focus B_0, having coordinates q_0, β_0, and z_{B_0} can be calculated as

$$\Delta_{tan} = \frac{q_0}{\cos\beta_0}\frac{\partial F}{\partial y}\bigg|_{y=L_{tan}, z=L_{sag}} \quad \text{(A.8)}$$

and

$$\Delta_{sag} = q_0\,\frac{\partial F}{\partial z}\bigg|_{y=L_{tan}, z=L_{sag}}, \quad \text{(A.9)}$$

where ($2L_{tan}$) x ($2L_{sag}$) is the illuminated area on the mirror surface. For the partial derivatives of order n that do not vanish, these displacements correspond to aberrations of order n in the focal plane.

A.1.1 Toroidal mirror in Rowland mounting

When working with a toroidal surface, incidence and reflection angles are equal (α_M=β_M=$\beta_{0,M}$), as stated by Snell's law. The the previous Eqns. (A.2)–(A.5) become

$$F_{20} = \frac{1}{2}\cos^2\alpha_M\left(\frac{1}{p}+\frac{1}{q}-\frac{2}{R\cos\alpha_M}\right), \tag{A.10}$$

$$F_{02} = \frac{1}{2}\left(\frac{1}{p}+\frac{1}{q}-\frac{2\cos\alpha_M}{\rho}\right), \tag{A.11}$$

$$F_{30} = \frac{1}{2}\sin\alpha_M\cos\alpha_M\left[\frac{1}{p}\left(\frac{\cos\alpha_M}{p}-\frac{1}{R}\right)-\frac{1}{q}\left(\frac{\cos\alpha_M}{q}-\frac{1}{R}\right)\right], \tag{A.12}$$

$$F_{12} = \frac{1}{2}\sin\alpha_M\left[\frac{1}{p}\left(\frac{1}{p}-\frac{\cos\alpha_M}{\rho}\right)-\frac{1}{q}\left(\frac{1}{q}-\frac{\cos\alpha_M}{\rho}\right)\right]. \tag{A.13}$$

Therefore, in order to have stigmatic imaging, two conditions must be fulfilled: $F_{20}=0$ and $F_{02}=0$, which give:

$$\frac{1}{p}+\frac{1}{q_0} = \frac{2}{R\cos\alpha_M} = \frac{2\cos\alpha_M}{\rho}, \tag{A.14}$$

from which it is possible to calculate the mirror radii. The main residual aberrations are the third-order terms, namely the tangential and sagittal coma, which are controlled respectively by F_{30} and F_{12}. Let us indicate as $M = p/q_0$ the ratio between the entrance and exit arms. For $M > 1$, the mirror is used to demagnify the source. The sizes of the illuminated portion on the mirror are $L_{tan} = Dp/\cos\alpha_M$, $L_{sag} = Dp$, where D is the half-divergence of the source. After some elaborations, the tangential ΔC_{tan} and sagittal ΔC_{sag} coma from a toroidal mirror in a stigmatic configuration are calculated from Eqns. (A.8) and (A.9) as

$$\Delta C_{tan} = 3\frac{q_0}{\cos\alpha_M}F_{30}L_{tan}^2 = \frac{3}{4}pD^2\frac{M^2-1}{M}\tan\alpha_M \tag{A.15}$$

and

$$\Delta C_{sag} = 2q_0F_{12}L_{tan}L_{sag} = \frac{1}{2}pD^2\frac{M^2-1}{M}\tan\alpha_M = \frac{2}{3}\Delta C_{tan}. \tag{A.16}$$

For a toroidal mirror with unity magnification in the so-called Rowland mounting, i.e. $p = q_0 = R\cos\alpha$ and $M = 1$, the coma aberration is fully canceled since both F_{30} and F_{12} are null. On the contrary, the higher the demagnification, the higher the coma, as stated by Eqns. (A.15) and (A.17).

A.1.2 Defocusing correction of a plane grating illuminated by converging light

When working with a plane grating $R = \rho = \infty$. Furthermore, if the grating is illuminated by the converging light coming from a preliminary optic the entrance arm p has to be considered negative in Eqn. (A.1). Then from Eqn. (A.2) we obtain the term:

$$F_{20} = \frac{1}{2}\left(-\frac{\cos^2\alpha_G}{p} + \frac{\cos^2\beta_G}{q_0}\right). \tag{A.17}$$

The condition $F_{20} = 0$ gives the equation to correct for the defocusing:

$$\frac{cos^2\alpha_G}{cos^2\beta_G} = \frac{p}{q_0}. \tag{A.18}$$

From the previous expression, the condition to have constant arms, p and q_0, at different wavelengths is

$$\frac{\cos\alpha_G}{\cos\beta_G} = \frac{\cos\alpha_G}{\cos k - \alpha_G} = const., \tag{A.19}$$

where $k = \alpha_G - \beta_G$ is the subtended angle. Therefore, a monochromator with a uniform line-space grating illuminated in converging light has to work at variable subtended angle to have fixed entrance and exit slits.

Bibliography

[1] New G. H. C. and Ward J. F. "Optical Third-Harmonic Generation in Gases". In: *Phys. Rev. Lett.* 10(19) (1967), pp. 556–559.

[2] Pellegrini C. "The history of X-ray free electron lasers". In: *The European Physical Journal H* 37(5) (2012), pp. 659–708.

[3] Paul P. M.; Toma E. S.; Breger P.; Mullot G.; Augè F.; Balcou Ph.; Muller H. G.; Agostini P. "Observation of a Train of Attosecond Pulses from High Harmonic Generation". In: *Science* 292(5522) (2001), pp. 1689–1692.

[4] Hentschel M. et al. "Attosecond metrology". In: *Nature* 414(6863) (2001), pp. 509–513.

[5] Klünder K. et al. "Probing single photon ionization on the attosecond time scale". In: *Phys. Rev. Lett.* 106(14) (2011), p. 143002.

[6] Krausz F. and Ivanov M. "Attosecond physics". In: *Rev. Mod. Phys.* 81(1) (2009), pp. 163–234.

[7] Wheeler J.A. et al. "Attosecond lighthouses from plasma mirrors". In: *Nature Photonics* 6 (2012), pp. 829–833.

[8] Drescher M. et al. "Time-resolved atomic inner-shell spectroscopy". In: *Nature* 419(6909) (2002), pp. 803–807.

[9] Muller H.G. "Reconstruction of attosecond harmonic beating by interference of two-photon transitions". In: *Appl. Phys. B* 74(1) (2002), pp. 17–21.

[10] J. et al. Itatani. "Attosecond streak camera". In: *Phys. Rev. Lett.* 88(17) (2002), p. 173903.

[11] Sansone G. et al. "Isolated Single-Cycle Attosecond Pulses". In: *Science* 314(5798) (2006), pp. 443–446.

[12] Goulielmakis E. et al. "Direct measurement of light waves". In: *Science* 305(5688) (2004), pp. 1267–1269.

[13] Tzallas P.; Skantzakis E.; Kalpouzos C.; Benis E. P.; Tsakiris G. D. and Charalambidis D. "Generation of intense continuum extreme-ultraviolet radiation by many-cycle laser fields". In: *Nat. Phys.* 3(12) (2007), pp. 846–850.

[14] Wu Y. et al. "Generation of high-flux attosecond extreme ultraviolet continuum with a 10 TW laser". In: *Appl. Phys. Lett.* 102(20) (2013), p. 201104.

[15] Popmintchev T. et al. “Bright Coherent Ultrahigh Harmonics in the keV X-ray Regime from Mid-Infrared Femtosecond Lasers”. In: *American Association for the Advancement of Science* 336(6086) (2012), pp. 1287–1291.

[16] Corkum P. B. “Plasma perspective on strong-field multiphoton ionization”. In: *Physical Review Letters* 71(13) (1993), pp. 1994–1997.

[17] Schafer K. J.; Yang B. and Kulander K. C. “Above threshold ionization beyond the high harmonic cutoff”. In: *Physical Review Letters* 70 (1993), pp. 1599–1602.

[18] Lewenstein M.; Balcou P.; Ivanov M. Y.; LHuillier A. and Corkum P. B. “Theory of high-order harmonic generation by low-frequency laser fields”. In: *Physical Review A* 49(3) (1994), pp. 2117–2132.

[19] Farkas G. and Toth C. “Proposal for attosecond light pulse generation using laser induced multiple-harmonic conversion processes in rare gases”. In: *Physics Letters A* 168(5) (1992), pp. 447–450.

[20] Lambert G. et al. “Injection of harmonics generated in gas in a free-electron laser providing intense and coherent extreme-ultraviolet light”. In: *Nature Physics* 4(4) (2008), pp. 296–300.

[21] Gauthier D.; Guizar-Sicairos M.; Ge X.; Boutu W.; Carre B.; Fienup J. R. and Merdji H. “Single-shot femtosecond x-ray holography using extended references”. In: *Physical Review Letters* 105(9) (2010), p. 93901.

[22] Keldysh L. V. “Ionization in the Field of a Strong Electromagnetic Wave”. In: *Sov. Phys. JETP* 20(5) (1965), pp. 1307–1314.

[23] Chang Z. *Fundamentals of Attosecond Optics*. CRS Press, Taylor and Francis Group, 2011.

[24] Lopez-Martens R. et al. “Amplitude and Phase Control of Attosecond Light Pulses”. In: *Phys. Rev. Lett.* 94(3) (2005), p. 033001.

[25] Gustafsson E.; Ruchon T.; Swoboda M.; Remetter T.; Pourtal E.; López-Martens R.; Balcou Ph. and A. LHuillier. “Broadband attosecond pulse shaping”. In: *Opt. Lett.* 32(1) (2007), pp. 1353–1355.

[26] Salières P. et al. “Feynman’s Path-Integral Approach for Intense-Laser-Atom Interactions”. In: *American Association for the Advancement of Science* 292(5518) (2001), pp. 902–905.

[27] Zenghu C. “Chirp of the single attosecond pulse generated by a polarization gating”. In: *Phys. Rev. A* 71(2) (2005), p. 023813.

[28] Takahashi E.; Nabekawa Y. and Midorikawa K. “Generation of 10-μJ coherent extreme-ultraviolet light by use of high-order harmonics”. In: *Opt. Lett.* 27(21) (2002), pp. 1920–1922.

[29] Kienberger R. et al. “Atomic transient recorder”. In: *Nature* 427 (2004), pp. 817–821.

[30] Burnett N. H.; Kan C. and Corkum P. B. "Ellipticity and polarization effects in harmonic generation in ionizing neon". In: *Phys. Rev. A* 51(5) (1995), pp. 3418–3421.

[31] Burnett N. H. Corkum P. B. and Ivanov M. Y. "Subfemtosecond pulses". In: *Opt. Lett.* 19(22) (1994), pp. 1870–1872.

[32] Tcherbakoff O.; Mével E.; Descamps D.; Plumridge J. and Constant E. "Time-gated high-order harmonic generation". In: *Phys. Rev. A* 68(4) (2003), p. 043804.

[33] Strelkov V.; Zaïr A.; Tcherbakoff O.; Lòpez-Martens R.; Cormier E.; Mèvel E. and Constant E. "Single attosecond pulse production with an ellipticity-modulated driving IR pulse". In: *Journal of Physics B: Atomic, Molecular and Optical Physics* 38(10) (2005), pp. 161–167.

[34] Samson J.A.R and Ederer D.L. *Vacuum Ultraviolet Spectroscopy, Vols. I and II*. Academic, New York, 1998.

[35] Peatman W.B. *Gratings,Mirrors and Slits: Beamline Desisgn for Soft X-Ray Synchrotron Radiation Sources*. Gordon and Breach, 1997.

[36] Atwood D. *Soft x-rays and extreme ultraviolet radiation: principles and applications*. Cambridge University Press, 1998.

[37] B.L. Henke; E.M. Gullikson and J.C. Davis. "X-ray interactions: photoabsorption, scattering, transmission, and reflection at E=50-30000 eV, Z=1-92". In: *Atomic Data and Nuclear Data Tables* 54 (1993), pp. 181–342.

[38] Mairesse Y. and Quéré F. "Frequency-resolved optical gating for complete reconstruction of attosecond bursts". In: *Phys. Rev. A* 71(1) (2005), p. 011401.

[39] Kyung Taec K.; Villeneuve D. M. and Corkum P. B. "Manipulating quantum paths for novel attosecond measurement methods". In: *Phys. Rev. A* 8 (2014), pp. 187–194.

[40] Lewenstein M.; Balcou P.; Ivanov M. Y.; LHuillier A. and Corkum P.B. "Theory of high-harmonic generation by low-frequency laser fields". In: *Phys. Rev. A* 49(3) (1994), p. 2117.

[41] Quéré F.; Mairesse Y. and Itatani J. "Temporal characterization of attosecond XUV fields". In: *Journal of Modern Optics* 52(2-3) (2005), pp. 339–360.

[42] Kane D. "Recent Progress Toward Real-Time Measurement of Ultrashort Laser Pulses". In: *IEEE JOURNAL OF QUANTUM ELECTRONICS* 35(4) (1999), pp. 421–431.

[43] Trebino R. *Soft x-rays and extreme ultraviolet radiation: principles and applications*. Kluwer Academic Publisher, 2000.

[44] F. Canova and L. Poletto. *Optical Technologies for Extreme-Ultraviolet and Soft X-ray Coherent Sources*. Springer, 2015.

[45] M. Hatayama; S. Ichimaru; T. Ohcni; E. J. Takahashi; K. Midorikawa and S. Oku. "Wide-range narrowband multilayer mirror for selecting a single-order harmonic in the photon energy range of 4070 eV". In: *Opt. Express* 24 (2016), pp. 14546–14551.

[46] L. Poletto and F. Frassetto. "Temporal Response of Ultrafast Grating Monochromators". In: *Appl. Sci.* 8 (2018), p. 5.

[47] L. Poletto and F. Frassetto. "Time-preserving grating monochromators for ultrafast extreme-ultraviolet pulses". In: *Appl. Opt.* 49 (2010), pp. 5465–5473.

[48] J. F. Seely; L. I. Goray; B. Kjornrattanawanich; J. M. Laming; G. E. Holland; K. A. Flanagan; R. K. Heilmann; C.-H. Chang; M. L. Schattenburg and A. P. Rasmussen. "Efficiency of a grazing-incidence off-plane grating in the soft-x-ray region". In: *Appl. Opt.* 45 (2006), pp. 1680–1687.

[49] M. Pascolini; S. Bonora; A. Giglia; N. Mahne; S. Nannarone and L. Poletto. "Gratings in a conical diffraction mounting for an extreme-ultraviolet time-delay-compensated monochromator". In: *Appl. Opt.* 45 (2006), pp. 3253–3262.

[50] D. Desiderio; S. Difonzo; B. Dlviacco; J. K. W. Jark; R. Krempaska; F. Lama; M. Luce; H. C. Mertins; M. Placentini; T. Prosperi et al. "The elettra circular polarization beamline and electromagnetic elliptical wiggler insertion device". In: *Synchrotron Radiation News* 12 (1999), pp. 34–38.

[51] M. Sacchi; C. Spezzani; P. Torelli; A. Avila; R. Delaunay and C.F. Hague. "Ultrahigh-vacuum soft x-ray reflectometer". In: *Rev. Sci. Inst.* 74 (2003), p. 2791.

[52] M. P. Kowalski; J. F. Seely; L. I. Goray; W. R. Hunter and J. C. Rife. "Comparison of the calculated and the measured efficiencies of a normal-incidence grating in the 125-225-Å wavelength range". In: *Appl. Opt.* 36 (1997), pp. 8939–8943.

[53] D. A. Content. "Diffraction grating groove analysis used to predict efficiency and scatter performance". In: *Gradient Index, Miniature, and Diffractive Optical Systems: Design and Analysis*. Ed. by Alan D. Kathman. Vol. 3778. Proc. SPIE. 1999, pp. 716–731.

[54] L. G. Parratt. "Surface Studies of Solids by Total Reflection of X-Rays". In: *American Physical Society* 5 (1954), pp. 359–369.

[55] Pascolini M.; Bonora S.; Giglia A.; Mahne N.; Nannarone S. and Poletto L. "Gratings in a conical diffraction mounting for an extreme-ultraviolet time-delay-compensated monochromator". In: *Appl. Opt.* 45 (2006), pp. 3253–3262.

[56] J. Limpert; N. Deguil-Robin; I. Manek-Hönninger; F. Salin; F. Röser; A. Liem; T. Schreiber; S. Nolte; H. Zellmer; A. Tünnermann; J. Broeng; A. Petersson and C. Jakobsen. "High-power rod-type photonic crystal fiber laser". In: *Opt. Express* 13 (2005), pp. 1055–1058.

[57] Limpert J.; Stutzki F.; Jansen F.; Otto H. J.; Eidam T.; Jauregui C. and A. Tünnermann. "Yb-doped large-pitch fibres: effective single-mode operation based on higher-order mode delocalisation". In: *Light: Science Amp; Applications* 1 (2012), pp. 1–5.

[58] Seise E.; Klenke A.; Limpert J. and Tünnermann A. "Coherent addition of fiber-amplified ultrashort laser pulses". In: *Opt. Express* 18 (2010), pp. 27827–27835.

[59] Nisoli M.; De Silvestri S.; Svelto O.; Szipöcs R.; Ferencz K.; Spielmann Ch.; Sartania S. and Krausz. F. "Compression of high-energy laser pulses below 5 fs". In: *Opt. Lett.* 22 (1997), pp. 522–524.

[60] Sola I. J.; Mével E.; Elouga L.; Constant E.; Strelkov V.; Poletto L.; Villoresi P.; Benedetti E.; Caumes J.-P.; Stagira S.; Vozzi C.; Sansone G. and Nisoli M. "Controlling attosecond electron dynamics by phase-stabilized polarization gating". In: *Nature Physics* 2 (2006), pp. 1745–2481.

[61] Peatross J.; Chaloupka J. L. and Meyerhofer D. D. "High-order harmonic generation with an annular laser beam". In: *Opt. Lett.* 19 (1994), pp. 942–944.

[62] *Stefan Kaesdorf GmbH*. http://kaesdorf.de/electrontof.html.

[63] Sansone G.; Benedetti E.; Calegari F.; Vozzi C.; Avaldi L.; Flammini R.; Poletto L.; Villoresi P.; Altucci C.; Velotta R.; Stagira S.; De Silvestri S. and Nisoli M. "Isolated Single-Cycle Attosecond Pulses". In: *Opt. Lett.* 314 (2006), pp. 443–446.

[64] Poletto L.; Frassetto F.; Calegari F.; Anumula S.; Trabattoni A. and Nisoli M. "Micro-focusing of attosecond pulses by grazing-incidence toroidal mirrors". In: *Opt. Express* 21 (2013), pp. 13040–13051.

[65] Kim K. T.; Zhang C.; Ruchon T.; Hergott J.-F.; Auguste T.; Villeneuve D. M.; Corkum P. B. and Quéré F. "Photonic streaking of attosecond pulse trains". In: *Opt. Lett.* 7 (2013), pp. 651–656.

[66] Frassetto F. and Poletto L. "Grating configurations to compress extreme-ultraviolet ultrashort pulses". In: *Appl. Opt.* 54 (2015), pp. 7985–7992.

[67] Lucchini M.; Lucarelli G. D.; Murari M.; Trabattoni A.; Fabris N.;Frassetto F.; De Silvestri S.; Poletto L. and Nisoli M. "Few-femtosecond extreme-ultraviolet pulses fully reconstructed by a ptychographic technique". In: *Opt. Express* 26(6) (2018), pp. 6771–6784.

[68] DeLong K. W.; Trebino R.; Hunter J. and White W. E. "Frequency-resolved optical gating with the use of second-harmonic generation". In: *J. Opt. Soc. Am. B* 11(11) (1994), pp. 2206–2215.

[69] Spangenberg D.; Rohwer E.; Brügmann M. H.; and Feurer T. "Ptychographic ultrafast pulse reconstruction". In: *Science* 40(6) (2015), pp. 1002–1005.

[70] Corder C.; Zhao P.; Bakalis J.; Li X.; Kershis M.D.; Muraca A.R.; White M.G. and Allison T.K. "Ultrafast extreme ultraviolet photoemission without space charge". In: *Struct. Dyn.* 5(5) (2018), p. 054301.

[71] Buss J.H. et al. "A setup for extreme-ultraviolet ultrafast angle-resolved photoelectron spectroscopy at 50-kHz repetition rate". In: *Rev. Sci. Instrum.* 90(2) (2019), p. 023105.

[72] Klas R. et al. "Table-top milliwatt-class extreme ultraviolet high harmonic light source". In: *Optica* 3(11) (2016), pp. 1167–1170.

[73] Harter J.W. et al. "A tunable low-energy photon source for high-resolution angle-resolved photoemission spectroscopy". In: *Rev. Sci. Instrum.* 83(11) (2012), p. 113103.

[74] Harter J.W. et al. "A tunable low-energy photon source for high-resolution angle-resolved photoemission spectroscopy". In: *Rev. Sci. Instrum.* 83(11) (2012), p. 113103.

[75] Frassetto F.; Fabris N.; Miotti P. and Poletto L. "Design Study of Time-Preserving Grating Monochromators for Ultrashort Pulses in the Extreme-Ultraviolet and Soft X-Rays". In: *Photonics* 4(14) (2017).

[76] Poletto L. and Frassetto F. "Cost-effective plane-grating monochromator design for extreme-ultraviolet application". In: *Appl. Opt.* 57(5) (2018), pp. 1202–1211.

[77] M.-C. et al. Chen. "Spatially coherent, phase matched, high-order harmonic EUV beams at 50 kHz". In: *Opt. Express* 17(20) (2009), pp. 17376–17383.

[78] del Rio M.S.; Canestrari N.; Jiang F. and Cerrina F. "SHADOW3: a new version of the synchrotron X-ray optics modelling package". In: *J. Synchrotron Radiat.* 18(5) (2011), pp. 708–716.